The QCD crossover up to $\mathcal{O}(\mu_B^6)$ from Lattice QCD

Dissertation

submitted by
Patrick Steinbrecher

Fakultät für Physik
Universität Bielefeld

March 2018

Supervisor and 1*st* corrector: Prof. Dr. Frithjof Karsch
2*nd* corrector: Prof. Dr. Helmut Satz

Contents

To my family
Rita & Friedrich and Oliver

Acknowledgments

First of all, I want to thank Frithjof Karsch and Swagato Mukherjee for their trust, wisdom and support in all parts of my life during the last three years. They enabled me to study and work on topics without any constrains. I greatly appreciate this freedom. I want to thank Christian Schmidt for sharing his knowledge about numerical and analytic aspects of this work. Furthermore, I thank Sayantan Sharma for his advise on the linear-μ formulation, for the great collaboration on keeping the many supercomputers busy, and for his fantastic Indian food. Edwin Laermann and Olaf Kaczmarek have been very important during my time as a Bachelor's and Master's student. They both inspired me to work in this field and helped with many good decisions I have made during that time. I am very grateful for all the great conversations and discussions with my collaborators from the HotQCD collaboration. This work would not have been possible without the exceptional scripts developed by Hauke Sandmeyer.

1 Introduction

In this work, we are going to study the crossover of quantum chromodynamics (QCD) as a function of the baryon chemical potential. We base this analysis on findings [1, 2] that at vanishing chemical potentials strong interaction matter does not have a genuine phase transition from a gas of hadrons and their resonances (HRG) to a quark-gluon plasma (QGP). In fact, it is an analytic crossover when increasing the temperature of a HRG system at zero chemical potential. Our goal is to understand up to which baryon chemical potential the crossover is still analytic. In other words, we are searching for signs of a second order QCD critical point as it would be the start of a genuine first order phase transition line. If no signs can be found, the change from a HRG to a QGP has to be an analytic crossover. In the following section, we introduce the current understanding of the QCD phase diagram. It primarily summarizes parts of [3, 4, 5]. For a more detailed introduction refer to the given references.

1.1 The QCD phase diagram

Quantum chromodynamics is the theory of strong interactions between fundamental constituents of matter, quarks and gluons. They become asymptotically free at high temperatures leading to a formation of a new phase referred to as quark-gluon plasma. Strong evidences, both from the theoretical as well as the experimental side, have been given that a QGP phase must exist [6, 7]. However, beyond that little is known about the actual phase structure of QCD at the physical point, i.e. the phases of a system with quark masses of nature. In Fig. 1.1, we show a possible QCD phase diagram as a function of the thermodynamic variables temperature T and baryon chemical potential μ_B. In particular interesting is the nature of the change from a HRG to a QGP. As mentioned above, it is known that at vanishing chemical potentials the hadronic phase has an analytic crossover to a QGP. Whether this analytic crossover endures for any μ_B or ends in a critical end-point (CEP) depends on the QCD structure far away from the physical point. This is why we first discuss the so-called Columbia plot which will guide us to understand possible structures of the QCD phase diagram at the physical point.

The Columbia plot is shown in Fig. 1.2. It describes the QCD structure as a function of the quark masses of a system with one strange quark and two light quarks at zero chemical potentials. At large quark masses, the system can be described by a $SU(3)$ pure gauge theory which has an exact $Z(3)$ symmetry. It has a first order phase transition with the Polyakov loop as the order parameter. In the chiral limit, i.e. $m_s = m_l \to 0$, the QCD Lagrangian has a global $\mathrm{SU}_L(N_f) \otimes \mathrm{SU}_R(N_f) \otimes \mathrm{U}_V(1) \otimes \mathrm{U}_A(1)$ symmetry. The axial $\mathrm{U}_A(1)$ symmetry is explicitly broken in order g^2 perturbation theory, known as the axial anomaly. The flavor symmetry $\mathrm{SU}_L(N_f) \otimes \mathrm{SU}_R(N_f)$ is spontaneously broken giving rise to $N_f^2 - 1$ Goldstone particles. For finite quark masses, the only exact symmetry is the $U_V(1)$ vector transformations group leading to quark number conservation. In the chiral limit, the transition is known to be of first order with the chiral condensate as the

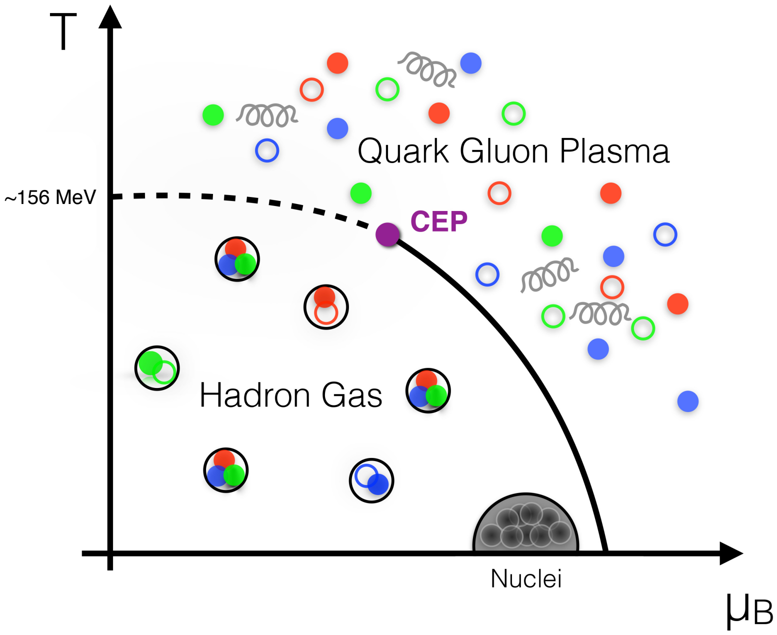

Figure 1.1: A sketch of the QCD phase diagram taken from [3]. Shown are three phases of QCD matter: the hadronic phase in which quarks and gluons are confined in hadrons, the quark-gluon plasma phase where quarks and gluons are asymptotically free, as well as ordinary nuclear matter. The dotted line represents the analytic crossover between these phases. In this sketch, a critical end-point (CEP) is assumed as the end of the crossover. The solid line would then correspond to a true first order phase transition.

order parameter. Both first order regions are expected to end on a second order critical line corresponding to a universality class of a three-dimensional Ising model with $Z(2)$ symmetry. At vanishing light quark mass and sufficiently large strange quark mass, the QCD Lagrangian has a global $O(4)$ symmetry. The associated second order transition line is believed to continuously connect to the $Z(2)$ second order line at a strange quark mass m_s^{tri}. However, the exact location of the tri-critical point m_s^{tri} is unknown. In particular interesting is its relative location to the physical strange quark mass m_s^{phys} as the $Z(2)$ critical line from the chiral limit region could be continuously connected to a critical point at the physical point for non-zero baryon chemical potential. This critical point would also have the universality class of a three-dimensional Ising model with $Z(2)$ symmetry. However, this highly depends on whether the size of the first order transition region close to the chiral limit shrinks or grows with increasing μ_B. For all other regions, the hadronic phase undergoes an analytic crossover to a QGP. The QCD phase structure is a matter of current research in heavy-ion collision experiments at the Relativistic Heavy Ion Collider (RHIC) at Brookhaven National Laboratory (BNL), and the Large Hadron Collider (LHC) at the European Organization for Nuclear Research

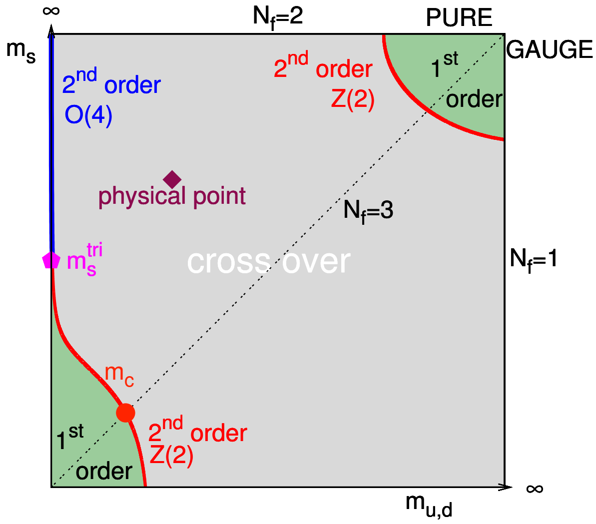

Figure 1.2: A sketch of the Columbia plot taken from [3]. Shown is the structure of QCD with a strange quark and two degenerate light quarks as a function of their masses at vanishing chemical potentials. Solid lines represent a second order phase transition while green regions correspond to a first order phase transition. The gray shaded area only has an analytic crossover from a HRG to a QGP.

(CERN). The so-called fireball created in heavy-ion collisions traverses through several states of matter each described by a specific set of temperature and density. After thermalization, the fireball is in the state of a quark-gluon plasma, then subsequently expands and cools down until hadrons form again. During this evolution, the medium crosses three lines in the $(T,\,\mu_B)$ plane whereby the properties of the system change. Depending on the reached baryon density, the system might cross a genuine phase transition line or has a rapid crossover from a quark-gluon plasma to a gas of heavy interacting hadrons. In this phase, hadrons scatter both elastically and inelastically, thus, the particle content is not fixed. Only after the so-called chemical freeze-out, inelastic interactions cease and the particle content is fixed. This state is characterized by a freeze-out temperature T_f and a freeze-out baryon chemical potential μ_B^f. Finally, the system is diluted sufficiently such that elastic collisions between hadrons cease, referred to as kinetic freeze-out. In heavy-ion collisions, detected hadrons only stem from chemical freeze-out. In particular interesting for current experiments are observables which reflect the thermal conditions of the system, i.e. are sensitive to the inner structure of the fireball. Fluctuations of globally conserved charges such as: baryon number B, electric charge Q and strangeness S vary strongly between the confined and deconfined phase, thus, can be measured to distinguish between the phases of QCD [8, 9]. However, fluctuations can only be observed in sub-volumes of a fireball. In experiments this can be studied on an event-by-event basis, i.e. fluctuations are obtained from measured ensembles of conserved charges in several heavy-ion collision events [10]. The idea of these fluctuation probes of the QCD phases is based on a simple picture: In the HRG all hadrons have electric charge of ±1 or ±2, while in the quark-gluon plasma the unit of charge is ±1/3 or ±2/3. Thus, the fluctuations of charged particles in or out of a sub-volume in the fireball produce a larger mean square fluctuation of the net electric charge while the system is in the hadronic phase [9]. The same applies for baryon-number fluctuations since baryons have baryon-number ±1 and quarks have only baryon-number ±1/3.

In order to search for a QCD critical point, it is mandatory to consider chiral observables as the crossover and a possible phase transition are supposed to be closely related to chiral symmetry restoration. If a critical point exists, we should be able to observe scaling of chiral observables with the critical exponents of a three-dimensional Ising model with $Z(2)$ symmetry at finite baryon chemical potential. The correlation length ξ, the chiral condensate Σ and the chiral susceptibility χ are supposed to scale as

$$\xi \sim t^{-\nu}, \qquad \Sigma - \Sigma_0 \sim t^{\beta}, \qquad \chi \sim t^{-\gamma}, \tag{1.1}$$

where t is the reduced temperature[1], $\nu \simeq 0.63$, $\beta \simeq 0.33$ and $\gamma \simeq 1.24$ [4]. At finite quark mass, the chiral condensate does not act as an order parameter, thus, approaches some non-zero value Σ_0. When approaching a critical point, a significant increase of chiral susceptibility fluctuations along the crossover must be observed. This scaling behavior will be the starting point of the present work. Similar arguments can be made for baryon-number fluctuations as these couple to the condensate [11, 12] which we are also going to investigate.

This work is organized in three parts. In the first part (see Sec. 1.2 and Sec. 2), we outline the basic constructs of lattice QCD in the so-called Highly-Improved Staggered Quark formulation and define chiral observables such as: subtracted condensate, subtracted susceptibility and disconnected susceptibility. Complementary, we derive their Taylor expansions in the chemical potentials μ_B, μ_Q and μ_S around vanishing chemical potentials.

The second part (see Sec. 3 and Sec. 4) extracts the curvature of the QCD crossover line, in terms of a Taylor expansion of $T_c(\mu_B)$, from the subtracted condensate and disconnected susceptibility for systems with different constraints, e.g. the initial conditions of heavy-ion collisions. Further, we compare it to the chemical freeze-out curve from heavy-ion collision experiments as well as lines of constant physics determined by lattice QCD simulations.

In the last part (see Sec. 5), we use the determined crossover curve to study chiral susceptibility fluctuations and baryon-number fluctuations along $T_c(\mu_B)$ as both are supposed to resemble singular behavior in the vicinity of a critical point. Additionally, we measure fluctuations of the chiral condensate along the crossover line.

---

[1] At finite chemical potential, the reduced temperature is dependent on the quark chemical potentials as well as their critical values.

1.2 Lattice QCD in the HISQ formulation[2]

In this work, we study the QCD phase diagram from first principles using a numerical technique referred to as lattice QCD (see [14, 15] for an in-depth summary). In particular in the low-energy regime, lattice QCD is the only theory which is able to really predict behavior of experiments as QCD is presently not solvable by analytic mathematical methods. Lattice QCD introduces a non-perturbative cut-off through replacing space-time with a discrete four-dimensional lattice defined by

$$\Lambda = \{\, (n_0,\, n_1,\, n_2,\, n_3) \,|\, n_i = 0,\, 1, \ldots, N_\sigma - 1 \,\wedge\, n_0 = 0,\, 1, \ldots, N_\tau - 1 \,\}\ , \tag{1.2}$$

where N_σ and N_τ are the number of sites in each spatial and the temporal dimension, respectively. The volume and temperature are given by

$$\frac{1}{T} = N_\tau a \qquad \text{and} \qquad V = (N_\sigma a)^3\ . \tag{1.3}$$

Here, a is the lattice spacing and represents a minimum wavelength, thus, in lattice QCD, no ultraviolet divergences arise from interactions between quarks and gluons. On the lattice, all observables are calculated in units of the lattice spacing a. To set the scale, the physical value of a can be extracted by comparison with a physical observable as obtained in experiments. Typically, this is done by comparison with the kaon decay constant f_K or the Sommer-scales

$$r_0^2 \left. \frac{dV_{q\bar{q}}(r)}{dr} \right|_{r=r_0} = 1.65 \quad \text{and} \quad r_1^2 \left. \frac{dV_{q\bar{q}}(r)}{dr} \right|_{r=r_1} = 1.0\,, \tag{1.4}$$

where $V_{q\bar{q}}$ is the heavy quark potential at zero temperature. The physical value for r_1 is often extracted from a fit to the 2S-1S energy splittings of the bottomonium meson [16]. Different methods for setting the scale have been described and compared in [17]. We mainly use f_K to set the scale in this work but also perform a comparison to continuum extrapolations using the r_1 scale (see Sec. 3 and Sec. 4). Our lattice formulation of choice is the so-called Highly-Improved Staggered Quark (HISQ) action [18] which we outline in the following paragraph.

Improved staggered quarks. The partition function is given by

$$Z = \int \mathcal{D}U \mathcal{D}\overline{\chi} \mathcal{D}\chi \ \ \exp\left(-S\right) \qquad \text{with} \qquad S = S_F + S_G \tag{1.5}$$

where U is a standard SU(3) link variable and S the HISQ action consisting of a gluonic part S_G and a fermionic part S_F. The staggered fermion fields have been introduced as χ and $\overline{\chi}$. They carry only one spin component and can be expressed in terms of

---

[2] Based on [13].

Grassmann numbers which enable to perform the fermion field integration. By doing so, the partition function Z further simplifies to

$$Z = \int \mathcal{D}U \ \det M_f \ \exp\left(-S_G\right) \ . \tag{1.6}$$

When using staggered fermions [19], the number of fermion doublers is reduced from 16 to only four degenerate species, referred to as tastes. At finite lattice spacing, these tastes are allowed to interact with each other, i.e. are unphysical as they can change their species through exchanging a gluon. However, in the continuum limit all tastes decouple and each taste contributes equally to the fermion determinant, i.e. $\det M_f$ describes four physical quarks with mass m_f. In order to perform simulations with only two light quarks u and d, and a strange quark s, we can modify the partition function by taking the fourth root of each fermion determinant. It is then given by

$$Z = \int \mathcal{D}U \ \det M_u^{1/4} \det M_d^{1/4} \det M_s^{1/4} \ \exp\left(-S_G\right) \ . \tag{1.7}$$

This approach, known as rooting, has caused a lot of controversy in the last decade [20]. Nonetheless, it has been shown successfully [21, 18] that rooting is a valid method for simulations with positive quark masses and zero quark chemical potentials. For vanishing taste mass, the staggered formulation has as in the continuum limit a $\mathrm{SU}_L(4)\otimes\mathrm{SU}_R(4)\otimes\mathrm{U}_V(1)$ symmetry. It is spontaneously broken to $\mathrm{SU}_V(4)\otimes\mathrm{U}_V(1)$ and gives rise to 15 massless Goldstone particles. However, the most important property of this formulation is that in the chiral limit, at finite lattice spacing, it is invariant under independent $\mathrm{U}(1)$ transformations of fermion fields at even and odd sites. A site is called even or odd if the sum of the coordinates, in units of the lattice spacing, is even or odd. It is a remnant of the chiral flavor symmetry and is only reduced to a subgroup by taste interactions. Thus, even at finite lattice spacing the staggered formulation enables to study the spontaneously broken chiral symmetry. It was shown in the so-called No-go theorem [22] that in a four-dimensional theory with a local action, it is not possible to create a lattice action which preserves the chiral symmetry and at the same time has no fermion doublers. This it why it is advantageous to allow for a certain number of fermion doublers in the action even when introducing additional taste-violations. Nonetheless, the HISQ formulation introduced a new fermionic action [23] which has no order a^2 errors in the kinetic properties as well as in the taste-violations. It is given by

$$S_F^{\mathrm{HISQ}} = S_F^{\mathrm{naive}}[X] + S_F^{\mathrm{Naik}}[W] + m\sum_n \overline{\chi}_n\chi_n \,, \tag{1.8}$$

where S_F^{naive} is the naive 1-link term

$$\begin{aligned} S_F^{\mathrm{naive}}[U] &= \sum_n \overline{\chi}_n \sum_\mu \eta_{n,\mu}\, c_1 \left(U_{n,\mu}\chi_{n+\hat{\mu}} - U^\dagger_{n-\hat{\mu},\mu}\chi_{n-\hat{\mu}}\right) \\ &= \sum_n \overline{\chi}_n \sum_\mu \eta_{n,\mu}\, c_1 \longleftarrow\!\underset{n}{\bullet}\!\longrightarrow \end{aligned} \tag{1.9}$$

Name	Path	Multiplicity	Coefficients	
			$\mathcal{F}^{f7}$	$\mathcal{F}^{f7L}$
1-link	$\hat{x}$	1	$1/8$	1
3-staple	$\hat{y}+\hat{x}-\hat{y}$	6	$1/16$	$1/16$
5-staple	$\hat{y}+\hat{z}+\hat{x}-\hat{z}-\hat{y}$	24	$1/64$	$1/64$
7-staple	$\hat{y}+\hat{z}+\hat{t}+\hat{x}-\hat{t}-\hat{z}-\hat{y}$	48	$1/384$	$1/384$
Lepage	$\hat{y}+\hat{y}+\hat{x}-\hat{y}-\hat{y}$	6	0	$-1/8$

Table 1.1: The smearing staples of the HISQ action for a link in $\hat{x}$ direction. There exist several other combinations for each staple (see Eq. (1.13)), e.g. the path $\hat{z}+\hat{x}-\hat{z}$ is also allowed for the 3-staple. Each staple has also contributions from paths starting in the backward direction. Taking this into account, the total number of possible paths (multiplicity) is shown for each staple. The coefficients for the first ($\mathcal{F}^{f7}$) and second ($\mathcal{F}^{f7L}$) level of smearing are shown and are motivated by perturbation theory [16] such that taste-violations are reduced.

and S_F^{Naik} the 3-link term

$$S_F^{\text{Naik}}[U] = \sum_n \overline{\chi}_n \sum_\mu \eta_{n,\mu}\, c_3 \left(N_{n,\mu}\chi_{n+3\hat{\mu}} - N^\dagger_{n-3\hat{\mu},\mu}\chi_{n-3\hat{\mu}} \right)$$

$$= \sum_n \overline{\chi}_n \sum_\mu \eta_{n,\mu}\, c_3$$

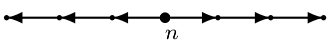

$$. \qquad (1.10)$$

This so-called Naik term uses a product of three links defined as $N_{n,\mu} \equiv U_{n,\mu}U_{n+\hat{\mu},\mu}U_{n+2\hat{\mu},\mu}$. As required, it preserves the staggered phases $\eta_{n,\mu}$ which are the remnants of the Dirac structure as removed by diagonalizing the lattice action in spin space. The staggered phases are given by

$$\eta_{n,1} = 1\,, \quad \eta_{n,2} = (-1)^{n_1}\,, \quad \eta_{n,3} = (-1)^{n_1+n_2}\,, \quad \eta_{n,0} = (-1)^{n_1+n_2+n_3}\,, \qquad (1.11)$$

where n_0, n_1, n_2 and n_3 are the coordinates of site n in units of the lattice spacing. The naive and Naik action stem from replacing the partial derivative in the Dirac operator with a higher-order difference quotient. At tree-level, they exactly cancel order a^2 discretization errors when defining their coefficients as

$$c_1 = \frac{9}{16} \quad \text{and} \quad c_3 = -\frac{1}{48}\,. \qquad (1.12)$$

The action (1.8) is not invariant under translation of multiples of the lattice spacing due to the alternating sign of $\eta_{n,\mu}$. Only under translations of multiples of $2a$, the staggered phase does not change its sign, therefore, a staggered action can be read as to describe fermions on a lattice where the sites are separated by $b \equiv 2a$. This can be understood as that the 16 degrees of freedom, of the four fermion doublers, are distributed over a

2^4 hypercube of the original lattice. On the lattice, the momenta p_μ are restricted to $(-\pi/a, \pi/a]$, thus, tastes within a hypercube have momentum components which differ by π/a. Additionally, this hypercube structure implies that the four tastes for each physical flavor interact with different link variables. This is why large taste symmetry-breaking effects are mainly produced by strongly fluctuating link variables, i.e. their origin is from virtual exchange of gluons with high momentum π/a or multiple gluons with total momentum π/a between tastes. This problem can be solved by smoothing each link with a perturbative motivated weighted sum of neighboring links, referred to as smearing. Following [23], a 3-link staple (see Eq. (1.13) and Tab. 1.1) removes coupling to gluons with a single transverse momentum of π/a. Likewise, a 5- and 7-link staple remove coupling to gluons with more components of momentum equal to π/a [16]. We refer to this as $\mathcal{F}^{f7}$ smearing which can be written as

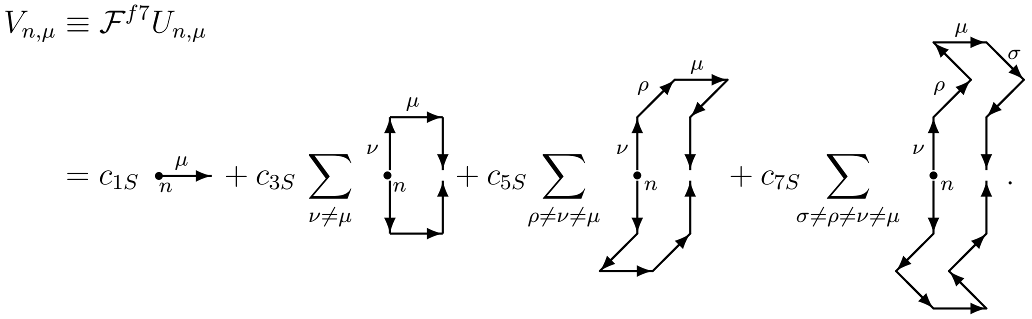

(1.13)

The coefficients for each staple are shown in Tab. 1.1. Smeared links are no longer elements of the gauge group SU(3) due to the sums in the $\mathcal{F}^{f7}$ scheme. To keep the good effects of smearing, it is needed to bound the smeared links by a projection to U(3) before the Naik links W are built. We define these reunitarized links as

$$W_{n,\mu} \equiv \mathcal{U}_{\mathrm{U}(3)} V_{n,\mu}\,, \tag{1.14}$$

where $\mathcal{U}_{\mathrm{U}(3)}$ is the projection operator. This smearing is a modification of the quark-gluon vertex in the action. It introduces a form factor that vanishes for taste-changing gluons with momenta π/a, but leaves gluons with low momenta unchanged [23]. Nonetheless, by exchanging multiple gluons with total momentum π/a, these taste-violations can still occur [16]. If each link on the lattice is smeared using Eq. (1.13), this introduces new lattice artifacts in the action of order a^2. An additional second level of smearing including a straight 5-link staple, called Lepage term (see Tab. 1.1), creates an action that is still order a^4 improved. Still, this smoothing increases the number of products of links in the smeared variables, thereby, the contribution of two-gluon vertices on quark lines are enhanced [18]. By smearing the 1-link term a second time using $\mathcal{F}^{f7L}$, it is guaranteed that gluons with high momenta are suppressed and order a^2 errors are removed. It is not required to project the 1-link terms back to U(3). The smeared links in the naive fermion action can then be expressed as

$$X_{n,\mu} \equiv \mathcal{F}^{f7L} W_{n,\mu} \tag{1.15}$$

with

$$\mathcal{F}^{f7L} U_{n,\mu} \equiv \mathcal{F}^{f7} U_{n,\mu} + c_L \sum_{\nu \neq \mu}$$

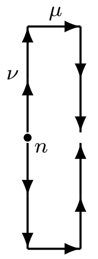

$. \quad (1.16)$

Note that in Eq. (1.8), the coefficient c_1 of the naive action has to take into account that the second level of smearing already includes a factor 9/8 of the 1-link term. In order to achieve the correct continuum limit at tree-level, the coefficients have to be

$$c_1 = \frac{1}{2} \quad \text{and} \quad c_3 = -\frac{1}{48}\,. \tag{1.17}$$

Additionally, the HISQ action has an Symanzik improved gauge action. It is given by

$$S_G = \beta \sum_n \sum_{\mu<\nu} c_P U_{n,\mu\nu} + c_R R_{n,\mu\nu} \qquad \text{with} \qquad \beta = 6/g^2\,, \tag{1.18}$$

where

$$R_{n,\mu\nu} = 1 - \frac{1}{6}\,\mathrm{Re}\,\mathrm{Tr}\,\Bigg($$

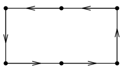

$+$

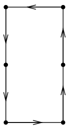

$\Bigg)_{n,\mu\nu} \quad (1.19)$

and $U_{n,\mu\nu}$ is the standard plaquette. At tree-level, the gauge action eliminates all order a^2 corrections if the coefficients are chosen to be

$$c_P = \frac{5}{4} \quad \text{and} \quad c_R = -\frac{1}{6}\,. \tag{1.20}$$

Compared to other staggered actions, such as stout [24] or the naive formulation, it was shown that the HISQ action greatly reduces the large pion mass splitting even at finite lattice spacing. Note that all these improvements of the action are only valid for simulations with the two light quarks u and d and the slightly heavier strange quark s. If applied with an additional charm quark, the coefficient for the Naik term has to be improved according to the bare charm mass [23].

Importance Sampling. The expectation value of an observable can be evaluated using Monte Carlo methods. For simulations with dynamical quarks, the expectation value of an observable O is obtained as

$$\langle O\rangle = \frac{1}{Z}\int \mathcal{D}U \;\; O \exp\left(-S_{\text{eff}}\right) \;. \tag{1.21}$$

with an effective action

$$S_{\text{eff}} = S_G - \sum_f \operatorname{Tr}\ln M_f \,. \tag{1.22}$$

The factor $\exp\left(-S_{\text{eff}}\right)$ is real for vanishing quark chemical potential and can be interpreted as a probability density. This is why the path integral can be solved numerically using importance sampling. This method samples link configurations $U^{(i)}$ with a probability

$$P\left(U^{(i)}\right) = \frac{1}{Z[U^{(i)}]}\exp\left(-S_{\text{eff}}[U^{(i)}]\right) \;. \tag{1.23}$$

The expectation value is then given by the sample average

$$\langle O\rangle = \lim_{N\longrightarrow\infty}\frac{1}{N}\sum_{i=1}^{N} O[U^{(i)}] \tag{1.24}$$

and can be approximated using a finite number of configurations. The error of this quantity can be estimated by a Jackknife or a statistical Bootstrap [14]. For the HISQ formulation, the only known exact algorithm for generating configurations with probability (1.23) is the Rational Hybrid Monte Carlo (RHMC) as described in [25].

Chemical potential. On the lattice, the chemical potential cannot be introduced as in the continuum. It has been shown that the naive way leads to quadratic divergences even for free fermions [26]. To achieve the correct continuum limit for finite density, we have to modify the link variables in temporal direction as

$$\begin{aligned} U_{n,0} &\quad\longrightarrow\quad \exp\left(\mu\right) U_{n,0} \\ U^{\dagger}_{n,0} &\quad\longrightarrow\quad \exp\left(-\mu\right) U^{\dagger}_{n,0} \,. \end{aligned} \tag{1.25}$$

However, it is also possible to introduce the chemical potential as

$$\begin{aligned} U_{n,0} &\quad\longrightarrow\quad \mu\, U_{n,0} \\ U^{\dagger}_{n,0} &\quad\longrightarrow\quad -\mu\, U^{\dagger}_{n,0} \,. \end{aligned} \tag{1.26}$$

In this so-called linear-μ formulation, it has been shown [27, 28] that in e.g. a μ expansion of the pressure all orders higher than $\mathcal{O}(\mu^4)$ are free of divergences (see Sec. 2.3). If applied to Monte Carlo simulations, this transformation leads to the so-called sign problem. For finite chemical potential, the fermion determinant becomes complex if μ is real. This is why the integrand in Eq. (1.23) cannot be interpreted anymore as a probability density, therefore, importance sampling is ill-defined. However, for small chemical potentials different approaches exist to simulate QCD at finite net quark density such as: Taylor expansion around $\mu = 0$ (see Sec. 2.1), imaginary μ [29] and reweighting [30].

1.3 Simulation setup

We have generated gauge field ensembles using a RHMC for 4 lattice volumes with $N_\tau = 6, 8, 12$ and 16 in a temperature range from 135 MeV to 175 MeV. The simulations have been performed using the tree-level improved HISQ formulation with two degenerate light quarks and a heavier strange quark with a physical ratio of $m_s/m_l = 27$. The quark masses have been set to their physical values. The parameters are shown in Tab. 1.2 and have been tuned such that the continuum limit is taken on a line of constant physics [31].

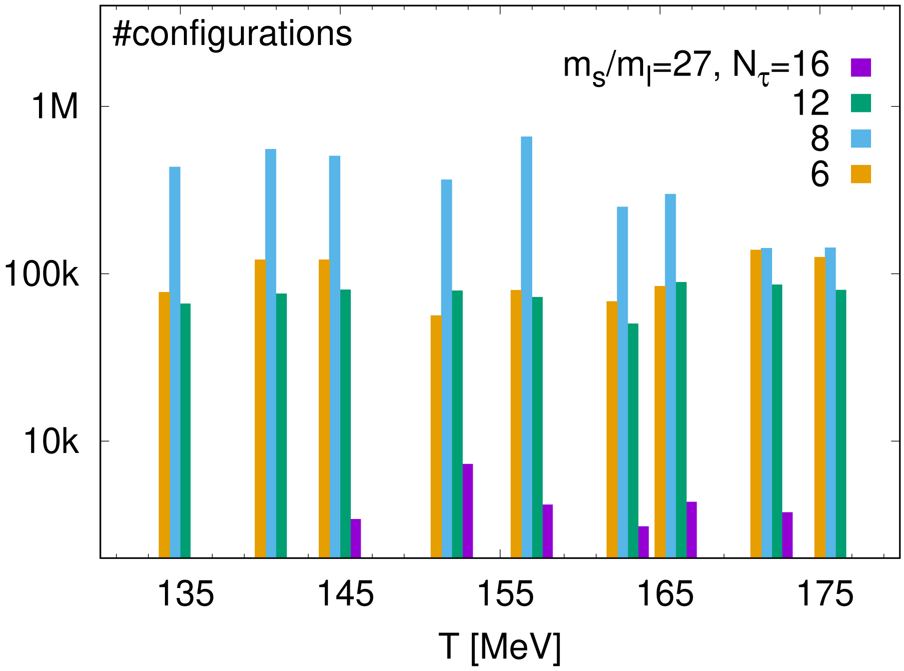

Figure 1.3: The number of configurations per temperature for ensembles with $N_\tau = 6, 8, 12$ and 16 as used in this work. The lattices have an aspect ratio of 4, i.e. $N_\sigma = 4N_\tau$. Each configuration is separated by 10 trajectories of unit length and have been generated using a RHMC algorithm with physical quark masses. The parameters are shown in Tab. 1.2.

In the continuum limit, these parameters correspond to a physical pion mass of about 140 MeV. For determining the lattice spacing $a(\beta)$, we use the kaon decay constant as a scale [32] with a value of $f_K = 155.7(9)/\sqrt(2)$ MeV. This allows us to determine the temperature T as shown in Tab. 1.2.

$N_\tau = 6$				$N_\tau = 8$			
β	m_l	T [MeV]	#conf.	β	m_l	T [MeV]	#conf.
5.980	0.00435	135.29	77392	6.245	0.00307	134.64	433848
6.010	0.00416	139.71	120797	6.285	0.00293	140.45	552049
6.045	0.00397	145.05	120777	6.315	0.00281	144.95	504390
6.080	0.00387	150.59	56160	6.354	0.00270	151.00	362474
6.120	0.00359	157.17	79545	6.390	0.00257	156.78	656149
6.150	0.00345	162.28	68159	6.423	0.00248	162.25	250234
6.170	0.00336	165.98	83980	6.445	0.00241	165.98	298445
6.200	0.00324	171.15	138476	6.474	0.00234	171.02	141528
6.225	0.00314	175.76	125281	6.500	0.00228	175.64	142705
$N_\tau = 12$				$N_\tau = 16$			
β	m_l	T [MeV]	#conf.	β	m_l	T [MeV]	#conf.
6.640	0.00196	134.94	66012	7.010	0.00132	144.9	3403
6.680	0.00187	140.44	75648	7.054	0.00129	151.0	7280
6.712	0.00181	144.97	79848	7.095	0.00124	156.9	4156
6.754	0.00173	151.10	78925	7.130	0.00119	162.0	3085
6.794	0.00167	157.13	72321	7.156	0.00116	166.0	4322
6.825	0.00161	161.94	50012	7.188	0.00113	170.9	3742
6.850	0.00157	165.91	88726				
6.880	0.00153	170.77	85661				
6.910	0.00148	175.76	79769				

Table 1.2: The parameters for generating gauge ensembles using the HISQ action with two degenerate light quarks and a heavier strange quark for lattices with $N_\tau = 6, 8, 12$ and 16. The temperature T has been determined using the f_K scale.

2 Chiral observables

The QCD crossover as well as a possible phase transition from a HRG to a QGP is supposed to be closely related to chiral symmetry restoration. This is why we consider three chiral observables to study the QCD crossover and in particular the pseudo-critical temperature T_0 at vanishing chemical potential. These can be derived from mass derivatives of the partition function $\ln Z$. In the following, we start from a staggered partition function with three non-degenerate quarks

$$Z = \int \mathcal{D}U \det M_u^{1/4} \det M_d^{1/4} \det M_s^{1/4} \, \mathrm{e}^{-S_G} \tag{2.1}$$

as it will be important at a later point[3]. For a quark flavor f, the chiral condensate is given by

$$\Sigma_f = \frac{T}{V}\frac{\partial}{\partial m_f} \ln Z = \frac{T}{V}\frac{1}{4}\left\langle \mathrm{Tr}\, M_f^{-1} \right\rangle \tag{2.2}$$

where M is the fermion matrix and V the spatial volume. It is more natural to study the light condensate in a two-flavor formulation where contributions from u and d quarks are taken into account. It is given by

$$\Sigma_l = \frac{T}{V}\left(\frac{\partial}{\partial m_u} + \frac{\partial}{\partial m_d}\right) \ln Z = \Sigma_u + \Sigma_d \; . \tag{2.3}$$

To remove additive non-logarithmic UV divergences in Σ_l, we subtract the strange chiral condensate. Additionally, we multiply Σ_l and Σ_s respectively with the bare quark masses m_s and $m_u + m_d$ to cancel multiplicative renormalization factors. The subtracted condensate is given by

$$\Sigma_{\mathrm{sub}} = m_s \Sigma_l - (m_u + m_d)\Sigma_s \; . \tag{2.4}$$

The point of largest fluctuations, i.e. T_0, is given by the inflection point of the condensate defined by the condition

$$\frac{d^2}{dT^2}\Sigma_{\mathrm{sub}} \equiv 0 \; . \tag{2.5}$$

However, with limited data points it is usually hard to obtain T_0 from a fit of the condensate. A more pronounced observable to determine the crossover temperature is

---

[3] For vanishing chemical potential and degenerate light quark masses, it is not necessary to make a distinction between u and d quarks. However, in a constrained Taylor expansion the u and d quark expansion coefficients have different contributions, thus, have to be treated independently even for degenerate light quarks.

the chiral susceptibility which is supposed to diverge at T_0 in the chiral limit. The total chiral susceptibility is given by

$$\chi_f = \frac{\partial}{\partial m_f}\Sigma_f = \chi_{f,\mathrm{conn}} + \chi_{f,\mathrm{disc}} \tag{2.6}$$

with

$$\chi_{\mathrm{f,conn}} = -\frac{T}{V}\frac{1}{4}\left\langle \mathrm{Tr}\, M_f^{-2}\right\rangle \ , \qquad \chi_{\mathrm{f,disc}} = \frac{T}{V}\frac{1}{16}\left[\left\langle \left(\mathrm{Tr}\, M_f^{-1}\right)^2\right\rangle - \left\langle \mathrm{Tr}\, M_f^{-1}\right\rangle^2\right] \ . \tag{2.7}$$

Similarly as for the condensate, the total susceptibility in two-flavor formulation is given by

$$\chi_l = \frac{T}{V}\left(\frac{\partial}{\partial m_u} + \frac{\partial}{\partial m_d}\right)\Sigma_l = \chi_u + \chi_d + 2\chi_{ud} \tag{2.8}$$

with

$$\chi_{fg} = \frac{\partial}{\partial m_f}\Sigma_g = \frac{T}{V}\frac{1}{16}\left(\left\langle \mathrm{Tr}\, M_f^{-1}\,\mathrm{Tr}\, M_g^{-1}\right\rangle - \left\langle \mathrm{Tr}\, M_f^{-1}\right\rangle\left\langle \mathrm{Tr}\, M_g^{-1}\right\rangle\right) \ . \tag{2.9}$$

For degenerate quark masses, i.e. $m_f \equiv m_g$, the mixed term χ_{fg} is equal to the disconnected susceptibility. This formulation still suffers from UV divergences and renormalization factors. This is why we define the subtracted susceptibility as

$$\begin{aligned}\chi_{\mathrm{sub}} &= \frac{T}{V}m_s\left(\frac{\partial}{\partial m_u} + \frac{\partial}{\partial m_d}\right)\Sigma_{\mathrm{sub}} \\ &= m_s^2\chi_l - 2m_s\Sigma_s - m_s(m_u+m_d)(\chi_{su}+\chi_{sd}) \ .\end{aligned} \tag{2.10}$$

We also introduce the two-flavor disconnected susceptibility

$$\chi_{\mathrm{disc}} = m_s^2\left(\chi_{u,\mathrm{disc}} + \chi_{d,\mathrm{disc}} + 2\chi_{ud}\right) \ . \tag{2.11}$$

For finite light quark masses, the subtracted and disconnected susceptibility still have a pronounced maximum at T_0, thus, the pseudo-critical temperature can be easily obtained by solving

$$\frac{d}{dT}\chi_{\mathrm{sub}} \equiv 0 \qquad \text{and} \qquad \frac{d}{dT}\chi_{\mathrm{disc}} \equiv 0 \ . \tag{2.12}$$

In contrast to the total susceptibility, the disconnected susceptibility has no additive UV divergences and only requires multiplicative renormalization. It should reproduce the dominant singular behavior in the chiral limit. This is why we also use χ_{disc} to determine T_0.

2.1 Taylor series in chemical potentials

We want to study the chiral properties of a system as a function of the chemical potentials μ_X for conserved charges X: baryon number B, electric charge Q and strangeness S. In this BQS ensemble, the quark chemical potentials can be derived from

$$\begin{aligned} \mu_B &= \mu_u + 2\mu_d \\ \mu_Q &= \mu_u - \mu_d \\ \mu_S &= \mu_d - \mu_s \,. \end{aligned} \tag{2.13}$$

In this work, we focus on the observables χ_{disc} and Σ_{sub} and Taylor expand these in the dimensionless parameter $\hat{\mu}_X \equiv \mu_X/T$ at vanishing chemical potential. These expansions are closely related to the expansion coefficients of the QCD pressure as the only difference is further mass derivatives. They have been first described for simplified cases in [33, 34]. This is why it is natural to first introduce relations needed for the Taylor series of the pressure which can be written as

$$\frac{P}{T^4} = \frac{1}{VT^3}\ln Z = \sum_{i,j,k=0}^{\infty} \frac{\chi_{ijk}^{BQS}}{i!j!k!}\hat{\mu}_B^i \hat{\mu}_Q^j \hat{\mu}_S^k \tag{2.14}$$

with

$$\chi_{ijk}^{BQS} = \frac{1}{VT^3} \left. \frac{\partial \ln Z}{\partial \hat{\mu}_B^i \partial \hat{\mu}_Q^j \partial \hat{\mu}_S^k} \right|_{\mu=0} \qquad \text{and} \qquad \chi_{000}^{BQS} = \frac{P(T,\mu=0)}{T^4} \,. \tag{2.15}$$

The derivatives $\partial/\partial\mu_X$ needed for the generalized susceptibilities are given in terms of quark chemical potential derivatives

$$\frac{\partial}{\partial \mu_B} = \frac{1}{3}\left(\frac{\partial}{\partial \mu_u} + \frac{\partial}{\partial \mu_d} + \frac{\partial}{\partial \mu_s} \right) \tag{2.16}$$

$$\frac{\partial}{\partial \mu_Q} = \frac{1}{3}\left(2\frac{\partial}{\partial \mu_u} - \frac{\partial}{\partial \mu_d} - \frac{\partial}{\partial \mu_s} \right) \tag{2.17}$$

$$\frac{\partial}{\partial \mu_S} = -\frac{\partial}{\partial \mu_s} \,. \tag{2.18}$$

It will be useful to define the partition function as

$$Z = \int \mathcal{D}U \, \mathrm{e}^{D_0^u} \, \mathrm{e}^{D_0^d} \, \mathrm{e}^{D_0^s} \, \mathrm{e}^{-S_G} \qquad \text{with} \qquad D_i^f = \frac{1}{4}\partial_f^i \ln \det M_f \,. \tag{2.19}$$

Here, ∂_f^i denotes the i-th derivative w.r.t. quark chemical potential μ_f. In the following, we use fgh for quark flavors and ijk for the order of derivatives. The derivative of an expectation value of an observable is given by

$$\partial_f \langle \mathcal{O} \rangle = \langle \partial_f \mathcal{O} \rangle + \left\langle \mathcal{O} D_1^f \right\rangle - \langle \mathcal{O} \rangle \left\langle D_1^f \right\rangle \,. \tag{2.20}$$

Higher order derivatives of Z can be derived by using

$$A_i^f = \frac{1}{Z}\partial_f^i Z = \langle a_i^f \rangle \tag{2.21}$$

with

$$a_i^f = \mathrm{e}^{-D_0^f}\, \partial_f^i\, \mathrm{e}^{D_0^f} \tag{2.22}$$

as a kernel. Here, the first orders are given by

$$a_0^f = 1 \tag{2.23}$$
$$a_1^f = D_1^f \tag{2.24}$$
$$a_2^f = D_2^f + {D_1^f}^2 \tag{2.25}$$
$$a_3^f = D_3^f + 3D_2^f D_1^f + {D_1^f}^3 \ . \tag{2.26}$$

We can define a more general formulation for derivatives w.r.t. three different quark flavors in terms of Eq. (2.22). It is given by

$$A_{ijk}^{fgh} = \frac{1}{Z}\partial_f^i \partial_g^j \partial_h^k Z = \left\langle a_i^f a_j^g a_k^h \right\rangle \ . \tag{2.27}$$

By using Eq. (2.20), derivatives of A can be derived iteratively as

$$\partial_h A_{ijk}^{fgh} = A_{i,j,k+1}^{fgh} - A_{ijk}^{fgh} A_1^h \ . \tag{2.28}$$

At this point, we can derive derivatives of $\ln Z$ iteratively by solving

$$\partial_f^i \partial_g^j \partial_h^{k+1} \ln Z = \partial_f^i \partial_g^j \partial_h^k A_{i,j,1}^{fgh} \ . \tag{2.29}$$

Chiral Condensate. For a single quark flavor f, the expansion of the chiral condensate is given by

$$\frac{\Sigma_f}{f_K^3} = \sum_{i,j,k=0}^{\infty} \frac{\Gamma_{ijk}^{BQS}}{i!j!k!} \hat{\mu}_B^i \hat{\mu}_Q^j \hat{\mu}_S^k \qquad \text{with} \qquad \Gamma_{ijk}^{BQS} = \left. \frac{\partial \Sigma_f / f_K^3}{\partial \hat{\mu}_B^i \partial \hat{\mu}_Q^j \partial \hat{\mu}_S^k} \right|_{\mu=0} \tag{2.30}$$

where f_K is the kaon decay constant. In the following, we introduce relations needed to compute the expansion coefficient Γ_{ijk}^{BQS}. For expanding the chiral condensate, we have to compute higher order derivatives of $\mathrm{Tr}\, M^{-1}$ which can be expressed using a similar iterative scheme. As a generator we use

$$F_i^f = \left\langle w_i^f \right\rangle \qquad \text{with} \qquad w_i^f = \mathrm{e}^{-D_0^f}\, \partial_f^i \left(C_0^f\, \mathrm{e}^{D_0^f} \right) \tag{2.31}$$

and

$$C_i^f = \frac{1}{4}\partial_f^i \operatorname{Tr} M_f^{-1} \ . \tag{2.32}$$

The first orders of Eq. (2.31) are given by

$$w_0^f = C_0^f \tag{2.33}$$
$$w_1^f = C_1^f + C_0^f D_1^f \tag{2.34}$$
$$w_2^f = C_2^f + 2C_1^f D_1^f + C_0^f D_2^f + C_0^f {D_1^f}^2 \tag{2.35}$$
$$w_3^f = C_3^f + 3C_2^f C_1^f + 3C_1^f D_2^f + C_0^f C_3^f + 3C_1^f {D_1^f}^2 + 3C_0^f D_2^f D_1^f + C_0^f {D_1^f}^3 \ . \tag{2.36}$$

We are now able to define derivatives w.r.t. several flavors

$$(F_0^f)_{ijk}^{fgh} = \left\langle w_i^f a_j^g a_k^h \right\rangle \tag{2.37}$$
$$(F_0^g)_{ijk}^{fgh} = \left\langle a_i^f w_j^g a_k^h \right\rangle \tag{2.38}$$
$$(F_0^h)_{ijk}^{fgh} = \left\langle a_i^f a_j^g w_k^h \right\rangle \ . \tag{2.39}$$

Here, (F_0^f) denotes the quark dependency of the chiral condensate. However, in the following we drop this notation and use F instead of (F_0^f) since the general structure of higher order derivatives of $\operatorname{Tr} M_f^{-1}$, in terms of F_{ijk}^{fgh}, is always the same for any f. By using Eq. (2.20), derivatives of F can be derived iteratively as

$$\partial_h F_{ijk}^{fgh} = F_{i,j,k+1}^{fgh} - F_{ijk}^{fgh} A_1^h \qquad \text{with} \qquad F = (F_0^{f/g/h}) \ . \tag{2.40}$$

We can now express the expansion coefficient Γ_{ijk}^{BQS} in Eq. (2.30) in the quark basis F_{ijk}^{fgh} by using Eq. (2.18) and solving

$$\Gamma_{ijk}^{BQS} = \frac{1}{f_K^3} \frac{N_\tau^{-1-(i+j+k)}}{N_\sigma^3} \frac{\partial F}{\partial \mu_B^i \partial \mu_Q^j \partial \mu_S^k} = \frac{1}{f_K^3} \frac{N_\tau^{-1-(i+j+k)}}{N_\sigma^3} F_{ijk}^{BQS} \tag{2.41}$$

with

$$\Gamma = (\Gamma^{u/d/s}) \ . \tag{2.42}$$

E.g., the explicit form of F_{200}^{BQS} is given by

$$\begin{aligned} F_{200}^{BQS} = \frac{1}{9}\Big(& - A_{002}^{uds} F - 2A_{011}^{uds} F - A_{020}^{uds} F - 2A_{101}^{uds} F - 2A_{110}^{uds} F \\ & - A_{200}^{uds} F + F_{002}^{uds} + 2F_{011}^{uds} + F_{020}^{uds} + 2F_{101}^{uds} + 2F_{110}^{uds} + F_{200}^{uds} \Big) \ . \end{aligned} \tag{2.43}$$

The Taylor expansion of the subtracted condensate can be written as

$$\frac{\Sigma_{\text{sub}}}{f_K^4} = \sum_{i,j,k=0}^{\infty} \frac{\Omega_{ijk}^{BQS}}{i!j!k!} \hat{\mu}_B^i \hat{\mu}_Q^j \hat{\mu}_S^k \tag{2.44}$$

with

$$\Omega_{ijk}^{BQS} = \frac{1}{f_K} \left[m_s \left((\Gamma^u)_{ijk}^{BQS} + (\Gamma^d)_{ijk}^{BQS} \right) - (m_u + m_d)(\Gamma^s)_{ijk}^{BQS} \right] . \tag{2.45}$$

Note that even for degenerate light quark masses

$$(\Gamma^u)_{ijk}^{BQS} \neq (\Gamma^d)_{ijk}^{BQS} \qquad \text{for} \qquad j > 0 \tag{2.46}$$

as can be seen from Eq. (2.17). This is why it is necessary to make a distinction between u and d quark coefficients in expansions which include μ_Q derivatives.

Chiral Susceptibility. For expanding the disconnected chiral susceptibility, we have to compute higher order derivatives of $(\operatorname{Tr} M^{-1})^2$ which can be expressed using a similar iterative scheme. As a generator we use

$$G_i^f = \left\langle g_i^f \right\rangle \qquad \text{with} \qquad g_i^f = \mathrm{e}^{-D_0^f} \, \partial_f^i \left({C_0^f}^2 \, \mathrm{e}^{D_0^f} \right) . \tag{2.47}$$

The first orders are given by

$$g_0^f = {C_0^f}^2 \tag{2.48}$$

$$g_1^f = 2 C_0^f C_1^f + {C_0^f}^2 D_1^f \tag{2.49}$$

$$g_2^f = 2 C_0^f C_2^f + 4 C_0^f C_1^f D_1^f + 2 {C_1^f}^2 + {C_0^f}^2 D_2^f + {C_0^f}^2 {D_1^f}^2 . \tag{2.50}$$

We are now able to define derivatives w.r.t. several flavors

$$(G_0^f)_{ijk}^{fgh} = \left\langle g_i^f a_j^g a_k^h \right\rangle \tag{2.51}$$

$$(G_0^g)_{ijk}^{fgh} = \left\langle a_i^f g_j^g a_k^h \right\rangle \tag{2.52}$$

$$(G_0^h)_{ijk}^{fgh} = \left\langle a_i^f a_j^g g_k^h \right\rangle . \tag{2.53}$$

By using Eq. (2.20), derivatives of G can be derived iteratively as

$$\partial_h G_{ijk}^{fgh} = G_{i,j,k+1}^{fgh} - G_{ijk}^{fgh} A_1^h \qquad \text{with} \qquad G = (G_0^{f/g/h}) . \tag{2.54}$$

The expansion of the disconnected susceptibility for a quark flavor f is given by

$$\frac{\chi_{f,\text{disc}}}{f_K^2} = \sum_{i,j,k=0}^{\infty} \frac{\Upsilon_{ijk}^{BQS}}{i!j!k!} \hat{\mu}_B^i \hat{\mu}_Q^j \hat{\mu}_S^k \tag{2.55}$$

with

$$\Upsilon_{ijk}^{BQS} = \frac{1}{f_K^2} \frac{N_\tau^{-1-(i+j+k)}}{N_\sigma^3} \left. \frac{\partial \left(G - F^2\right)}{\partial \mu_B^i \partial \mu_Q^j \partial \mu_S^k} \right|_{\mu=0} . \tag{2.56}$$

For the two-flavor susceptibility, we have to compute derivatives of χ_{ud}. In particular for the first term in Eq. (2.9), we introduce

$$K_{ijk}^{uds} = \left\langle w_i^u w_j^d a_k^s \right\rangle . \tag{2.57}$$

Note that the definition of K is specific for χ_{ud}. Similarly, derivatives of K can be derived iteratively as

$$\partial_h K_{ijk}^{fgh} = K_{i,j,k+1}^{fgh} - K_{ijk}^{fgh} A_1^h . \tag{2.58}$$

The expansion of the two-flavor disconnected susceptibility can be expressed as

$$\frac{\chi_\text{disc}}{f_K^4} = \sum_{i,j,k=0}^{\infty} \frac{\Xi_{ijk}^{BQS}}{i!j!k!} \hat{\mu}_B^i \hat{\mu}_Q^j \hat{\mu}_S^k \tag{2.59}$$

with

$$\Xi_{ijk}^{BQS} = \frac{m_s^2}{f_K^2} \left((\Upsilon^u)_{ijk}^{BQS} + (\Upsilon^d)_{ijk}^{BQS} + 2H_{ijk}^{BQS} \right) \tag{2.60}$$

and

$$H_{ijk}^{BQS} = \frac{1}{f_K^2} \frac{N_\tau^{-1-(i+j+k)}}{N_\sigma^3} \left. \frac{\partial \left(K - F_0^u F_0^d\right)}{\partial \mu_B^i \partial \mu_Q^j \partial \mu_S^k} \right|_{\mu=0} . \tag{2.61}$$

2.2 Constrained series expansions

The initial conditions in heavy-ion collisions of e.g. Au-Au and Pb-Pb are given by

$$n_S = 0, \quad \frac{n_Q}{n_B} = 0.4 , \tag{2.62}$$

where n_X are the densities for baryon number B, strangeness S and electric charge Q. By imposing these constrains, we can can fix the chemical potentials μ_Q and μ_S. Their expansions in $\hat{\mu}_B$ can be expressed as

$$\hat{\mu}_Q = q_1 \hat{\mu}_B + q_3 \hat{\mu}_B^3 + q_5 \hat{\mu}_B^5 + \mathcal{O}\left(\hat{\mu}_B^7\right) \tag{2.63}$$

$$\hat{\mu}_S = s_1 \hat{\mu}_B + s_3 \hat{\mu}_B^3 + s_5 \hat{\mu}_B^5 + \mathcal{O}\left(\hat{\mu}_B^7\right) , \tag{2.64}$$

where q_n and s_n are ratios of sums of generalized susceptibilities and can be derived by requiring these constrains order by order. The coefficients can be found in [35]. By using the above equations, we can reorder the Taylor expansions in Eq. (2.44) and Eq. (2.55) in powers of $\hat{\mu}_B$. We introduce the following notation for the constrained expansion of the subtracted condensate

$$\frac{\Sigma_{\text{sub}}}{f_K^4} = \sum_{n=0}^{\infty} \frac{c_n^{\Sigma}}{n!} \hat{\mu}_B^n \tag{2.65}$$

and the disconnected susceptibility

$$\frac{\chi_{\text{disc}}}{f_K^4} = \sum_{n=0}^{\infty} \frac{c_n^{\chi}}{n!} \hat{\mu}_B^n \ . \tag{2.66}$$

Here, the first non-vanishing coefficients are defined as

$$c_2^{\Sigma} = \Omega_{200}^{BQS} + \Omega_{020}^{BQS} q_1^2 + 2\Omega_{101}^{BQS} s_1 + \Omega_{002}^{BQS} s_1^2 + 2q_1(\Omega_{110}^{BQS} + \Omega_{011}^{BQS} s_1) \tag{2.67}$$

and

$$c_2^{\chi} = \Xi_{200}^{BQS} + \Xi_{020}^{BQS} q_1^2 + 2\Xi_{101}^{BQS} s_1 + \Xi_{002}^{BQS} s_1^2 + 2q_1(\Xi_{110}^{BQS} + \Xi_{011}^{BQS} s_1) \ . \tag{2.68}$$

In general, the structure of the constrained Taylor expansion coefficients are always the same. Therefore, the 4th order of the subtracted condensate and the disconnected susceptibility are both given by

$$\begin{aligned} c_4 =& X_{400}^{BQS} + X_{040}^{BQS} q_1^4 + 4X_{301}^{BQS} s_1 + 6X_{202}^{BQS} s_1^2 + 4X_{103}^{BQS} s_1^3 + X_{004}^{BQS} s_1^4 \\ &+ 24q_3(X_{110}^{BQS} + X_{011}^{BQS} s_1) + 4q_1^3(X_{130}^{BQS} + X_{031}^{BQS} s_1) \\ &+ 6q_1^2(X_{220}^{BQS} + 2X_{121}^{BQS} s_1 + X_{022}^{BQS} s_1^2) + 24X_{101}^{BQS} s_3 + 24X_{002}^{BQS} s_1 s_3 \\ &+ 4q_1(X_{310}^{BQS} + 6X_{020}^{BQS} q_3 + 3X_{211}^{BQS} s_1 + 3X_{112}^{BQS} s_1^2 + X_{013}^{BQS} s_1^3 + 6X_{011}^{BQS} s_3) \end{aligned} \tag{2.69}$$

with $X = \Omega$ for c_4^{Σ} and $X = \Xi$ for c_4^{χ}. The 6th order becomes lengthy but is straightforward to derive. By setting the coefficients s_n and q_n to zero, the expansion coefficients c_n represent a system with vanishing μ_Q and μ_S which we discuss in Sec. 4.1.

2.3 Computation of traces

The equations for D_i^f and C_i^f can be solved using the identities

$$\frac{\partial \ln \det M_f}{\partial \mu_f} = \mathrm{Tr}\, \frac{\partial \ln M_f}{\partial \mu_f} = \mathrm{Tr} \left(M_f^{-1} \frac{\partial M_f}{\partial \mu_f} \right) \tag{2.70}$$

and

$$\frac{\partial M_f^{-1}}{\partial \mu_f} = -M_f^{-1}\frac{\partial M_f}{\partial \mu_f}M_f^{-1}\,. \tag{2.71}$$

The first orders are given by

$$D_1^f = \frac{1}{4}\,\mathrm{Tr}\left(M_f^{-1}\frac{\partial M_f}{\partial \mu_f}\right) \tag{2.72}$$

$$D_2^f = \frac{1}{4}\,\mathrm{Tr}\left(M_f^{-1}\frac{\partial^2 M_f}{\partial \mu_f^2}\right) - \frac{1}{4}\,\mathrm{Tr}\left(M_f^{-1}\frac{\partial M_f}{\partial \mu_f}M_f^{-1}\frac{\partial M_f}{\partial \mu_f}\right) \tag{2.73}$$

and

$$C_1^f = -\frac{1}{4}\,\mathrm{Tr}\left(M_f^{-1}\frac{\partial M_f}{\partial \mu_f}M_f^{-1}\right) \tag{2.74}$$

$$C_2^f = -\frac{1}{4}\,\mathrm{Tr}\left(M_f^{-1}\frac{\partial^2 M_f}{\partial \mu_f^2}M_f^{-1}\right) + \frac{2}{4}\,\mathrm{Tr}\left(M_f^{-1}\frac{\partial M_f}{\partial \mu_f}M_f^{-1}\frac{\partial M_f}{\partial \mu_f}M_f^{-1}\right)\,. \tag{2.75}$$

All higher orders can be derived simply by using the product rule and above identities. In general, the traces required for D_i^f and C_i^f contain only products of the inverse fermion matrix M^{-1} and higher orders of the local operator $\partial M/\partial\mu$. It follows from the Γ^5-hermiticity

$$M^\dagger(\mu) = \Gamma^5 M(-\mu)\Gamma^5 \qquad \text{and} \qquad \frac{\partial^n M^\dagger(\mu)}{\partial\mu^n} = (-1)^n\Gamma^5\frac{\partial^n M(-\mu)}{\partial\mu^n}\Gamma^5 \tag{2.76}$$

that these traces must obey

$$\mathrm{Tr}\left(\prod_i M_f^{-1}\frac{\partial^{n_i} M_f}{\partial \mu_f^{n_i}}\right)^* = (-1)^{\sum_i n_i}\,\mathrm{Tr}\left(\prod_i M_f^{-1}\frac{\partial^{n_i} M_f}{\partial \mu_f^{n_i}}\right)\,. \tag{2.77}$$

Therefore, C_n^f and D_n^f are imaginary for odd n, and real for even n as from the above equation follows that

$$D_n^{f\,*} = (-1)^n D_n^f \qquad \text{and} \qquad C_n^{f\,*} = (-1)^n C_n^f\,. \tag{2.78}$$

Random noise method. In practice, the individual traces can be stochastically estimated using the so-called random noise method [36]. In this method, the trace is replaced by a sum over N_S random noise vectors η_k each with the properties of white noise

$$\langle\eta_i\rangle = \lim_{N_S\to\infty}\frac{1}{N_S}\sum_{k=1}^{N_S}\eta_{ki} = 0\,, \qquad \langle\eta_i\eta_j\rangle = \lim_{N_S\to\infty}\frac{1}{N_S}\sum_{k=1}^{N_S}\eta_{ki}^*\eta_{kj} = \delta_{ij}\,. \tag{2.79}$$

Here, η_{ki} is component i of random vector k. On a single gauge configuration, the trace of e.g. products of matrix derivatives and inversions can be obtained as

$$\mathrm{Tr}\left(M^{-1}\frac{\partial^n M}{\partial\hat{\mu}^n}\right) = \lim_{N\to\infty}\frac{1}{N}\sum_{k=1}^{N}\eta_k^\dagger\, M^{-1}\frac{\partial^n M}{\partial\hat{\mu}^n}\,\eta_k\,. \tag{2.80}$$

This equation can be approximated by using only a finite number of random vectors. In these traces, each step of the form $M^{-1}(\partial M/\partial\hat{\mu})\eta_k = x$ is then obtained by solving

$$M\,x = \frac{\partial M}{\partial\hat{\mu}}\,\eta_k \tag{2.81}$$

using a Conjugate Gradient (CG) where x is the unknown vector. The product of the fermion matrix derivative with η_k is very similar to computing the Dslash operator of the HISQ action. When a chemical potential is introduced (see Sec. 1), all time-like links receive a factor $\exp(\pm\mu)$. Therefore, terms in the fermion action which contain products of k links receive a factor $\exp(\pm k\mu)$. For the Naik link k is equal to 3. To avoid confusion, we denote in the following the lattice coordinates with $n \equiv (n_t,\,\mathbf{n})$ and the unit vector in time direction with $\hat{t}$. In this notation, the derivative of the fermion matrix is given by

$$\begin{aligned}\left(\left.\frac{\partial^j M}{\partial(\mu)^j}\right|_{\mu=0}\chi\right)_n &= c_1\left(U_{n,t}\chi_{n+\hat{t}} - (-1)^j\,U^\dagger_{n-\hat{t},t}\chi_{n-\hat{t}}\right)\\ &\quad + 3^j c_3\left(N_{n,t}\chi_{n+3\hat{t}} - (-1)^j\,N^\dagger_{n-3\hat{t},t}\chi_{n-3\hat{t}}\right)\,.\end{aligned} \tag{2.82}$$

Here, the factors 3^j and $(-1)^j$ stem from the derivative of $\exp(\pm k\mu)$ taken at $\mu=0$. For the physical derivative w.r.t. μ/T, this equation needs to be multiplied with a factor $1/N_\tau^j$. It has been shown before that 1500 random vectors for all traces give reliable results for coefficients up to 6th order in μ as the stochastic noise is well reduced below the gauge noise [35]. In Fig. 2.1, we show the normalized error of

$$A_4^u = D_4^u + 4D_3^u D_1^u + 3D_2^{u2} + 6D_2^u D_1^{u2} + D_1^{u4} \tag{2.83}$$

as a function of the number of random vectors N_S averaged over 45 gauge configurations for two cases. In the first case, all individual traces in Eq. (2.83) are calculated with the same number of random vectors. In the second case, the trace D_1^u is always calculated with 1500 random vectors. By doing so, we greatly reduce the error even when using only a small N_S for the remaining traces. In particular, trace products which contain $D_1^{f^2}$ seem to be dominating the error. We conclude that when using 2000 random vectors for all D_1 traces and 500 for all others no additional bias is introduced. Additionally, a great reduction in computing time of about a factor 2 is achieved compared to the naive calculation where N_S is fixed to 1500 for all traces. The technique to calculate the error of individual traces as a function of the number of random vectors N_S has been described in [13].

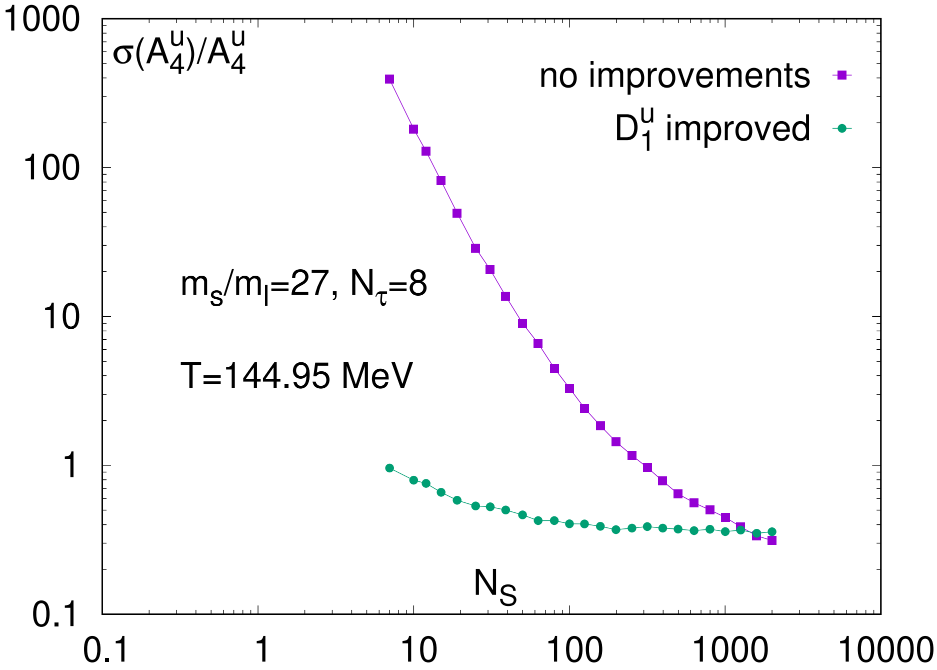

Figure 2.1: The standard error of A_4^u normalized with the mean of A_4^u as a function of the number of random vectors N_S. The traces were measured on 45 configurations from the $N_\tau = 8$ ensemble at a temperature of 144.95 MeV. Here, "improved" means that the trace D_1^u is calculated at each N_S with 1500 random vectors.

Unbiased estimators. When computing products of traces, e.g. $D_1^f D_2^f$, we have to take into account that D_1^f and D_2^f are correlated if derived from the same random noise vector. In particular for simulations with degenerate u and d quark, terms like $D_1^u D_1^d$ are most likely correlated as there is no difference between the operators D_1^u and D_1^d, thus, can be estimated with the same random vector set to save computing time. As long as the traces for quark flavor f and g were computed using different sets of random noise vectors no unbiased estimators have to be used. In order to remove the bias for all other cases, we can compute these products only for different random noise vectors, i.e. expectation values on a single gauge configuration require sums of the form $\sum_{i \neq j}$ where i and j label different random vectors. For a large number of random vectors, these sums consume a lot of computing time especially for e.g. ${D_1^f}^4$ which would require a sum similar to $\sum_{i \neq j \neq k \neq l}$. However, we can rewrite these sums in such a way that the required computing time scales linearly with the number of random vectors. We use the following unbiased estimators [37] for the expectation value of trace products on a single gauge configuration which are based on Newton-Girad formulae. We want to calculate product of traces of the form

$$\text{unbiased}\left(\prod_{i=1}^{N_{tr}} a_i^{\gamma_i}\right) = \frac{\prod_{i=1}^{N_{tr}} \gamma_i!}{N_S(N_S-1)\cdots(N_S-|\gamma|+1)} e_\gamma \tag{2.84}$$

where N_{tr} is the total number of traces, a_i a specific trace operator and γ_i the corresponding power of trace a_i. The unbiased estimate e_γ can be expressed as

$$e_\gamma = -\frac{1}{|\gamma|} \sum_{\alpha+\beta=\gamma, \alpha\neq(0,0,\cdots,0)} (-1)^{|\alpha|} \binom{|\alpha|}{\alpha} p_\alpha e_\beta \tag{2.85}$$

with

$$e_{(0,0,\cdots,0)} = 1 \; . \tag{2.86}$$

Here, γ, β and α are integer valued vectors with dimension equal to the total number of traces in the product and $\binom{|\alpha|}{\alpha}$ is the multinomial coefficient. The vector γ contains the power exponents of each trace. The sum in Eq. (2.85) has to be understood as the sum over all possible combinations which fulfill $\alpha + \beta = \gamma$ while leaving out the case where all components of α are zero. The power sums p_α are defined as

$$p_\alpha = \sum_{j=1}^{N_S} \prod_{i=1}^{N_{tr}} a_{i,j}^{\alpha_i} \tag{2.87}$$

where $a_{i,j}$ is the i-th trace calculated using the j-th random vectors. E.g., the unbiased trace product of the form AB^2 would correspond to $\gamma = (1, 2)$ and translates into

$$\left\langle A\, B^2 \right\rangle_v = \frac{\sum_i A_i \left(\sum_i B_i\right)^2 - \sum_i A_i \sum_i B_i^2 - 2\sum_i A_i B_i \sum_i B_i + 2\sum_i A_i B_i^2}{N_S(N_S-1)(N_S-2)} \; . \tag{2.88}$$

Here, A_i and B_i are arbitrary traces of operators calculated using the i-th random noise vector and $\langle\cdot\rangle_v$ denotes the expectation value over random vectors on a single configuration.

Deflated Conjugate Gradient. The computing time required to solve a single random vector, as required in Eq. (2.81), is dominated by low-lying eigenvalues of $-M^\dagger M$. We can reduce the CG iteration count by computing an initial guess x_0 for the CG using the lowest N_{ev} eigenvalues λ_i and eigenvectors q_i. It is given by

$$x_0 = \sum_{i=1}^{N_{ev}} \frac{\langle q_i, \eta_k \rangle}{\lambda_i} \; . \tag{2.89}$$

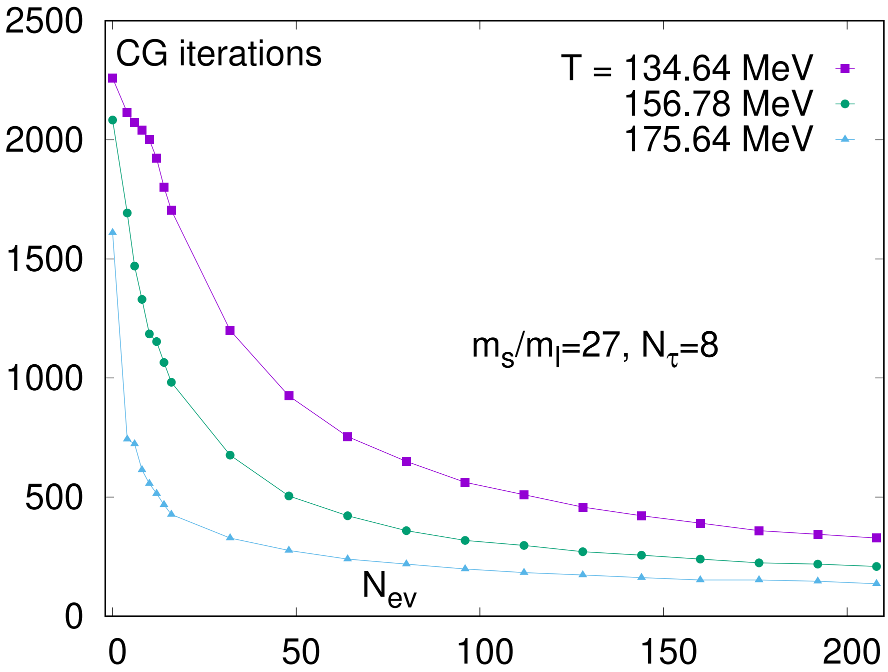

Figure 2.2: The required number of CG iterations for computing $\mathrm{Tr}\, M^{-1}$ as a function of the number of eigenvectors N_{ev} for reaching a residual of 10^{-6}. The tests were performed on a single $N_\tau = 8$ configuration for three temperature values.

By using this initial guess, the CG only has to solve the remaining high mode part of the problem. The eigenvectors and eigenvalues can be computed with a Kalkreuter-Simma algorithm [38] or a Lanczos [39]. In Fig. 2.2, we show the required CG iterations to reach a residual of 10^{-6} when computing the chiral condensate, i.e. solving $Mx = \eta_k$, as a function of the number of eigenvectors N_{ev}. We achieve a speed-up of 6 to 8 depending depending on the temperature. Typically, configurations at lower temperatures have smaller eigenvalues, thus, deflation is more effective. In our simulations, we use always 256 eigenvectors as there is still a speed-up of about 1.4 when going from 192 to 256 eigenvectors. Deflation only helps to reduce computing time and has no effect on the accuracy as the CG always converges into the same minimum.

Linear-μ formulation. As discussed in Sec. 1, the chemical potential can be introduced by multiplying all time-like forward links with μ and all time-like backward links with $-\mu$. However, this formulation does not achieve the correct continuum limit as UV divergences still survive for Taylor coefficients of the pressure in the orders $\mathcal{O}(\mu^2)$ and $\mathcal{O}(\mu^4)$. It has been shown successfully [27, 28] for the pressure expansion that divergences stem from the free case in order $\mathcal{O}(\mu^2)$ and $\mathcal{O}(\mu^4)$, as well as that higher orders do not show any difference between linear-μ and exponential-μ, thus, are divergence free. In the

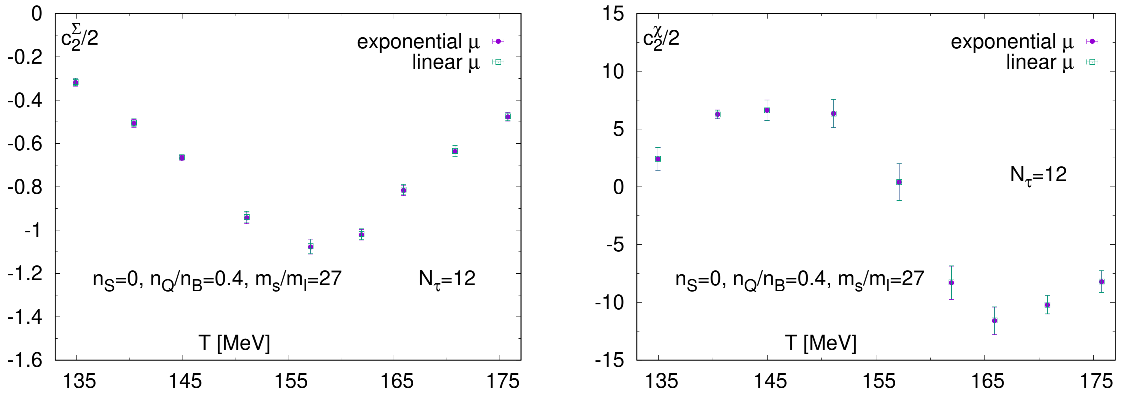

Figure 2.3: The 2nd order Taylor expansion coefficient of the subtracted condensate (left) and the disconnected two-flavor susceptibility (right) for a lattice spacing with $N_\tau = 12$ in a strangeness neutral system calculated using the exponential-μ (purple) and linear-μ (green) formulation.

following, we argue schematically that for the chiral condensate and chiral susceptibility only the 2nd order in μ does not produce the physical value in the continuum limit when using the linear-μ formulation [40]. On the lattice, the pressure expansion in linear-μ formulation is given by

$$a^4\left(P(T,\mu) - P(T,0)\right) = a^4 P_{\text{phys}} + a^4 P_{\text{div}} \tag{2.90}$$

where P_{phys} is the physical pressure without the leading order. The term P_{div} contains all the divergences which originate from the linear-μ formulation. In the free case, P_{div} can be described as a joined expansion in μ and mass m. It is given by

$$a^4 P_{\text{div}} = \sum_{n=0}^{\infty} (am)^{2n} \sum_{k=1}^{\infty} c_{nk} (a\mu)^{2k} \tag{2.91}$$

where c_{nm} are the expansion coefficients. We have made clear that the expansion has to be even in m due to chiral symmetry. Relevant for this discussion are only the leading and next-to-leading orders in m as higher orders vanish in the continuum limit. After truncating the series after the relevant orders, we find

$$\begin{aligned} a^4 P_{\text{div}} = {} & (am)^0 \left(c_{01}(a\mu)^2 + c_{02}(a\mu)^4 + c_{03}(a\mu)^6 + \cdots\right) \\ & + (am)^2 \left(c_{11}(a\mu)^2 + c_{12}(a\mu)^4 + c_{13}(a\mu)^6 + \cdots\right) + \cdots \,. \end{aligned} \tag{2.92}$$

As can be seen in the above equation, P_{div} itself has a divergence proportional to a^{-2} in the c_{01} term. Additionally, the terms c_{11} and c_{02} have a constant contribution to P_{div} as they do not vanish in the continuum limit. This is why the 2nd and 4th μ derivative of the pressure do not achieve the correct continuum limit. From this point, we are able

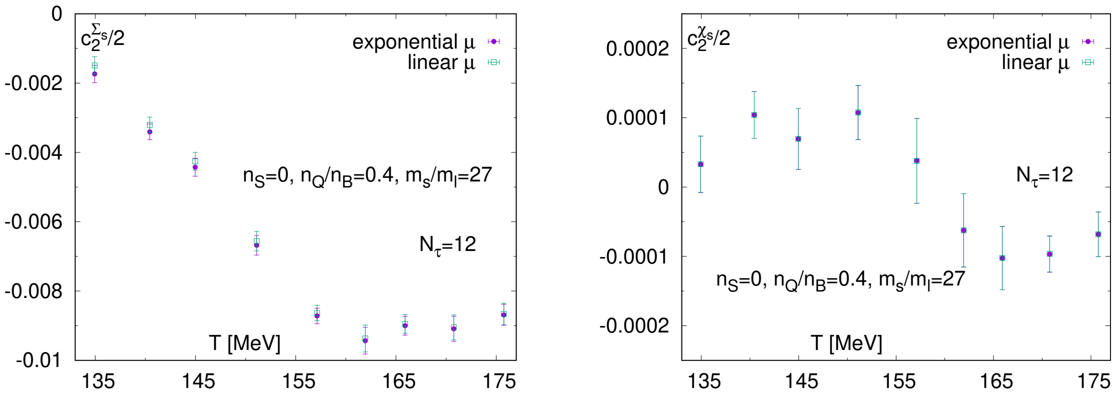

Figure 2.4: The 2nd order Taylor expansion coefficient of the strange condensate (left) and the disconnected strange susceptibility (right) for a lattice spacing with $N_\tau = 12$ in a strangeness neutral system calculated using the exponential-μ (purple) and linear-μ (green) formulation.

to give similar arguments for the chiral condensate and chiral susceptibility by taking further mass derivatives of P_{div}. The chiral condensate contribution from P_{div} is given by

$$a^3\Sigma_{\text{div}} = 2am\left(c_{11}(a\mu)^2 + c_{12}(a\mu)^4 + c_{13}(a\mu)^6 + \cdots\right) + \cdots \; . \tag{2.93}$$

We find that the 2nd order has a constant contribution in the continuum limit while higher orders are free of divergent terms. For the chiral susceptibility, we find similarly that

$$a^2\chi_{\text{div}} = 2\left(c_{11}(a\mu)^2 + c_{12}(a\mu)^4 + c_{13}(a\mu)^6 + \cdots\right) + \cdots \tag{2.94}$$

has a constant contribution from the c_{11} term. However, in this work we study the Taylor expansion of the disconnected susceptibility for which the physical value is exactly zero in the free case. Therefore, the series of the disconnected susceptibility starts in order $(am)^2$ and thus all orders are expected to be free of divergent as well as constant terms. These dimensional arguments for the condensate and susceptibility are in good agreement with our findings when comparing actual simulations using both μ formulations. In Fig. 2.3, we compare exponential-μ and linear-μ formulation for the 2nd order of the subtracted condensate and disconnected susceptibility. A relatively small difference is visible for the condensate as all linear-μ values are systematically slightly higher. This discrepancy seems to be highly mass dependent as for the expansion of the strange condensate we observe larger difference for the 2nd order (see Fig. 2.4). As expected, no difference is visible for the two-flavor disconnected susceptibility (see Fig. 2.3) and the strange disconnected susceptibility (see Fig. 2.4) in 2nd order. We conclude that it is valid to use the linear-μ formulation for the condensate starting at 4th order and for the disconnected susceptibility in all orders.When using the linear-μ formulation, the equations for C_n^f and D_n^f are greatly simplified as derivatives $\partial^n M/\partial\mu^n$ are equal to zero for $n > 1$. They are given by

$$D_n^f = \frac{1}{4}(-1)^{n+1}\,(n-1)!\,\mathrm{Tr}\left[\left(M_f^{-1}\frac{\partial M_f}{\partial \mu_f}\right)^n\right] \tag{2.95}$$

and

$$C_n^f = \frac{1}{4}(-1)^n\,n!\,\mathrm{Tr}\left[\left(M_f^{-1}\frac{\partial M_f}{\partial \mu_f}\right)^n M_f^{-1}\right]\,. \tag{2.96}$$

This simplification directly translates into a significant reduction in computing time of about a factor 4 as the number of required fermion matrix inversions reduces from 35 to 9 when computing coefficients of the pressure up to 8th order. Note that when computing all required traces for the pressure up to e.g. 8th order, we can only compute the expansion of the condensate and the disconnected susceptibility up to 6th order.

3 The QCD crossover at zero chemical potential

We extract the crossover temperature T_0 from the inflection point of the condensate and the maximum of the susceptibility. For this, we calculate the first and second T derivatives of Σ_{sub} and $\chi_{\text{disc/sub}}$, respectively, from a combined fit of the data using several Padé approximations $[m,n]$ up to order $m+n<8$. We use the Akaike information criterion (AIC) to give each Padé approximation a weight to determine the mean and the systematic error. The statistical error is estimated using a statistical bootstrap [14]. Using these weighted Padé sums, we are able to calculate T derivatives as required for Eq. (2.5) and Eq. (2.12). These equations are solved numerically for T_0. In the following section, we describe and test the validity of the Padé AIC fit method for a problem where the exact solution is known.

3.1 Padé AIC fit method

Given a data set with N points including errors, we fit several Padé approximations $[m,n]$ of the form

$$P(T) = \frac{\sum_{i=0}^{m} a_j T^j}{1+\sum_{k=1}^{n} b_k T^k} \qquad \text{with} \qquad m+n<N \tag{3.1}$$

to the data. Here, a_i and b_k are real coefficients. If the data can be described well by Padé approximations, different values for $[m,n]$ give similar results. However, for small data sets it is important to carefully tune the initial guess of each fit. From now on, we speak of a models instead of Padé approximations. Following [41], in a set of R models the best model is given by the smallest AIC_c value

$$\text{AIC}_c = 2k + \frac{2k(k+1)}{N-k-1} + \chi^2 \tag{3.2}$$

where k is the number of parameters in a model and χ^2 is given by a fit of a model to the data. This definition of AIC_c assumes Gaussian distributed errors. It is important to note that the smallest AIC_c value only finds the best model in the given set. Therefore, it is crucial to provide reasonable good models. However, the AIC method can suffer from model selection uncertainties. This is why it is advantageous to average over all models using weights defined by

$$w_i = \frac{\exp(-\frac{1}{2}\Delta_i)}{\sum_{r=1}^{R}\exp(-\frac{1}{2}\Delta_r)} \tag{3.3}$$

where

$$\Delta_i = \text{AIC}_{c,i} - \text{AIC}_{\text{min}} \tag{3.4}$$

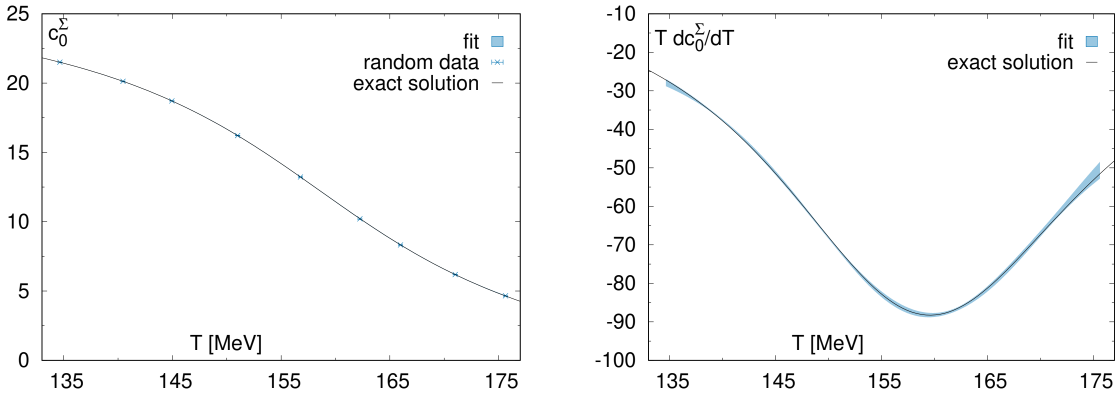

Figure 3.1: The fake subtracted condensate (left) and its first T derivative (right). It has been generated by using ansatz (3.7) which is shown as the black line. The blue data points were generated from this ansatz in combination with random noise. The blue band corresponds to the Padé AIC model mean which includes systematic and statistical errors.

is the AIC$_c$ difference of model i to the best model wit AIC$_c$ $\equiv$ AIC$_{\text{min}}$. The model mean is then given by

$$\overline{P}(T) = \sum_{i=0}^{R} w_i P_i(T) \ . \tag{3.5}$$

Still, models P_i which are not physical should be discarded by hand. Even with a comparably small weight w_i, poles in P_i can have a significant contribution to $\overline{P}$. The variance of $\overline{P}$ can be calculated by

$$\operatorname{var}\left(\overline{P}(T)\right) = \left(\sum_{i=0}^{R} w_i \sqrt{\operatorname{var}(P_i(T)) + \left(P_i(T) - \overline{P}(T)\right)^2}\right)^2 \tag{3.6}$$

where var$(P_i(T))$ is the statistical variance of model P_i, e.g. estimated by a statistical bootstrap. In order to test the quality of the model mean $\overline{P}(T)$ for physical observables when having only a small number of data points, we generated random data using an ansatz

$$c_0^\Sigma(T) = A + B\arctan(C(T - T_0)) \tag{3.7}$$

which should be a good approximation of the chiral condensate c_0^Σ at vanishing chemical potential. We determined reasonable values for the parameters A, B, C and T_c by fitting the ansatz to our $N_\tau = 8$ ensemble. Using this ansatz, we generated data points at 9 temperatures as also used in our simulations. We then added random noise to the mean

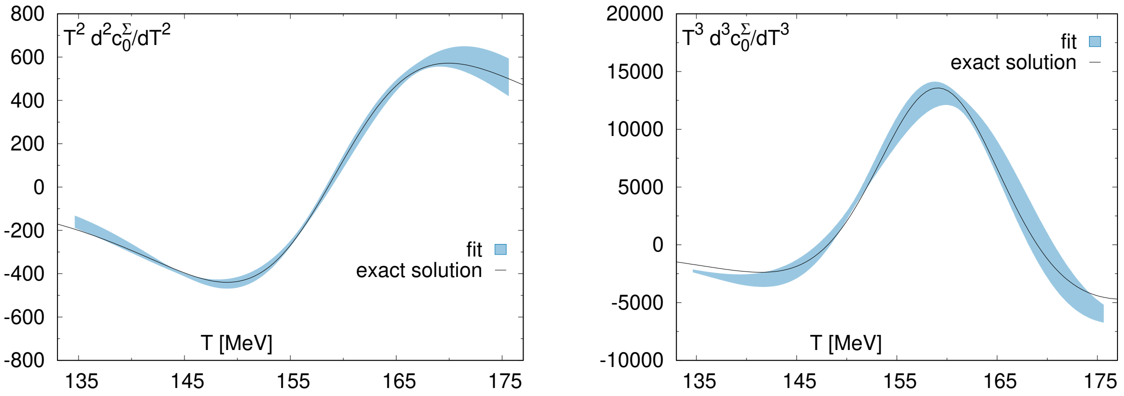

Figure 3.2: The 2nd (left) and 3rd (right) T derivative of the fake subtracted condensate. It has been generated by using ansatz (3.7) which is shown as the black line. The blue band corresponds to the Padé AIC model mean which includes systematic and statistical errors.

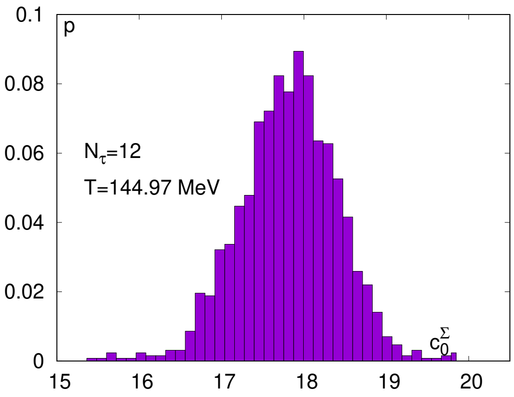

Figure 3.3: Histogram for the subtracted two-flavor chiral condensate. The probability p has been calculated by dividing a $N_\tau = 12$ ensemble at $T = 144.97$ MeV in about 1200 samples where each sample consists of about 60 configurations.

of each data point and included errors of similar magnitude as for the $N_\tau = 8$ ensemble. As constructed, the data points agree with the ansatz within errors. In Fig. 3.1, we show the ansatz in comparison to the random data points and the model mean. We found that within errors the model mean agrees with the exact solution. In particular for determining T_c from the second T derivative of the condensate as well as the curvature of the crossover line, it is important to study the quality of T derivatives of $\overline{P}$. In Fig. 3.1 and Fig. 3.2, we compare derivatives of $\overline{P}(T)$ up to 3rd order to the exact derivatives. For all orders, we observe in the crossover region excellent agreement within $1\,\sigma$ to the exact derivatives. Only the third derivative of the condensate shows a discrepancy at

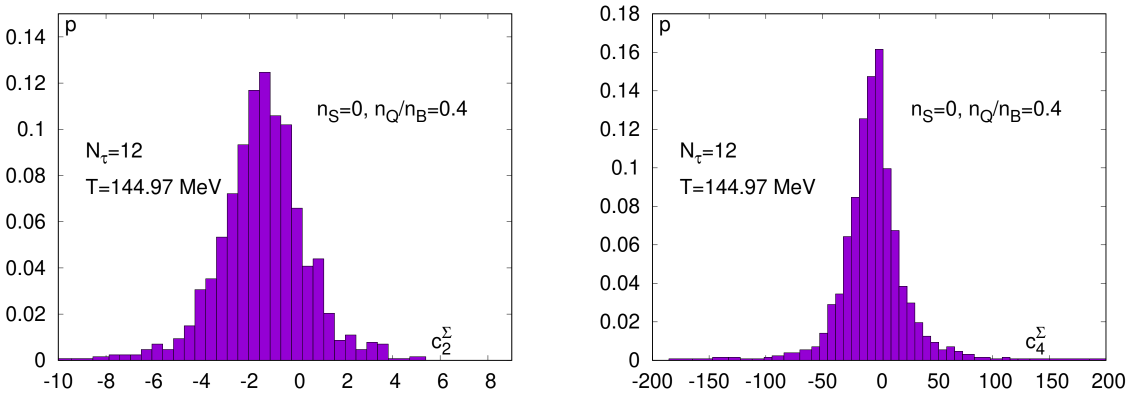

Figure 3.4: Histograms for the 2nd (left) and the 4th order (right) Taylor expansion coefficient of the subtracted two-flavor chiral condensate in a constrained case with $n_S = 0$ and $n_Q/n_B = 0.4$. The probability p has been calculated by dividing a $N_\tau = 12$ ensemble at $T = 144.97$ MeV in about 1200 samples where each sample consists of about 60 configurations.

the borders which is still within $3\,\sigma$. However, it is expected that these fits fail at the borders due to missing information about the low and high T behavior. Nevertheless, in this work only the results close to T_0 are important. We conclude that the Padé AIC fit method is a robust tool to determine fits close to T_0 which produce good behavior even at higher derivatives within errors. In Fig. 3.3, we show the distribution of the subtracted condensate for our $N_\tau = 12$ ensemble at a temperature below T_0. The subtracted condensate is Gaussian distributed as required for the here described method. In Sec. 4.1, we fit higher order Taylor expansion coefficients using this method. Their distribution is shown in Fig. 3.4 and is also Gaussian. Additionally, we verified that the distribution of the chiral susceptibility is Gaussian. Therefore, we can use the Padé AIC fit method for higher order Taylor expansion coefficients for all observables considered in this work.

3.2 Determination of T_0

In Fig. 3.5 and Fig. 3.6, we show the condensate and susceptibility normalized using the f_K scale of $155.7(9)/\sqrt{2}$ MeV. We have data for $N_\tau = 6, 8, 12$ and 16 in the temperature range of 135 MeV to 175 MeV. The temperature has been fixed using the f_K scale as described in [32]. The temperature range is sufficient to determine the peak location of the susceptibility for $N_\tau = 6, 8$ and 12 with an uncertainty of about 0.2 MeV. For $N_\tau = 16$, the errors are about 10 times larger. Given the small errors of the susceptibility itself, the Padé fits are very stable and show no dependency on the low or high temperature data points. The significant contribution comes from data points around T_0. Having more data points at low and high temperatures only helps to stabilize

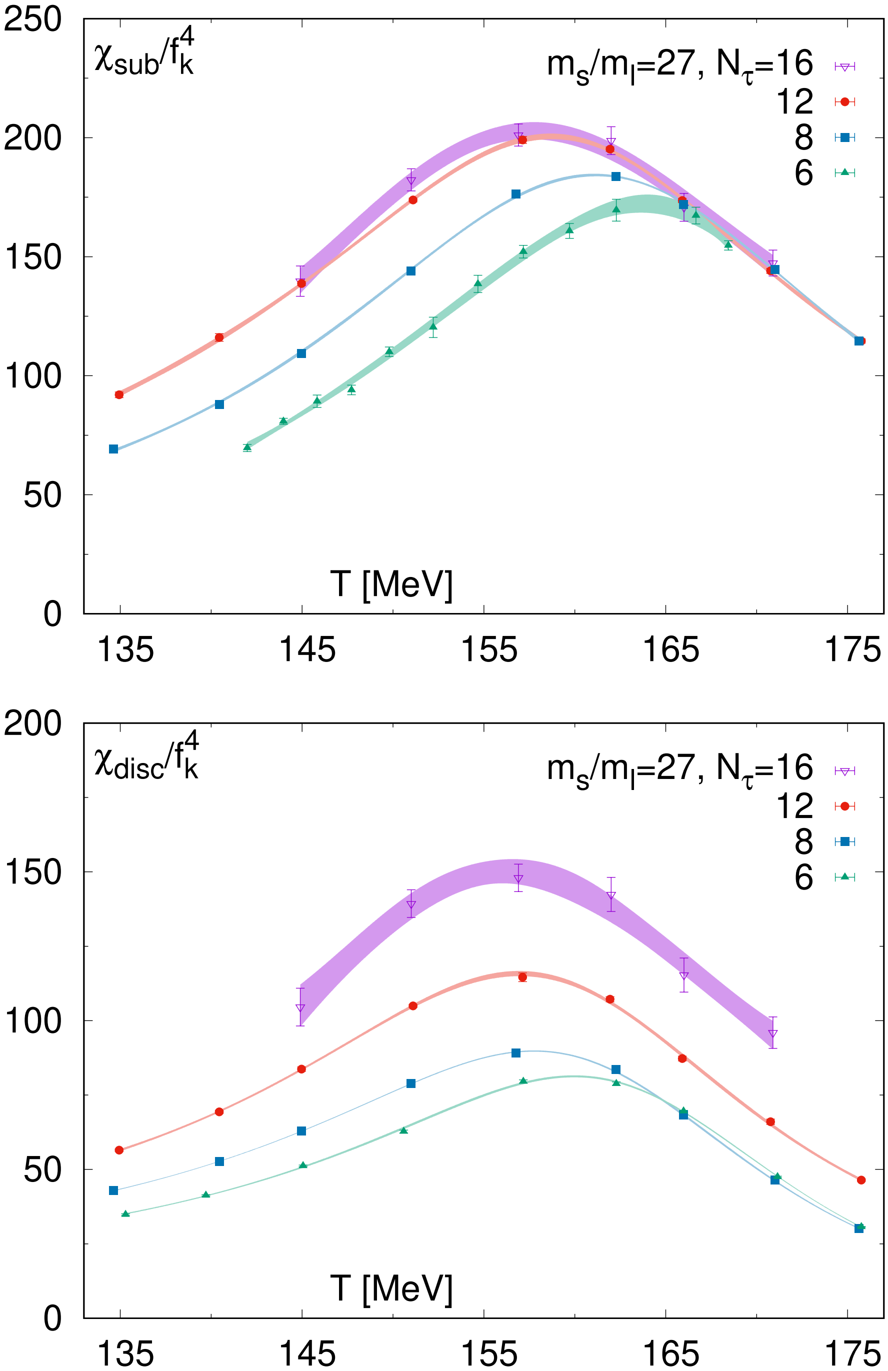

Figure 3.5: The subtracted susceptibility (top) and the disconnected susceptibility (bottom) as a function of the temperature for different N_τ. The data is plotted in two-flavor formulation and normalized using the kaon decay constant f_K. The colored bands are given by the AIC weighted Padé approximations and include statistical as well as systematic errors.

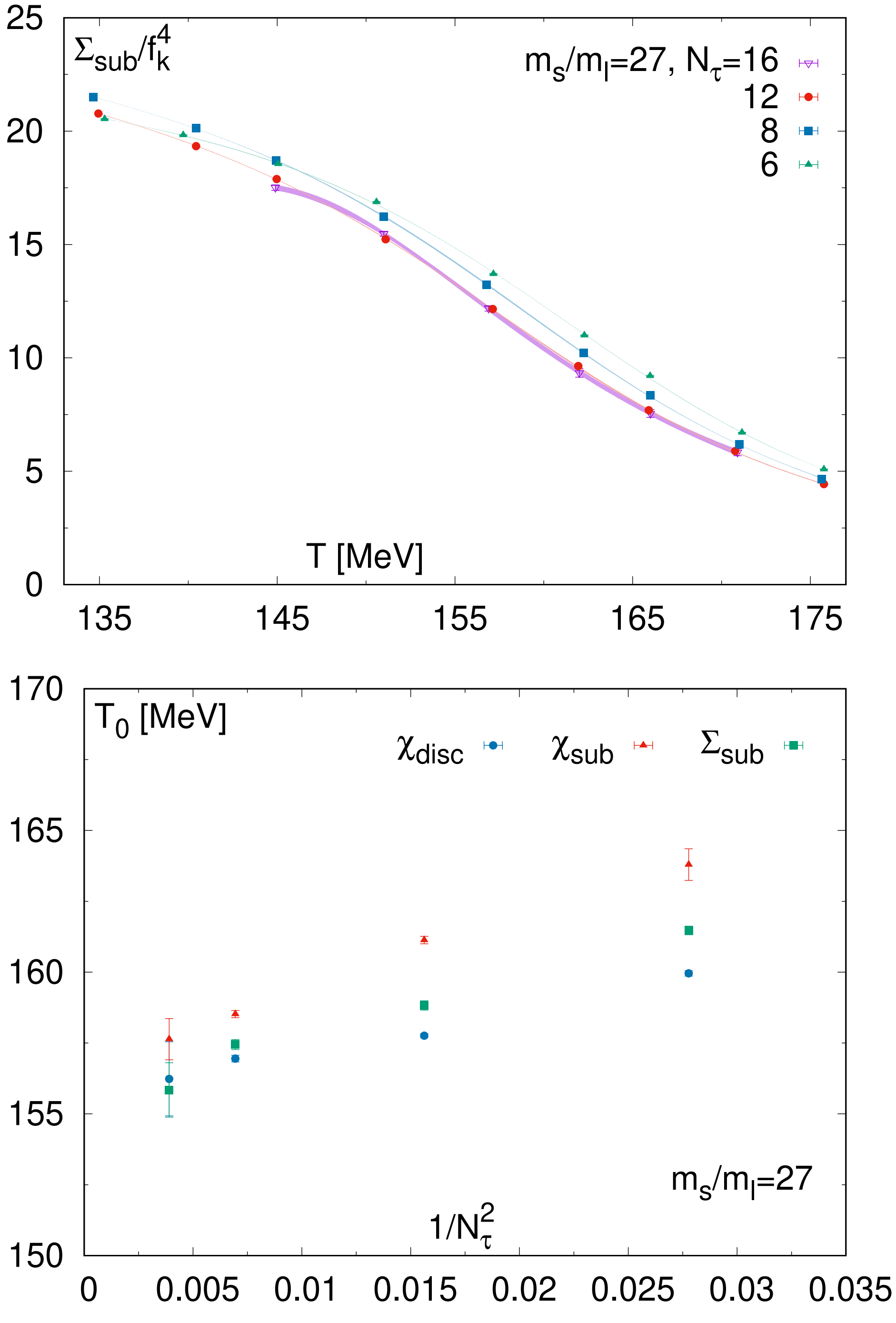

Figure 3.6: The subtracted condensate (top) as a function of the temperature for different N_τ. The data is plotted in two-flavor formulation and normalized using the kaon decay constant f_K. The colored bands are given by the AIC weighted Padé approximations and include statistical as well as systematic errors. In the bottom, we show the obtained chiral crossover temperatures T_0 from four lattice spacings with $N_\tau = 6, 8, 12$ and 16 as a function of $1/N_\tau^2$.

N_τ		$T_0(\Sigma_{\mathrm{sub}})$	$T_0(\chi_{\mathrm{sub}})$	$T_0(\chi_{\mathrm{disc}})$	[MeV]
6		161.5(2)	163.8(6)	160.0(1)	
8		158.8(2)	161.1(2)	157.8(1)	
12		157.4(2)	158.5(2)	157.0(2)	
16		155.8(10)	157.6(7)	156.2(13)	
∞		155.9(2)	156.6(2)	155.6(2)	
∞	excluding $N_\tau = 6$	156.2(3)	156.4(2)	156.3(2)	

Table 3.1: The chiral crossover temperature T_0 in MeV extracted from AIC weighted Padé fits to the condensate and susceptibility at vanishing chemical potential. All observables use the two-flavor formulation. We show continuum extrapolated values for T_0 from a bootstrap using an ansatz with $\mathcal{O}(N_\tau^{-2})$ corrections. The last row shows the effect of a continuum extrapolation without $N_\tau = 6$.

N_τ		$T_0\,(\Sigma_{\mathrm{sub}})$	[MeV]	(r_1 scale)
6		168.4(3)		
8		163.0(2)		
12		158.9(2)		
16		156.5(10)		
∞		155.7(2)		
∞	excluding $N_\tau = 6$	155.6(3)		

Table 3.2: The values for the chiral crossover temperature T_0 in MeV extracted from the subtracted condensate using the r_1 scale [32] (see Tab. 3.1 for f_K scale).

the statistical bootstrap. Determining the inflection point of the condensate is typically more prone to systematic errors. In particular, it is not possible to leave out low or high temperature data points as the fits become unstable and cannot interpolate the data. This is why the condensate gives slightly larger errors for T_0. As expected, we observe for all observables in Fig. 3.6 that T_0 shifts to smaller values for increasing N_τ. For the subtracted observables[4], the difference between our $N_\tau = 12$ and $N_\tau = 16$ ensemble is small which may indicated that these observables are already close to the continuum. However, the disconnected susceptibility still shows significant cut-off effects even at large N_τ values. The extracted T_0 values are summarized in Tab. 3.1. We bootstrap a continuum extrapolation using an ansatz with $\mathcal{O}(N_\tau^{-2})$ corrections with and without our smallest $N_\tau = 6$ ensemble. For the subtracted observables, we cannot observe a difference by excluding $N_\tau = 6$ given that both extrapolations agree within errors. Due to the larger cut-off effects in the disconnected susceptibility, we see a significant difference of about 1 MeV between both extrapolations. Taking only the chiral observables Σ_{sub}, χ_{sub} and χ_{disc} into account, the chiral crossover at vanishing chemical potential must occur in

---

[4] The $N_\tau = 6$ subtracted susceptibility has been measured by Sheng-Tai Li. The $N_\tau = 16$ subtracted condensate and subtracted susceptibility have been measured by Nikhil Karthik.

N_τ	$T_0\left(c_2^\Sigma\right)$	$T_0\left(c_2^\chi\right)$	[MeV]
6	161.3(3)	158.9(6)	
8	160.1(2)	157.9(3)	
12	157.7(5)	156.6(12)	
∞	157.8(5)	156.4(9)	

Table 3.3: The values for the chiral crossover temperature T_0 in MeV extracted from the 2nd order expansion coefficient of the subtracted condensate and the disconnected susceptibility in case of vanishing μ_Q and μ_S (see Sec. 4.1). All observables use the two-flavor formulation. We show continuum extrapolated values for T_0 from a bootstrap using an ansatz with $\mathcal{O}(N_\tau^{-2})$ corrections.

the temperature range from 155.4 MeV to 156.8 MeV. We crosschecked our analysis by using smoothing splines[5] which show similar values for T_0 compared to the Padé analysis. In Tab. 3.2, we show the crossover temperature extracted from the condensate using the r_1 scale [32]. At finite N_τ, we see a significant difference to the f_K scale of about 7 MeV for $N_\tau = 6$ and about 1 MeV for $N_\tau = 16$. As expected, in the continuum limit the difference to $T_0(\chi_{\text{sub}})$ using the f_K scale is small and less than 0.3 MeV. However, this good agreement might only be accidental as the typical error for fixing the temperature using r_1 or f_K as a scale is of about 1 MeV [32, 17]. This systematic error is not included in the T_0 values shown in our tables and figures.

Additionally, we extract T_0 from the 2nd order expansion coefficient (see Sec. 4.1) of the subtracted condensate and the disconnected susceptibility as they should also diverge in the chiral limit. In these cases, T_0 is defined by

$$c_2^\chi = 0 \qquad \text{and} \qquad \frac{d}{dT} c_2^\Sigma = 0 \tag{3.8}$$

and shown in Tab. 3.3 in combination with the continuum extrapolated values. In theory, these should be similar to the crossover temperatures from the subtracted condensate and the disconnected susceptibility. For each N_τ, the temperatures T_0 agree with eachother as well as the continuum T_0 from c_2^χ within errors. However, the continuum T_0 from c_2^Σ deviates by about 1 MeV to $T_0(\Sigma_{\text{sub}})$.

Our final values for the crossover temperature including statistical and systematic errors are: 155.9(2)(10) MeV for the subtracted condensate, 156.6(2)(10) MeV for the subtracted susceptibility and 155.6(2)(10) MeV for the disconnected two-flavor susceptibility. Here, the first bracket stands for the statistical and systematic error resulting from the Padé AIC fits, and the second bracket denotes the systematic error from setting the scale which is about 1 MeV as discussed above. We have shown that the difference in the continuum limit between the r_1 scale and the f_K scale is insignificant for T_0, thus, can be neglected.

---

[5] The smoothing splines were generated by Swagato Mukherjee.

The latest value for the crossover temperature at vanishing chemical potential using the HISQ action with physical quark masses can be found in [32]. They report a value for the crossover temperature of 154(9) MeV from a scaling analysis of the renormalized two-flavor total susceptibility. This value is in good agreement with our determination of T_0 given the rather large errors. Compared to our results, we drastically reduce the error by about a factor 50 as expected due to increased statistics.

The publication [42] has studied the subtracted light quark condensate using the stout action with physical quark masses. They report a value of 157(3)(3) MeV for the crossover temperature T_0 which is about 1 MeV larger than our value. Still, within errors it agrees with our results. Additionally, they show a T_0 of 147(2)(3) MeV for some light quark susceptibility normalized with T^4. Using this T^4 normalization shifts the pseudo-critical temperature to smaller values. It is not clear from their publication and references which definition has been used for the susceptibility, thus, a direct comparison to our data is not possible.

There is another publication [43] which also determined T_0 using the stout action with physical quark masses. They report 154.7(8) MeV for the subtracted condensate and 154.4(8) MeV for the renormalized light quark susceptibility.

4 The curvature of the QCD crossover line

The QCD crossover line can be parameterized as

$$\frac{T_c(\mu_B)}{T_0} = 1 - \kappa_2 \left(\frac{\mu_B}{T_0}\right)^2 - \kappa_4 \left(\frac{\mu_B}{T_0}\right)^4 + \mathcal{O}(\mu_B^6) \tag{4.1}$$

where T_0 is the pseudo-critical temperature at vanishing chemical potential. The curvature coefficients κ_n can be obtained by requiring that each order μ_B^n in

$$\frac{d}{dT}\frac{\chi_{\rm disc}(T,\hat{\mu}_B)}{f_K^4} \equiv 0 \qquad \text{and} \qquad \frac{d^2}{dT^2}\frac{\Sigma_{\rm sub}(T,\hat{\mu}_B)}{f_K^4} \equiv 0 \ . \tag{4.2}$$

vanishes. Note that it is also common to formulate Eq. (4.2) using partial T derivatives evaluated at constant μ_B/T. However, we have compared both definitions and did not find any difference for the mean of κ_2 and κ_4 as well as the corresponding errors. From now on, we use only Eq. (4.2).

4.1 Systems with vanishing μ_Q and μ_S

The Taylor expansions for vanishing μ_Q and μ_S are given only by μ_B derivatives, i.e. the coefficients from Sec. 2.2 for the subtracted chiral condensate $\Sigma_{\rm sub}$ simplify to

$$c_n^{\Sigma} = \Omega_{n00}^{BQS} \tag{4.3}$$

and for the disconnected chiral susceptibility $\chi_{\rm disc}$ to

$$c_n^{\chi} = \Xi_{n00}^{BQS} \ . \tag{4.4}$$

In the following, we derive κ_2 from the coefficients of the chiral susceptibility. First, we expand the susceptibility in T and $\hat{\mu}_B$ around $(T_0, \hat{\mu}_B = 0)$. The relevant terms for κ_2 are given by

$$\begin{aligned} \frac{\chi_{\rm disc}(T,\mu_B)}{f_K^4} &= c_0^{\chi}|_{(T_0,0)} + \left.\frac{\partial c_0^{\chi}}{\partial T}\right|_{(T_0,0)} (T-T_0) + \frac{1}{2}\left.\frac{\partial^2 c_0^{\chi}}{\partial T^2}\right|_{(T_0,0)} (T-T_0)^2 \\ &+ \frac{1}{2}\, c_2^{\chi}|_{(T_0,0)}\, \hat{\mu}_B^2 + \frac{1}{2}\left.\frac{\partial c_2^{\chi}}{\partial T}\right|_{(T_0,0)} (T-T_0)\hat{\mu}_B^2 + \ldots \ . \end{aligned} \tag{4.5}$$

Taking into account that the first T derivative of $\chi_{\rm disc}$ is zero at T_0 and not writing terms which have no contribution to order μ_B^2, we obtain for the T derivative of the Taylor expansion

$$\begin{aligned} \frac{d}{dT}\frac{\chi_{\rm disc}(T,\mu_B)}{f_K^4} &= \left.\frac{\partial^2 c_0^{\chi}}{\partial T^2}\right|_{(T_0,0)} (T-T_0) - c_2^{\chi}|_{(T_0,0)} \frac{\mu_B^2}{T^3} + \frac{1}{2}\left.\frac{\partial c_2^{\chi}}{\partial T}\right|_{(T_0,0)} \hat{\mu}_B^2 + \ldots \\ &= \left(\frac{1}{2}\left.\frac{\partial c_2^{\chi}}{\partial T}\right|_{(T_0,0)} \frac{1}{T_0^2} - \left.\frac{\partial^2 c_0^{\chi}}{\partial T^2}\right|_{(T_0,0)} \frac{\kappa_2}{T_0} - c_2^{\chi}|_{(T_0,0)} \frac{\mu_B^2}{T_0^3} \right) \mu_B^2 + \mathcal{O}(\mu_B^4) \ . \end{aligned} \tag{4.6}$$

In the last step, we used that the equation is only equal to zero at the crossover temperature, i.e. has to be evaluated at $T = T_c(\mu_B)$. In combination with Eq. (4.1), the difference $T - T_0$ can be written as

$$T - T_0 \equiv T_c(\mu_B) - T_0 = -\kappa_2 \frac{\mu_B^2}{T_0} + \mathcal{O}(\mu_B^4) \tag{4.7}$$

and $1/T^3$ as

$$\frac{1}{T^3} = \frac{1}{T_0^3} \left(1 + 3\kappa_2 \left(\frac{\mu_B}{T_0} \right)^2 + \mathcal{O}(\mu_B^4) \right) \, . \tag{4.8}$$

By demanding that the order $\mathcal{O}(\mu_B^2)$ vanishes, we find that

$$\kappa_2^\chi = \frac{1}{2T_0^2} \frac{T_0 \left. \frac{\partial c_2^\chi}{\partial T} \right|_{(T_0,0)} - 2 \, c_2^\chi |_{(T_0,0)}}{\left. \frac{\partial^2 c_0^\chi}{\partial T^2} \right|_{(T_0,0)}} \, . \tag{4.9}$$

Note that κ_2 is independent of the f_K normalization used in the expansion coefficients c_n^χ. Similarly, we find that the second curvature coefficient can be determined from the subtracted condensate as

$$\kappa_2^\Sigma = \frac{1}{2T_0^3} \frac{6 \, c_2^\Sigma |_{(T_0,0)} - 4T_0 \left. \frac{\partial c_2^\Sigma}{\partial T} \right|_{(T_0,0)} + T_0^2 \left. \frac{\partial^2 c_2^\Sigma}{\partial T^2} \right|_{(T_0,0)}}{\left. \frac{\partial^3 c_0^\Sigma}{\partial T^3} \right|_{(T_0,0)}} \, . \tag{4.10}$$

However, determining κ_2 from the condensate requires higher T derivatives of the expansion coefficients compared to from the susceptibility which leads to higher systematic errors. The T derivatives of all expansion coefficients can be analytically obtained by derivating the AIC weighted Padé sums. The equation for κ_4 derived from the disconnected susceptibility is given by requiring that $\mathcal{O}(\mu_B^4)$ in Eq. (4.6) vanishes. It reads

$$\kappa_4^\chi = \frac{1}{24T_0^2} \frac{-72\kappa_2^\chi c_2^\chi - 4c_4^\chi + T_0 \left[\frac{\partial c_4^\chi}{\partial T} + 12\kappa_2^\chi \left(4\frac{\partial c_2^\chi}{\partial T} - T_0 \frac{\partial^2 c_2^\chi}{\partial T^2} + \kappa_2^\chi T_0^2 \frac{\partial^3 c_0^\chi}{\partial T^3} \right) \right]}{\frac{\partial^2 c_0^\chi}{\partial T^2}} \tag{4.11}$$

where all coefficients and their derivatives have to be evaluated at $(T_0, \hat{\mu}_B = 0)$. For the subtracted condensate the 4th order curvature coefficient is given by

$$\begin{aligned} \kappa_4^\Sigma = {} & \frac{288\kappa_2^\Sigma c_2^\Sigma + 20c_4^\Sigma - 216T_0\kappa_2^\Sigma \frac{\partial c_2^\Sigma}{\partial T} - 8T_0 \frac{\partial c_4^\Sigma}{\partial T}}{\frac{1}{24T_0^3} \frac{\partial^3 c_0^\Sigma}{\partial T^3}} \\ & + \frac{T_0^2 \left(\frac{\partial^2 c_4^\Sigma}{\partial T^2} + 12\kappa_2^\Sigma \left(6\frac{\partial^2 c_2^\Sigma}{\partial T^2} - T_0 \frac{\partial^3 c_2^\Sigma}{\partial T^3} + \kappa_2^\Sigma T_0^2 \frac{\partial^4 c_0^\Sigma}{\partial T^4} \right) \right)}{\frac{1}{24T_0^3} \frac{\partial^3 c_0^\Sigma}{\partial T^3}} \, . \end{aligned} \tag{4.12}$$

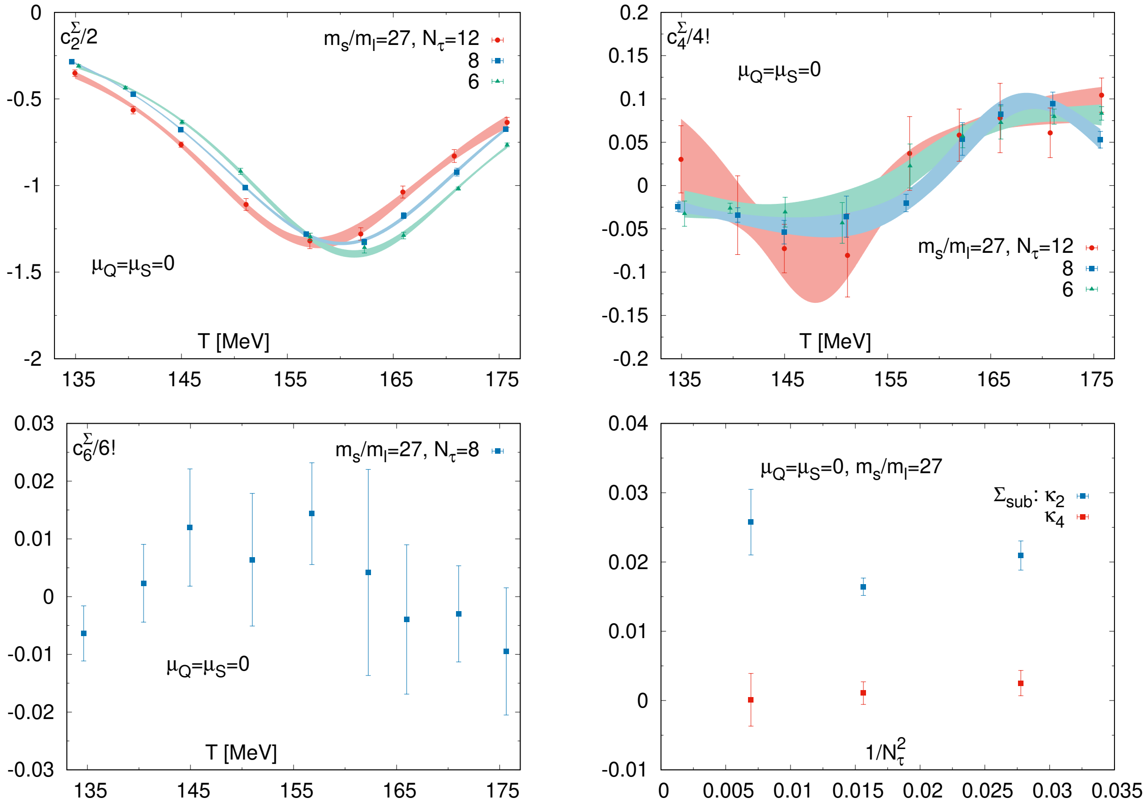

Figure 4.1: The 2nd (top left), 4th (top right) and 6th (bottom left) order expansion coefficients of the subtracted chiral condensate as a function of the temperature normalized with f_K and factorials. The data is shown for a system with vanishing μ_Q and μ_S at three lattice spacings with $N_\tau = 6, 8$ and 12. The colored bands represent the AIC weighted Padé fits of the coefficients. In the bottom right, we show the 2nd and 4th order curvature coefficients κ_2 and κ_4 of the chiral crossover line $T_c(\mu_B)$ as a function of $1/N_\tau^2$ extracted from the subtracted condensate.

N_τ		$\kappa_2(\Sigma_{\text{sub}})$	$\kappa_4(\Sigma_{\text{sub}})$	$\sigma(\kappa_4)$
6		0.0209(21)	0.00252	0.00182
8		0.0164(13)	0.00107	0.00164
12		0.0256(47)	0.000113	0.00380
∞	$\mathcal{O}(N_\tau^{-2})$	0.0150(35)	-0.000737	0.00344

Table 4.1: The curvature coefficients κ_2 and κ_4 of the chiral crossover line $T_c(\mu_B)$ extracted from the subtracted condensate Σ_{sub} for a system with vanishing μ_Q and μ_S at three lattice spacings with $N_\tau = 6, 8$ and 12. The error of κ_4 is denoted with $\sigma(\kappa_4)$. In the last column, we show a continuum extrapolation from a bootstrap with $\mathcal{O}(N_\tau^{-2})$ corrections.

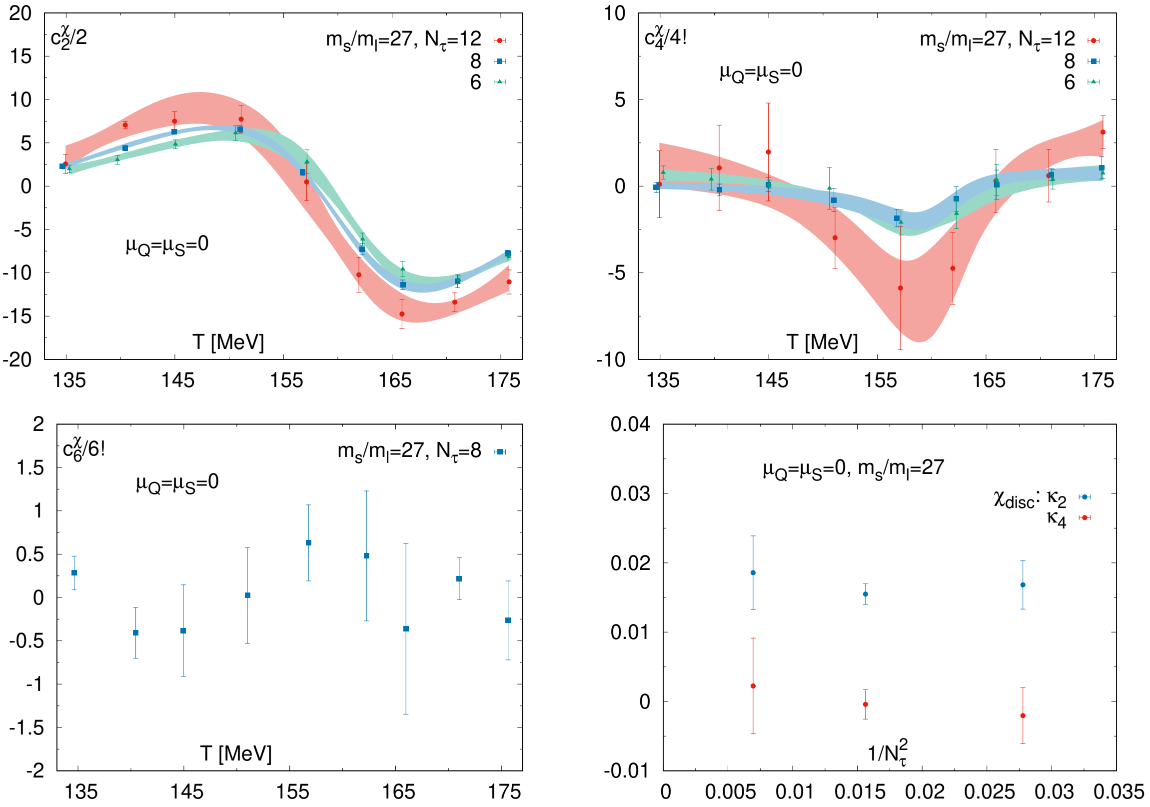

Figure 4.2: The 2nd (top left), 4th (top right) and 6th (bottom left) order expansion coefficients of the disconnected chiral susceptibility as a function of the temperature normalized with f_K and factorials. The data is shown for a system with vanishing μ_Q and μ_S at three lattice spacings with $N_\tau = 6, 8$ and 12. The colored bands represent the AIC weighted Padé fits of the coefficients. In the bottom right, we show the 2nd and 4th order curvature coefficients κ_2 and κ_4 of the chiral crossover line $T_c(\mu_B)$ as a function of $1/N_\tau^2$ extracted from the disconnected susceptibility.

N_τ		$\kappa_2(\chi_{\text{disc}})$	$\kappa_4(\chi_{\text{disc}})$	$\sigma(\kappa_4)$
6		0.0168(35)	-0.00205	0.00404
8		0.0155(15)	-0.000424	0.00213
12		0.0185(53)	0.00224	0.00690
∞	$\mathcal{O}(N_\tau^{-2})$	0.0158(47)	0.00238	0.00592

Table 4.2: The curvature coefficients κ_2 and κ_4 of the chiral crossover line $T_c(\mu_B)$ extracted from the disconnected susceptibility Σ_{sub} for a system with vanishing μ_Q and μ_S at three lattice spacings with $N_\tau = 6, 8$ and 12. The error of κ_4 is denoted with $\sigma(\kappa_4)$. In the last column, we show a continuum extrapolation from a bootstrap with $\mathcal{O}(N_\tau^{-2})$ corrections.

The 2nd and 4th order coefficients of the subtracted condensate and the disconnected susceptibility are shown in Fig. 4.1 and Fig. 4.2. Close to the crossover temperature T_0, the 2nd order of the condensate c_2^Σ has a pronounced minimum. Additionally, c_2^Σ is negative in the considered temperature range. When increasing N_τ, the shape of c_2^Σ and the value of the minimum do not change significantly. Only the location of the minimum shifts to smaller temperature values. Including the factorials from the Taylor series, we find that the 4th order c_4^Σ is significantly smaller compared to c_2^Σ. In the crossover region, c_4^Σ passes through zero and one may argue that the slope increases for larger N_τ values. However, the errors of c_4^Σ are significantly larger compared to the 2nd order coefficient and do not allow a proper distinction of different lattice spacings.

For the 2nd order of the susceptibility c_2^χ, we see a zero in the crossover region which shifts to smaller temperatures values for increasing N_τ. As for the condensate, the 4th order Taylor series coefficient is significantly smaller compared to the 2nd order. Although, c_4^χ has a minimum in the crossover region while c_2^χ has a zero, thus, the contribution of the 4th order might be larger or of similar magnitude close to the crossover line $T_c(\mu_B)$.

In Fig. 4.1 and Fig. 4.2, we show values for κ_2 obtained from the subtracted condensate Σ_{sub} and the disconnected susceptibility χ_{disc}. The continuum extrapolated values are shown in Tab. 4.2 and Tab. 4.1. The continuum results were generated using a bootstrap which takes into account $\mathcal{O}(N_\tau^{-2})$ corrections. As expected, κ_2 is positive for both observables and all N_τ, thus, for increasing and moderately large μ_B, the crossover temperature $T_c(\mu_B)$ shifts to smaller values. Within error bars, we do not see a difference between $\kappa_2(\Sigma_{\mathrm{sub}})$ and $\kappa_2(\chi_{\mathrm{disc}})$. Nevertheless, the mean of κ_2 from the disconnected susceptibility is slightly larger.

We show the values and continuum extrapolations of κ_4 in Fig. 4.2 and in Tab. 4.2. Using the error bars as a bound, we find that κ_4 is about a factor 5 smaller than the second order κ_2.

4.2 Strangeness neutral systems

In a strangeness neutral system, the curvature coefficients can be derived similarly as for the $\mu_Q = \mu_S = 0$ case in Sec. 4.1. The only difference is that in Eq. (4.5) the disconnected susceptibility has to be expanded in the chemical potentials μ_B, μ_Q and μ_S. By combining all coefficients for each order in μ_B, as shown in Eq. (2.68), the first contributing order κ_2 of the crossover line is similarly given by Eq. (4.9). The required expansion coefficients c_n^Σ and c_n^χ are smaller compared to the $\mu_Q = \mu_S = 0$ case and have smaller errors due to the electric charge and strangeness contributions. However, the general behavior of the coefficients is similar as described in Sec. 4.1. In Fig. 4.3 and Fig. 4.5, we show the constrained expansion coefficients up to 4th order for $N_\tau = 6, 8$ and 12. Additionally, we show the 6th order using our $N_\tau = 8$ ensemble. For the condensate, the 6th order c_6^Σ is significantly smaller compared to the 4th order. The 6th order coefficient of the susceptibility c_6^χ has large error bars but is at least a factor two smaller than c_4^χ in

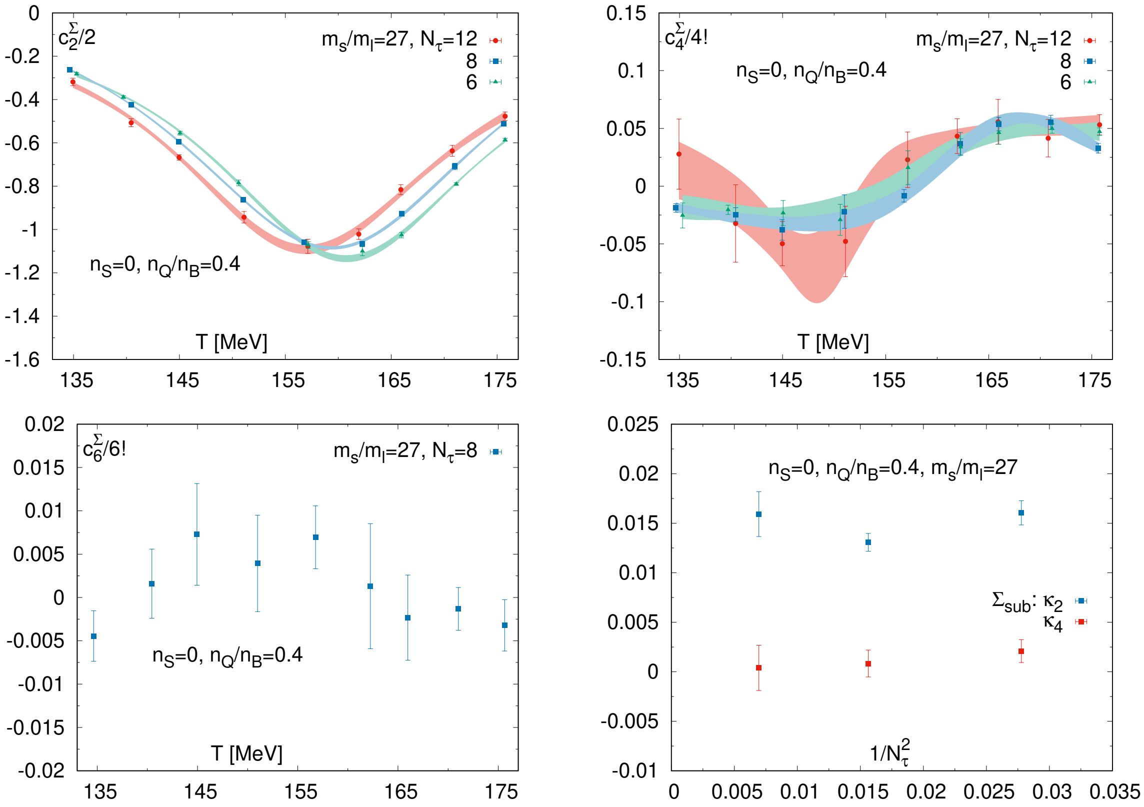

Figure 4.3: The 2nd (top left), 4th (top right) and 6th (bottom left) order expansion coefficients of the subtracted chiral condensate as a function of the temperature normalized with f_K and factorials. The data is shown for a strangeness neutral system at three lattice spacings with $N_\tau = 6, 8$ and 12. The colored bands represent the AIC weighted Padé fits of the coefficients. In the bottom right, we show the 2nd and 4th order curvature coefficients κ_2 and κ_4 of the chiral crossover line $T_c(\mu_B)$ as a function of $1/N_\tau^2$ extracted from the subtracted condensate.

N_τ		$\kappa_2(\Sigma_{\text{sub}})$	$\kappa_4(\Sigma_{\text{sub}})$	$\sigma(\kappa_4)$
6		0.0161(12)	0.00209	0.00116
8		0.0131(10)	0.000836	0.00136
12		0.0159(23)	0.000393	0.00229
∞	$\mathcal{O}(N_\tau^{-2})$	0.0120(20)	-0.000432	0.00235

Table 4.3: The curvature coefficients κ_2 and κ_4 of the chiral crossover line $T_c(\mu_B)$ extracted from the subtracted condensate Σ_{sub} for a strangeness neutral system at three lattice spacings with $N_\tau = 6, 8$ and 12. The error of κ_4 is denoted with $\sigma(\kappa_4)$. In the last column, we show a continuum extrapolation from a bootstrap with $\mathcal{O}(N_\tau^{-2})$ corrections.

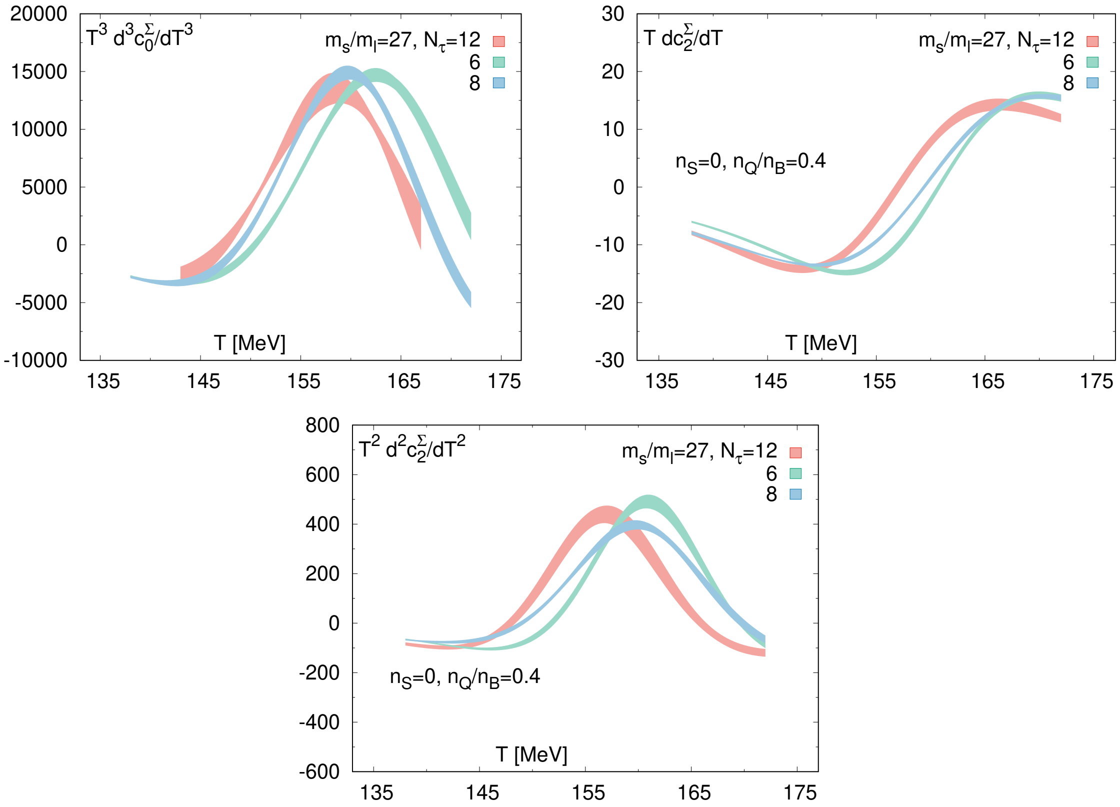

Figure 4.4: The third T derivative of the subtracted condensate (top left), the first T derivative (top right) and the second T derivative (bottom) of the 2nd order expansion coefficient as a function of the temperature as needed for the determination of κ_2. The colored bands stem from derivatives of the AIC weighted Padé sums.

the vicinity of the crossover temperature T_0. In Fig. 4.6, we illustrate the two main contribution to κ_2 extracted from the disconnected susceptibility. Here, the derivatives of the coefficients are determined from derivatives of the AIC weighted Padé sum. The contribution of the c_2^χ term to κ_2 in Eq. (4.9) is insignificant. Similarly, we show the main contributions to κ_2 determined from the subtracted condensate in Fig. 4.4. The obtained κ_2 values are sown in Fig. 4.3 and Tab. 4.3. We have performed a continuum extrapolation with $\mathcal{O}(N_\tau^{-2})$ corrections using three lattice spacings with $N_\tau = 6, 8$ and 12. In general, we do not see a difference between a strangeness neutral system and the $\mu_Q = \mu_S = 0$ case within error bars. However, the mean of κ_2 is about 10% smaller in the strangeness neutral case. Given the larger errors of the expansion coefficients required for κ_4, we were only able to determine a bound on the 4th order of the crossover line $T_c(\mu_B)$. In Tab. 4.3, we show values for κ_4 obtained from three lattice sizes with $N_\tau = 6, 8$ and 12. Due to the large errors for κ_4, no statement on the sign of κ_4 can be made. Nevertheless, the error of κ_4 is one order of magnitude smaller than κ_2, thus,

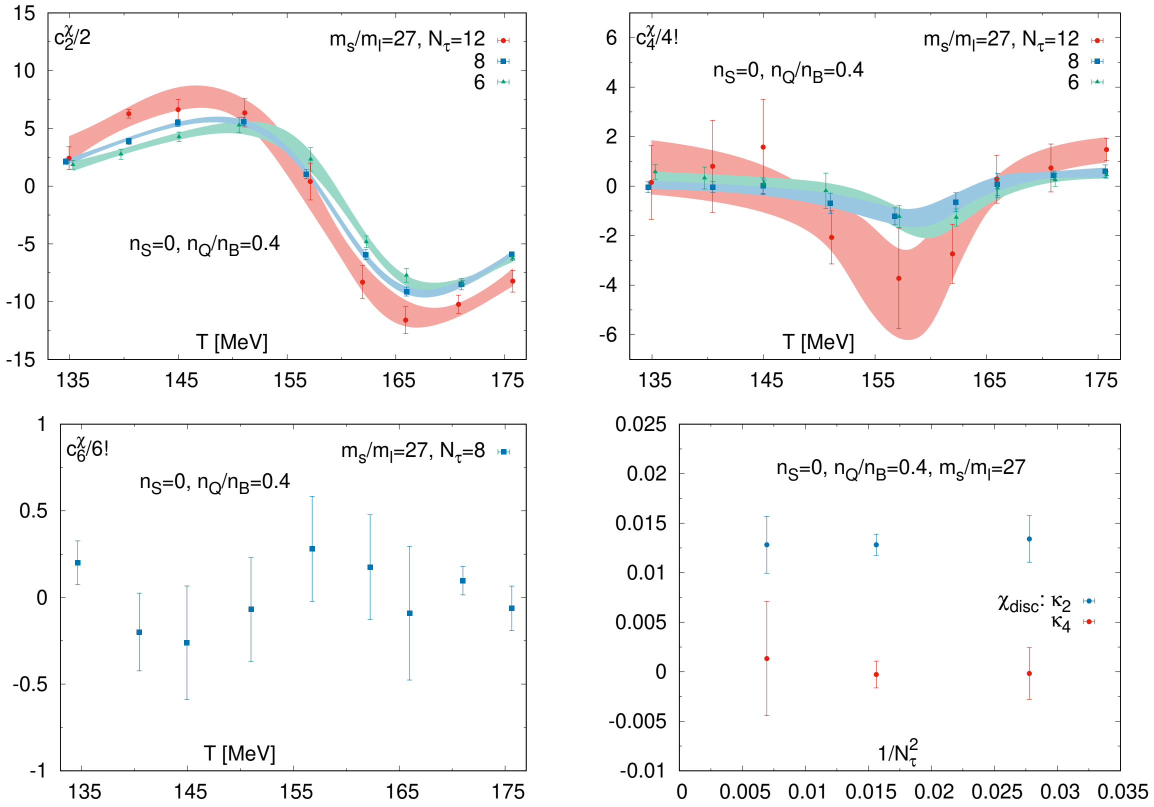

Figure 4.5: The 2nd (top left), 4th (top right) and 6th (bottom) order expansion coefficients of the disconnected chiral susceptibility as a function of the temperature normalized with f_K and factorials. The data is shown for a strangeness neutral system at three lattice spacings with $N_\tau = 6, 8$ and 12. The colored bands represent the AIC weighted Padé fits of the coefficients. In the bottom right, we show the 2nd and 4th order curvature coefficients κ_2 and κ_4 of the chiral crossover line $T_c(\mu_B)$ as a function of $1/N_\tau^2$ extracted from the disconnected susceptibility.

N_τ		$\kappa_2(\chi_{\rm disc})$	$\kappa_4(\chi_{\rm disc})$	$\sigma(\kappa_4)$
6		0.0134(26)	-0.000170	0.00260
8		0.0128(11)	-0.000277	0.00135
12		0.0128(29)	0.00134	0.00577
∞	$\mathcal{O}(N_\tau^{-2})$	0.0123(30)	0.000131	0.00406

Table 4.4: The curvature coefficients κ_2 and κ_4 of the chiral crossover line $T_c(\mu_B)$ extracted from the disconnected susceptibility $\chi_{\rm disc}$ for a strangeness neutral system at three lattice spacings with $N_\tau = 6, 8$ and 12. The error of κ_4 is denoted with $\sigma(\kappa_4)$. In the last column, we show a continuum extrapolation from a bootstrap with $\mathcal{O}(N_\tau^{-2})$ corrections.

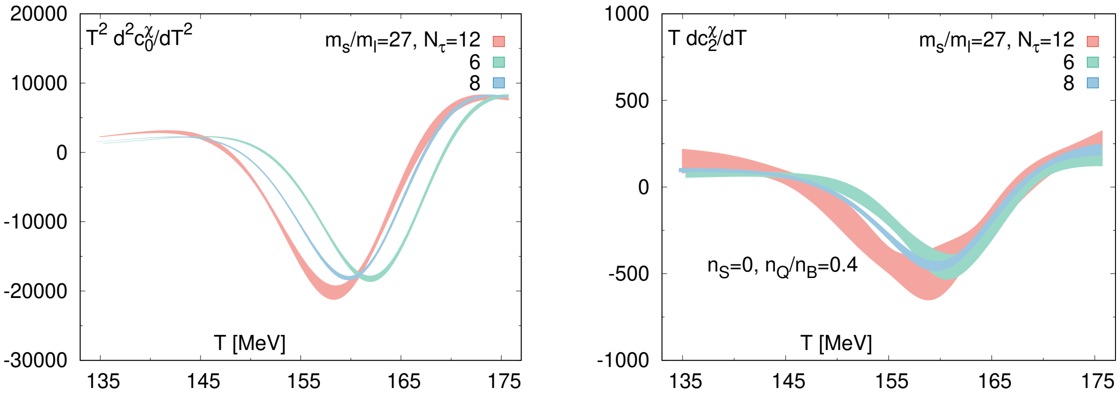

Figure 4.6: The second T derivative of the disconnected susceptibility (left) and the first T derivative of the 2nd order expansion coefficient (right) as a function of the temperature as needed for the determination of κ_2. The colored bands stem from derivatives of the AIC weighted Padé sums.

even for moderately large μ_B the contribution of κ_2 to $T_c(\mu_B)$ should be dominant. The dependency on the scale to fix the temperature is supposed to be small. When using the r_1 scale, the mean of $\kappa_2(\Sigma_{\text{sub}})$ increases only by 5% and is given by 0.0127(20).

At present, there is only one other publication [44] which calculated the curvature of the crossover line for a system which fulfills the initial conditions of heavy-ion collisions. In that publication, they extracted the leading order κ_2 from the renormalized condensate and the renormalized total light quark susceptibility. They used the stout action and performed simulations at imaginary baryon chemical potential in combination with an analytic continuation to real values. They report a κ_2 of 0.0158(13) from the total chiral susceptibility and 0.0138(11) from the chiral condensate. Since we determine κ_2 from the disconnected susceptibility, we can only compare to values for κ_2 from the condensate. Our value (0.0120(20)) does agree within errors although the reported mean in the publication is about 15% larger. They do not report values for κ_4.

The publication [43] performed similar simulations compared to the above mentioned reference. The only difference is that they do not have exact strangeness neutrality as required from the initial conditions of heavy-ion collisions. Instead, they performed simulations at vanishing strangeness chemical potential μ_S and gave arguments that the difference to exact strangeness neutrality is small. They used two determination methods for κ_2 and report (0.0132(10), 0.0131(12)) extracted from the renormalized light quark susceptibility and (0.0134(13), 0.0145(11)) from the subtracted condensate. These values are comparable to our results.

4.3 Comparison to chemical freeze-out curve

In heavy-ion collision experiments, measured particles stem from chemical freeze-out, thus, signs of criticality can only be found if the chemical freeze-out line is close to the crossover line as it is supposed to end in a critical point, if one exists. In the following, we compare the freeze-out line and crossover line with data from heavy-ion collision experiments and other lattice QCD simulations. For this, we first have to study up to which baryon chemical potential μ_B we can trust the Taylor expansions of the subtracted condensate and disconnected susceptibility. The difference between these truncated Taylor expansions up to $\mathcal{O}(\mu_B^2)$, $\mathcal{O}(\mu_B^4)$ and $\mathcal{O}(\mu_B^6)$ can be seen in Fig. 4.7 at fixed μ_B. Most important for this work is the difference around $T_c(\mu_B)$, i.e. along the crossover

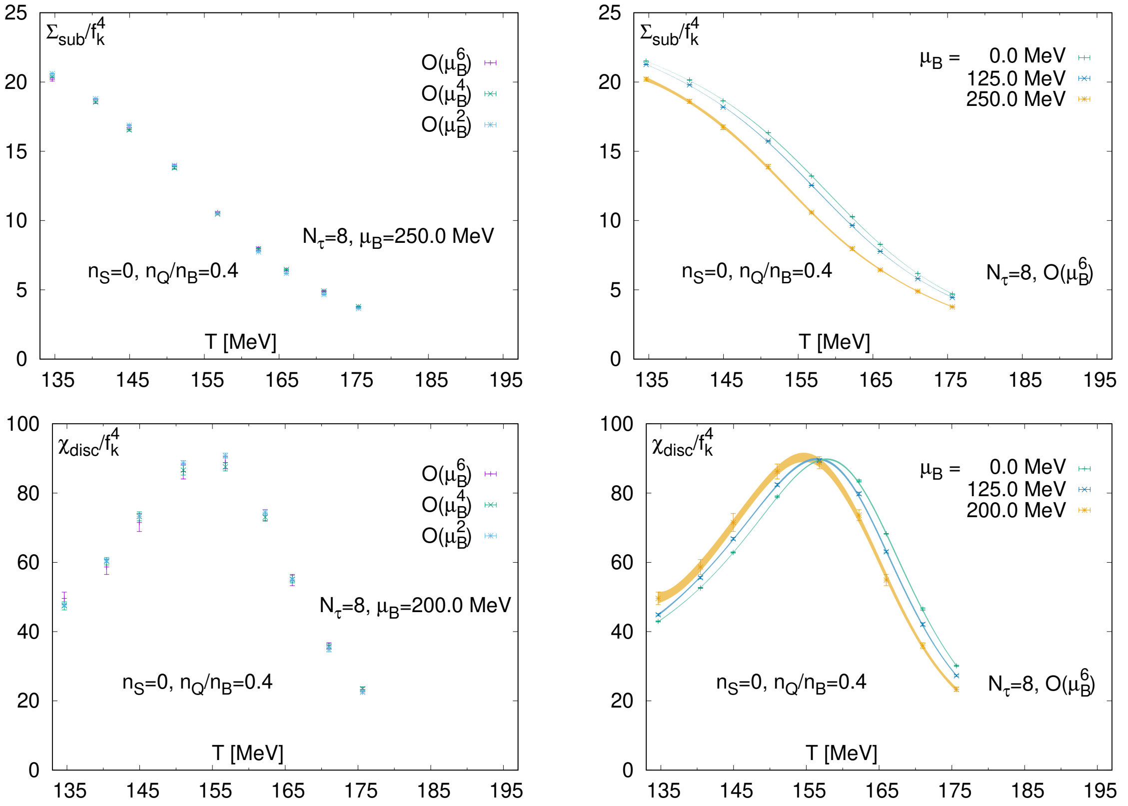

Figure 4.7: The Taylor expansion of the subtracted condensate (top) and the disconnected susceptibility (bottom) for one lattice spacing with $N_\tau = 8$ in a strangeness neutral system. The left figures show the Taylor expansion up to $\mathcal{O}(\mu_B^2)$, $\mathcal{O}(\mu_B^4)$ and $\mathcal{O}(\mu_B^6)$ at fixed μ_B and the right figures shows the expansion up to $\mathcal{O}(\mu_B^6)$ for several μ_B values. The colored bands correspond to different values for the baryon chemical potential μ_B and were constructed from the Padé AIC fits to the Taylor coefficients. The expansion coefficients are shown in Fig. 4.3 and Fig. 4.5.

line. For the condensate, almost no difference is visible even at $\mu_B = 250$ MeV between a 6th and 2nd order expansion. However, at low and high temperature the difference is larger. Only the 4th and 6th order expansions agree well within errors in the whole temperature range. This is expected as along $T_c(\mu_B)$ the 4th order is about 30 times smaller than the 2nd order. Likewise, the 4th order is about 5 times smaller than the 6th order. In general, these higher order corrections to the leading order of the subtracted condensate are small and never larger than 20%. This can be seen in the right of Fig. 4.7 which shows the Taylor expansion up to 6th order as a function of T for fixed μ_B ranging from 100 MeV to 250 MeV. We conclude that the Taylor expansion of the subtracted condensate can be trusted up to $\mu_B = 250$ MeV close to the crossover temperature, i.e. $\mu_B/T \simeq 1.65$. For a baryon chemical larger than 250 MeV the statistical errors become more pronounced and no statement about the truncation errors of the series can be made. Similar arguments can be made for the disconnected susceptibility. However, the disconnected susceptibility expansion can only be trusted up to $\mu_B = 200$ MeV given the relatively larger errors in the Taylor coefficients (see Fig. 4.7). In Fig. 4.8, we compare the parameterization of the $\mathcal{O}(\mu_B^2)$ and $\mathcal{O}(\mu_B^4)$ crossover line $T_c(\mu_B)$ extracted from the Taylor expansion of the subtracted condensate. As discussed above, the Taylor

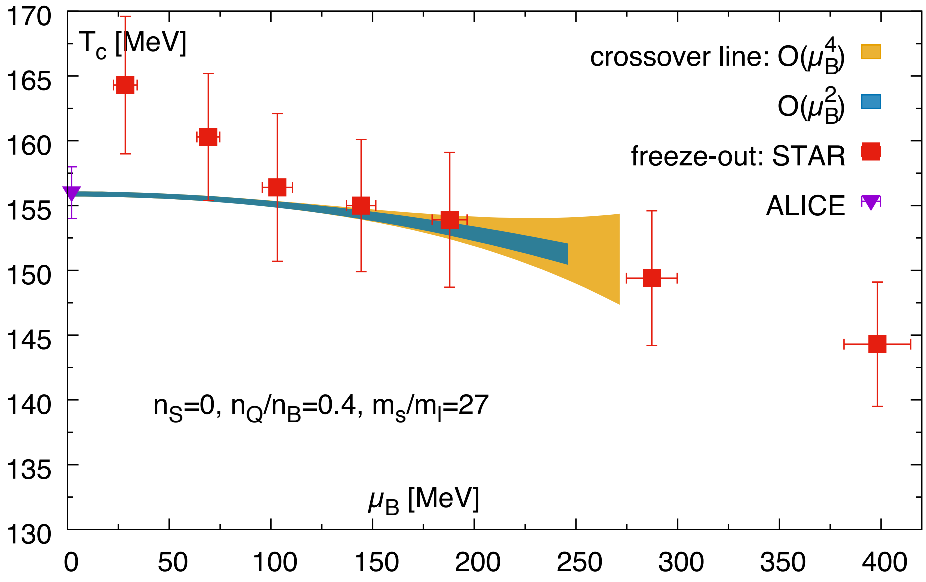

Figure 4.8: The crossover temperature T_c as a function of the baryon chemical potential μ_B for a strangeness neutral system. All required expansion coefficients κ_n have been extracted from the subtracted condensate Σ_{sub}. The 2nd and 4th order crossover line are continuum extrapolated using three lattice spacings with $N_\tau = 6, 8$ and 12. Also shown are freeze-out parameters from the experiments ALICE [45] and STAR [46].

expansion including 4th order corrections can be trusted up to $\mu_B \leq 250$ MeV. We argue that for $\mu_B \leq 250$ MeV fourth order corrections are insignificant. For μ_B values above 250 MeV, the uncertainty of κ_4 becomes a more dominant contribution to the curvature of the crossover line as the spread of the error band increases from about 0.5 MeV to almost 4.0 MeV at $\mu_B = 250$ MeV. We also compare the crossover line with results on freeze-out temperatures extracted from particle yields measured in heavy-ion collision experiments such as ALICE [45] (LHC) and STAR [46] (RHIC). The mean of the ALICE freeze-out temperature of 156(2) MeV agrees very well with our crossover line at almost vanishing baryon chemical potential. The STAR data seems to extrapolate to a freeze-out temperature of about 167 MeV which is significantly higher than the ALICE data point. Also, the curvature of the STAR data at small μ_B would require to have a κ_2 which is at least a factor 6 larger than our value. Given this rather large κ_2, the 4th order κ_4 would need to be negative and at least 30 times larger than our value. When leaving out the first two STAR data points the curvature agrees well with the crossover line from the subtracted condensate. At present, no statement can be made whether the chemical freeze-out line is close to the QCD crossover by just comparing with ALICE and STAR data. However, several arguments [47, 48] have been made that chemical freeze-out might be related to lines of constant physics (LCPs), i.e. lines $T_X(\mu_B)$ where an observable X stays constant. This is why we compare in the following the crossover line to LCPs from lattice QCD simulations [35]. In that publication, LCPs are parameterized similarly to the crossover line. For LCPs starting at $T = 155.9$ MeV, they report second order curvature coefficients κ_2^X for constant energy density ϵ

$$0.00932 \leq \kappa_2^{\epsilon} \leq 0.0114 , \tag{4.13}$$

for constant entropy density s

$$0.00818 \leq \kappa_2^{s} \leq 0.0100 \tag{4.14}$$

and for constant pressure P

$$0.00767 \leq \kappa_2^{P} \leq 0.00971 . \tag{4.15}$$

The LCP curvatures from energy density and entropy density agree to the crossover curvature although the overlap to $\kappa_2^{\Sigma} = 0.00120(20)$ within error bars is only at the border of 1σ. This might suggest that physics do not change much along the crossover line (see Sec. 5). In particular, the energy density seems to stay constant as there is good agreement to κ_2^{Σ}. They also report 4th order curvature coefficients κ_4^X. Given our rather large errors in κ_4 from the crossover live, the agreement to 4th order curvature coefficients from LCPs is expected.

4.4 The crossover surface

The methods described in this work allow to perform Taylor expansions in any combination of μ_B, μ_Q and μ_S as well as the quark chemical potentials μ_u, μ_d and μ_s by simply evaluating gauge configurations generated at zero chemical potential. This freedom enables to study the curvature of the QCD crossover line for different systems using the method outlined in Sec. 4. In theory, combining curvatures from several combinations of μ_B, μ_Q and μ_S would allow to map out a 4-dimensional crossover surface in a QCD phase diagram, i.e. the plane (T, μ_B, μ_Q, μ_S).

	$\kappa_2(\chi_{\text{disc}})$
$\mu_B = \mu_S = 0$	0.0314(39)
$\mu_Q = \mu_S = 0$	0.0158(47)
$\mu_B = \mu_Q = 0$	0.0146(35)
$n_S = 0$, $n_Q/n_B = 0.5$	0.0127(30)
$n_S = 0$, $n_Q/n_B = 0.4$	0.0123(30)
$n_S = 0$, $n_Q/n_B = 0.1$	0.0117(26)

Table 4.5: The continuum extrapolations of the 2nd order curvature coefficient κ_2 extracted from Taylor expansions of the disconnected two-flavor susceptibility using different constrains which are shown in the first column.

The only remaining cases, i.e. Taylor expansions in a single chemical potential, which were not covered yet in previous sections are expansions in μ_Q, and in μ_S. In these cases, the expansion coefficients from Sec. 2.2 simplify for the subtracted chiral condensate Σ_{sub} to

$$c_n^{\Sigma} = \Omega_{0n0}^{BQS} \qquad \text{for} \qquad \mu_B = \mu_S = 0 \ , \tag{4.16}$$

$$c_n^{\Sigma} = \Omega_{00n}^{BQS} \qquad \text{for} \qquad \mu_B = \mu_Q = 0 \ , \tag{4.17}$$

and for the disconnected chiral susceptibility χ_{disc} to

$$c_n^{\chi} = \Xi_{0n0}^{BQS} \qquad \text{for} \qquad \mu_B = \mu_S = 0 \ , \tag{4.18}$$

$$c_n^{\chi} = \Xi_{00n}^{BQS} \qquad \text{for} \qquad \mu_B = \mu_Q = 0 \ . \tag{4.19}$$

As shown in the last sections, the curvatures extracted from the condensate and disconnected susceptibility give similar results. This is why in the following we only focus on the disconnected susceptibility. In Fig. 4.9, we compare the curvature κ_2 from the Taylor expansions in μ_B, in μ_Q and in μ_S for finite temporal extent with $N_\tau = 6, 8$ and 12. The continuum extrapolated values are summarized in Tab. 4.5. We found that the $\mu_B = \mu_S = 0$ case has a curvature of 0.314(39) which is about two times larger than all other cases ranging from 0.0146(35) ($\mu_B = \mu_Q = 0$) to 0.0158(47) ($\mu_Q = \mu_S = 0$). This large curvature can be explained phenomenological as pions are light compared

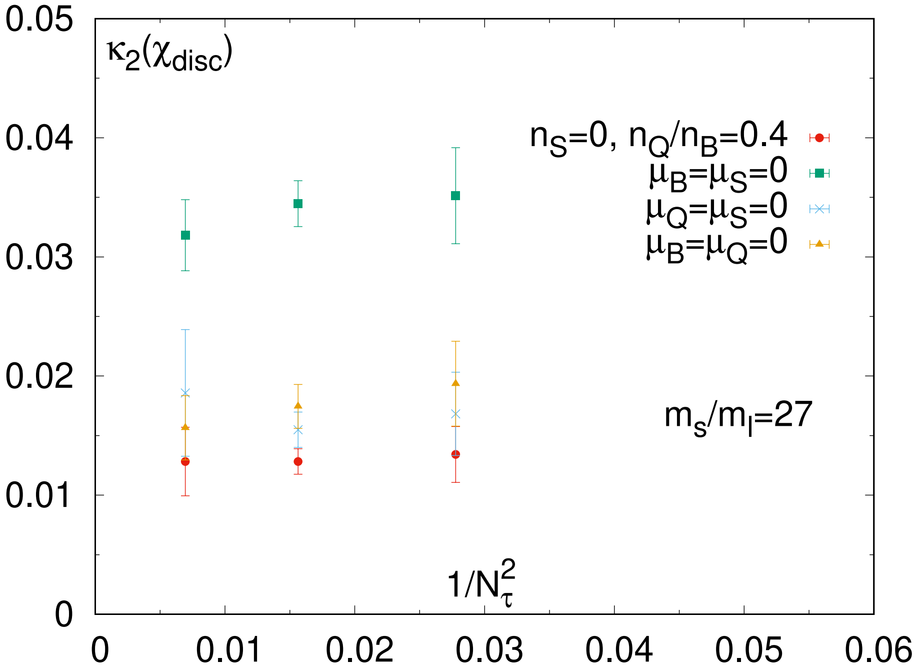

Figure 4.9: The 2nd order curvature coefficient κ_2 as a function of $1/N_\tau^2$ extracted from Taylor expansions of the disconnected two-flavor susceptibility using different constrains.

to baryons and kaons. Therefore, when increasing μ_Q, with $\mu_B = \mu_S = 0$ fixed, pions are added to the system more easily which leads to a larger temperature reduction compared to just increasing μ_B or μ_S. This argument assumes that the energy density stays constant along the crossover line. As shown above, this seems to be correct for heavy-ion collisions. To fully support this argument, we would need to identify lines of constant energy density for e.g. the $\mu_B = \mu_S = 0$ case and compare these to the corresponding crossover line. In theory, it is also expected that the case $\mu_Q = \mu_S = 0$ has a larger curvature than the $\mu_B = \mu_Q = 0$ case. However, within errors we observe no difference between both curvatures. The origin of this increased curvature stems from the slope of the 2nd order expansion coefficient of the disconnected susceptibility. It is the main contribution to κ_2 (see Eq. 4.9) as it is multiplied with T_0. Note that the denominator is independent of the constrains, thus, is in all cases equivalent. In Fig. 4.10, we compare c_2^χ and its slope for $\mu_B = \mu_S = 0$ to the strangeness neutral case. The slope for $\mu_B = \mu_S = 0$ is about a factor 3 larger than the strangeness neutral case.

We have also studied the curvature κ_2 in systems with constrains of the form

$$n_S = 0, \quad \frac{n_Q}{n_B} = r \tag{4.20}$$

at three r values. We chose $r = 0.5$ the isopin symmetric case, $r = 0.4$ the initial

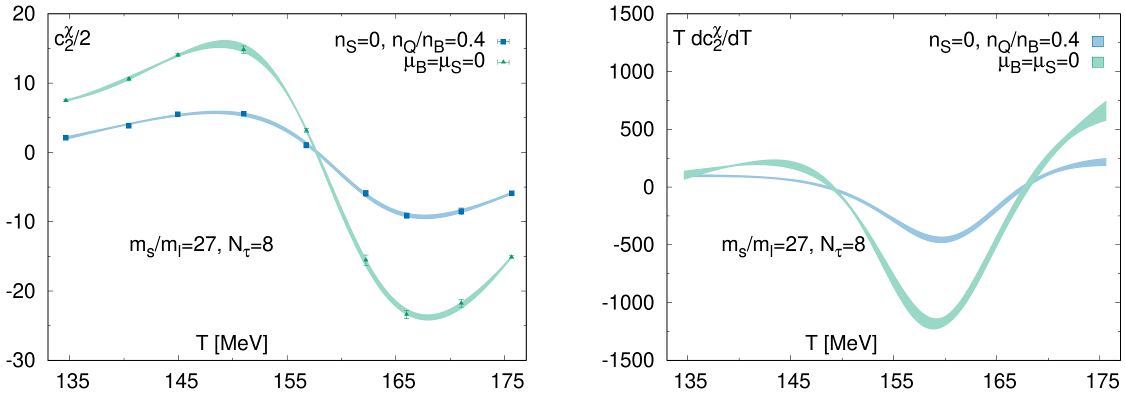

Figure 4.10: The 2nd order expansion coefficient of the disconnected susceptibility (left) and the first T derivative (right) at a finite lattice spacing with $N_\tau = 8$ shown for a system with $\mu_B = \mu_S = 0$ as well as for a strangeness neutral system.

conditions in Au-Au and Pb-Pb collisions (see Sec.4), and $r = 0.1$ which is a value close to the charge neutral case. In Tab. 4.5, we show the continuum results for the mentioned cases using three lattice spacings with $N_\tau = 6, 8$ and 12. We observe when decreasing r from 0.5 to 0.1 the mean of κ_2 changes by about 8% to smaller values. However, within errors all cases can be considered equal.

At present, there are no publications which report the curvature for the cases investigated in this section except the $r = 0.4$ case and the $\mu_Q = \mu_S = 0$ case which we already discussed in Sec. 4.1 and Sec. 4.2.

5 Fluctuations along the QCD crossover line

In this section, we are going to study the behavior of observables along the QCD crossover line. We have already shown in Sec. 4 that the pressure stays constant along the crossover line. However, other observables might have more interesting behavior as their properties are strongly related to the correlation length of the system when approaching a theoretical critical point, thus, might show signs of increased fluctuations with increasing baryon-density. In particular of interest are the disconnected susceptibility and net baryon-number fluctuations as both are supposed to diverge at a critical point in an infinite volume [32, 11, 12]. Additionally, we investigate the change of the chiral condensate along the crossover line as its change is an important input parameter for models to calculate e.g. the nucleon mass [49].

5.1 Chiral observables

In the following, we derive equations for the relative change of the disconnected two-flavor susceptibility along the crossover line $T_c(\mu_B)$. In general, these steps are equivalent for other observables as long as they are normalized with a T independent variable. In our case, we use the kaon decay constant f_K. Similarly as for the crossover line, we compute curvature coefficients λ_2 and λ_4 defined by

$$\frac{\chi_{\mathrm{disc}}(T_c(\mu_B),\mu_B)-\chi_{\mathrm{disc}}(T_0,0)}{\chi_{\mathrm{disc}}(T_0,0)}=\lambda_2\left(\frac{\mu_B}{T_0}\right)^2+\lambda_4\left(\frac{\mu_B}{T_0}\right)^4+\ \cdots\ . \tag{5.1}$$

In order to determine the coefficients λ_2 and λ_4, we start from a joint Taylor expansion in $\hat{\mu}$ and T around $(T_0,\hat{\mu}=0)$. It is given by

$$\begin{aligned}\frac{\chi_{\mathrm{disc}}(T,\mu_B)}{f_K^4} &= c_0^{\chi}\big|_{(T_0,0)}+\left.\frac{\partial c_0^{\chi}}{\partial T}\right|_{(T_0,0)}(T-T_0)+\frac{1}{2}\left.\frac{\partial^2 c_0^{\chi}}{\partial T^2}\right|_{(T_0,0)}(T-T_0)^2 \\ &\quad+\frac{1}{2}\,c_2^{\chi}\big|_{(T_0,0)}\,\hat{\mu}_B^2+\frac{1}{24}\,c_4^{\chi}\big|_{(T_0,0)}\,\hat{\mu}_B^4+\frac{1}{2}\left.\frac{\partial c_2^{\chi}}{\partial T}\right|_{(T_0,0)}(T-T_0)\hat{\mu}_B^2+\cdots\ .\end{aligned} \tag{5.2}$$

Here, we have used the Taylor coefficients c_n^{χ} as introduced in Sec. 2.2 and neglected higher orders in T and $\hat{\mu}_B$ which do not contribute to $\mathcal{O}(\mu_B^2)$ and $\mathcal{O}(\mu_B^4)$. This expansion has to be evaluated along the crossover line, i.e. the temperature difference $T-T_0$ and powers of $1/T$ are given by

$$T-T_0\equiv T_c(\mu_B)-T_0=-\kappa_2\frac{\mu_B^2}{T_0}-\kappa_4\frac{\mu_B^4}{T_0^3}+\mathcal{O}(\mu_B^6) \tag{5.3}$$

and

$$\frac{1}{T^n}=\frac{1}{T_0^n}\left(1+n\kappa_2\left(\frac{\mu_B}{T_0}\right)^2+\mathcal{O}(\mu_B^4)\right)\ . \tag{5.4}$$

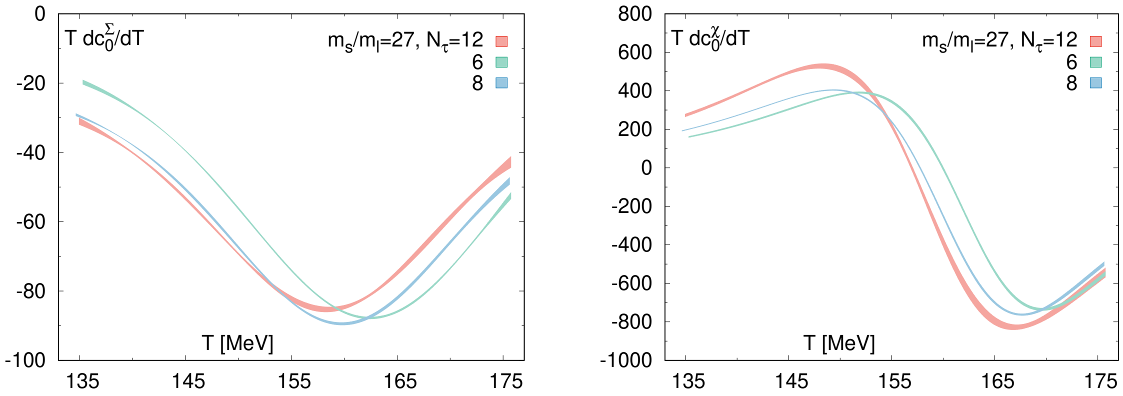

Figure 5.1: The first T derivative of the subtracted condensate (left) and the first T derivative of the disconnected two-flavor susceptibility (right) as needed for the determination of λ_2. The colored bands stem from derivatives of the AIC weighted Padé sums.

We can now reorder the joint Taylor expansion in powers of μ_B/T_0 to

$$\begin{aligned}\frac{\chi_{\mathrm{disc}}(T,\mu_B)}{f_K^4} &= c_0^\chi|_{(T_0,0)} + \left(-T_0\, \frac{\partial c_0^\chi}{\partial T}\bigg|_{(T_0,0)} \kappa_2 + \frac{1}{2}\, c_2^\chi|_{(T_0,0)}\right)\left(\frac{\mu_B}{T_0}\right)^2 \\ &+ \left(-T_0\, \frac{\partial c_0^\chi}{\partial T}\bigg|_{(T_0,0)} \kappa_4 + \frac{1}{2} T_0^2\, \frac{\partial^2 c_0^\chi}{\partial T^2}\bigg|_{(T_0,0)} \kappa_2^2 + c_2^\chi|_{(T_0,0)}\, \kappa_2 \right. \\ &\left. + \frac{1}{24}\, c_4^\chi|_{(T_0,0)} - \frac{1}{2} T_0\, \frac{\partial c_2^\chi}{\partial T}\bigg|_{(T_0,0)} \kappa_2\right)\left(\frac{\mu_B}{T_0}\right)^4 + \cdots \,.\end{aligned} \tag{5.5}$$

The last step is to normalize each order with c_0^χ. We find for the coefficients λ_n along the crossover line

$$\lambda_2 = \frac{-\frac{\partial c_0^\chi}{\partial T}\kappa_2 T_0 + \frac{1}{2}c_2^\chi}{c_0^\chi} \tag{5.6}$$

and

$$\lambda_4 = \frac{-\frac{\partial c_0^\chi}{\partial T}\kappa_4 T_0 + \frac{1}{2}\frac{\partial^2 c_0^\chi}{\partial T^2}\kappa_2^2 T_0^2 + c_2^\chi \kappa_2 + \frac{1}{24}c_4^\chi - \frac{1}{2}\frac{\partial c_2^\chi}{\partial T}\kappa_2 T_0}{c_0^\chi} \,. \tag{5.7}$$

Here, all Taylor coefficients have to be evaluated at $(T_0, 0)$. Note that in this last step all coefficients λ_n become independent of the normalization choice as all terms in the numerator and denominator contain a factor $1/f_K^4$. In our simulations, we extract the crossover parameters T_0 and κ_n from the observable of interest, i.e. in Eq. (5.6) and

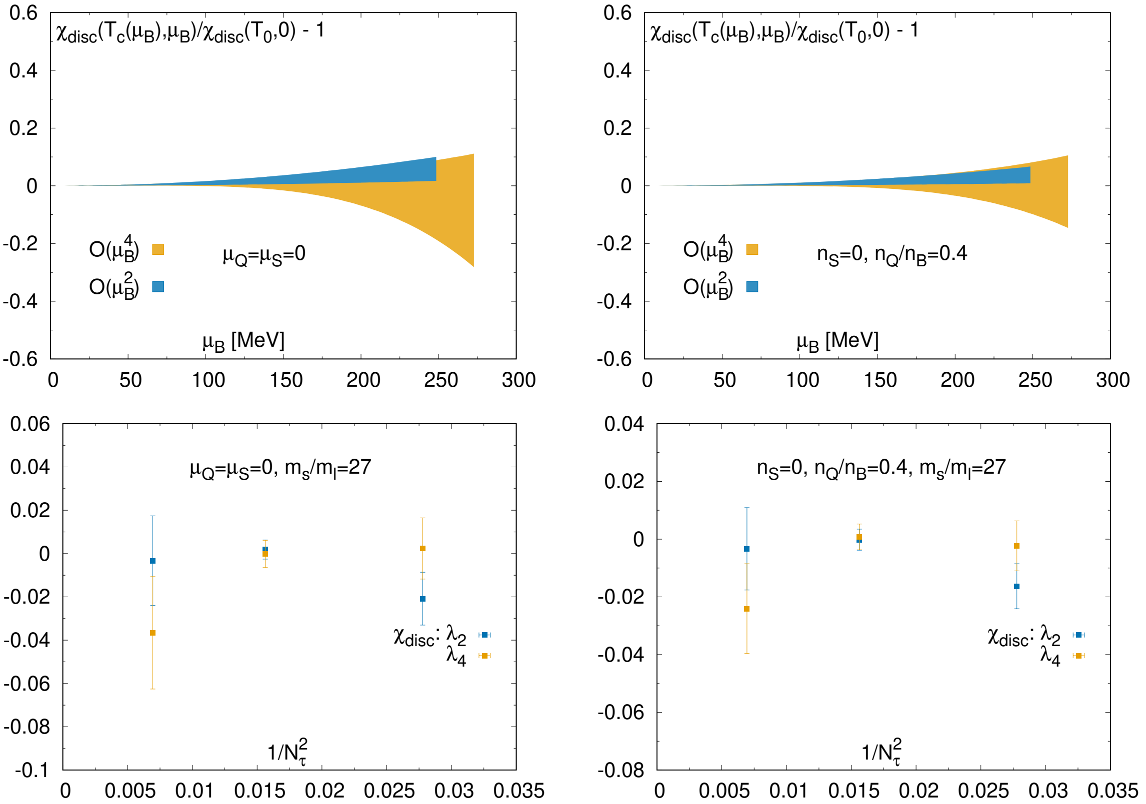

Figure 5.2: The relative change of the disconnected susceptibility (top) along the corresponding crossover line $T_c(\mu_B)$ for systems with $\mu_Q = \mu_S = 0$ and strangeness neutrality. The blue band includes continuum extrapolated corrections up to 2nd order in μ_B and the yellow band up to 4th order in μ_B. The values for λ_2 and λ_4 at finite N_τ are shown in the bottom.

N_τ		$\lambda_2(\chi_{\text{disc}})$	$\sigma(\lambda_2)$	$\lambda_4(\chi_{\text{disc}})$	$\sigma(\lambda_4)$
6		-0.0163	0.00779	-0.00234	0.00866
8		-0.000180	0.00366	0.000765	0.00446
12		-0.00336	0.0143	-0.0241	0.0155
∞	$n_S = 0, n_Q/n_B = 0.4$	0.0148	0.0113	-0.00697	0.0128
6		-0.0208	0.0122	0.00236	0.0141
8		0.00186	0.00441	-0.000217	0.00624
12		-0.00327	0.0207	-0.0366	0.0260
∞	$\mu_Q = \mu_S = 0$	0.0230	0.0163	-0.0165	0.0201

Table 5.1: The coefficients λ_2 and λ_4 extracted from the disconnected susceptibility χ_{disc} for systems with $\mu_Q = \mu_S = 0$ and strangeness neutrality at three lattice spacings with $N_\tau = 6, 8$ and 12. The continuum extrapolated values stem from a bootstrap using an ansatz with $\mathcal{O}(N_\tau^{-2})$ corrections. Here, σ denotes the standard error.

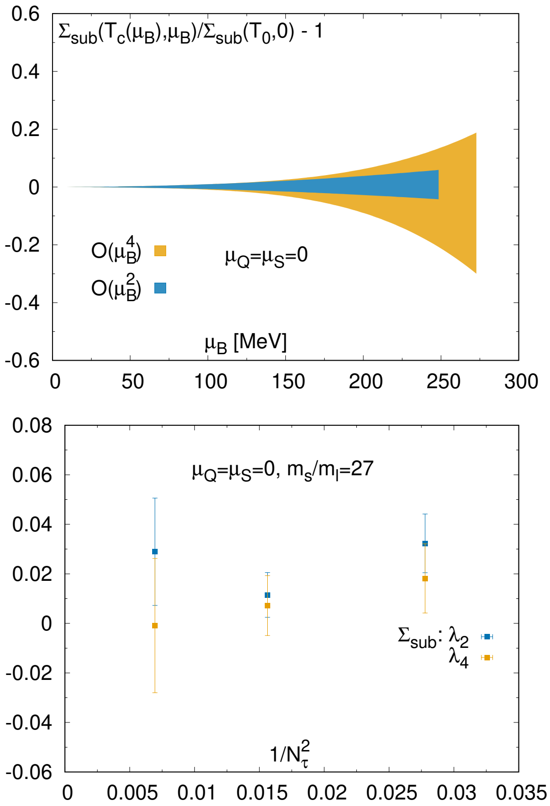

Figure 5.3: The relative change of the subtracted condensate (top) along the corresponding crossover line $T_c(\mu_B)$ for systems with $\mu_Q = \mu_S = 0$ and strangeness neutrality. The blue band includes continuum extrapolated corrections up to 2nd order in μ_B and the yellow band up to 4th order in μ_B. The values for λ_2 and λ_4 at finite N_τ are shown in the bottom.

N_τ		$\lambda_2(\Sigma_{\text{sub}})$	$\sigma(\lambda_2)$	$\lambda_4(\Sigma_{\text{sub}})$	$\sigma(\lambda_4)$
6		0.0237	0.00945	0.0140	0.00885
8		0.00674	0.00668	0.00511	0.0101
12		0.0220	0.0162	0.00118	0.0163
∞	$n_S = 0, n_Q/n_B = 0.4$	0.000902	0.0152	-0.00440	0.0171
6		0.0323	0.0119	0.0182	0.0140
8		0.0115	0.00904	0.00718	0.0121
12		0.0289	0.0217	-0.000892	0.0271
∞	$\mu_Q = \mu_S = 0$	0.00329	0.0199	-0.00703	0.0252

Table 5.2: The coefficients λ_2 and λ_4 extracted from the subtracted condensate Σ_{sub} for systems with $\mu_Q = \mu_S = 0$ and strangeness neutrality at three lattice spacings with $N_\tau = 6, 8$ and 12. The continuum extrapolated values stem from a bootstrap using an ansatz with $\mathcal{O}(N_\tau^{-2})$ corrections. Here, σ denotes the standard error.

Eq. (5.7) the values were extracted from the disconnected susceptibility χ_{disc}. Therefore, it is expected that the second order λ_2 is small because the contribution of $\frac{\partial c_0^\chi}{\partial T}$ to λ_2 is exactly zero at T_0, as it is the definition of the crossover temperature (see Fig. 5.1). Likewise, the last term c_2^χ is small as it passes through zero in the crossover region (see Fig. 4.5). This is why in particular the 4th order λ_4 is important for the disconnected susceptibility. However, the difference in λ_2 and λ_4 is small when using the chiral condensate to determine the crossover curvature κ_n and the crossover temperature T_0.

In Fig. 5.2, we show the relative change of the disconnected two-flavor susceptibility for systems with strangeness neutrality and $\mu_Q = \mu_S = 0$ up to $\mathcal{O}(\mu_B^2)$ and $\mathcal{O}(\mu_B^4)$. The coefficients λ_n are shown up to 4th order in Tab. 5.1 for finite N_τ and in the continuum. In both cases, the change is small and never larger than 15% for $\mu_B < 250$ MeV. For the strangeness neutral case, the change is always smaller than 10%. We argue that this insignificant change in an observable which should diverge at a critical point is a strong sign to disfavor a critical point in the region defined by our crossover line for baryon chemical potentials up to 250 MeV. To truly exclude a critical point in this region, we would have to study the change of the parameters λ_n with increasing lattice volumes. In this work, all simulations were performed at a fixed lattice volume which sets a bound on the maximal correlation length. However, it has been shown by [50] that volume effects are small for an aspect ratio of 4, i.e. lattices with $N_\sigma/N_\tau = 4$.

For the subtracted condensate, it is not expected that the leading order λ_2 is small given that the contributing terms, $\frac{\partial c_0^\Sigma}{\partial T}$ and c_2^Σ, are finite and not close to zero in the transition region (see Fig. 5.1 and Fig. 4.3). However, we found that λ_2 and λ_4 are small. Consequently, the subtracted condensate stays constant along the crossover line. This can be seen in Fig. 5.3 for systems with strangeness neutrality and $\mu_Q = \mu_S = 0$ up to $\mathcal{O}(\mu_B^2)$ and $\mathcal{O}(\mu_B^4)$. The relative change of Σ_{sub} along the crossover line has almost no slope, only the error band widens with increasing μ_B. For both systems, the relative change of Σ_{sub} along the crossover line stays below 3% for a baryon chemical potential smaller than 200 MeV. For larger μ_B, the errors become more dominant but still limit the deviations to zero chemical potential to be relatively small.

5.2 Conserved charges

In Sec. 2, we have introduced generalized susceptibilities χ_{ijk}^{BQS} as the Taylor coefficients of the normalized QCD pressure P/T^4. They can be directly related to observables measured in heavy-ion collision experiments [51]. In particular, these Taylor coefficients are proportional to higher order moments: mean M_X, variance σ_X^2, skewness S_X and kurtosis k_X which are obtained by net charge fluctuations $\delta N_X = N_X - \langle N_X \rangle$ for each charge X in the BQS ensemble. Their relations to generalized susceptibilities are shown in Tab. 5.3. Unfortunately, in heavy-ion collisions the volume is unknown. However, ratios of higher order moments can be constructed in a volume independent way allowing a direct comparison to lattice simulations [52, 53, 54]. In the following, we study

Moment	Symbol	Experiment	Lattice
mean	M_X	$\langle N_X \rangle$	$VT^3\chi_1^X$
variance	σ_X^2	$\left\langle (\delta N_X)^2 \right\rangle$	$VT^3\chi_2^X$
skewness	S_X	$\dfrac{\left\langle (\delta N_X)^3 \right\rangle}{\sigma_X^3}$	$\dfrac{VT^3\chi_3^X}{\left(VT^3\chi_2^X\right)^{3/2}}$
kurtosis	k_X	$\dfrac{\left\langle (\delta N_X)^4 \right\rangle}{\sigma_X^4} - 3$	$\dfrac{VT^3\chi_4^X}{\left(VT^3\chi_2^X\right)^2}$

Table 5.3: Higher order moments as measured in heavy-ion experiments and their associated lattice observables obtained from higher order susceptibilities. Here, X corresponds to the conserved charges: baryon number B, electric charge Q and strangeness S.

fluctuations of net baryon-number along the QCD crossover line, i.e. the change of σ_B^2. To stick with our notation, we chose to normalize σ_B^2 with $V f_k^3$. As already discussed in in Sec. 5.1, normalizing an observable with a constant term does not have an influence on the coefficients λ_n. These coefficients can be calculated as for the chiral condensate and chiral disconnected susceptibility (see Eq. (5.6) and Eq. (5.7)). Accordingly, the second order is obtained by

$$\lambda_2 = \frac{-\frac{\partial c_0^B}{\partial T}\kappa_2 T_0 + \frac{1}{2}c_2^B}{c_0^B} \ . \tag{5.8}$$

Here, we use the crossover parameters κ_n and T_0 extracted from the subtracted chiral condensate. The Taylor expansion of $\sigma_B^2/(V f_K^3)$ can be written as

$$\frac{\sigma_B^2}{V f_K^3} = \frac{1}{V f_K^3}\frac{\partial \ln Z}{\partial \hat{\mu}_B^2} = \sum_{i,j,k=0}^{\infty} \frac{\xi_{ijk}^{BQS}}{i!j!k!}\hat{\mu}_B^i \hat{\mu}_Q^j \hat{\mu}_S^k \tag{5.9}$$

with

$$\xi_{ijk}^{BQS} = \frac{1}{V f_K^3} \left. \frac{\partial \ln Z}{\partial \hat{\mu}_B^{i+2} \partial \hat{\mu}_Q^j \partial \hat{\mu}_S^k} \right|_{\mu=0} \ . \tag{5.10}$$

For a constrained Taylor expansion, we introduce the following notation

$$\frac{\sigma_B^2}{V f_K^3} = \frac{1}{V f_K^3}\frac{\partial \ln Z}{\partial \hat{\mu}_B^2} = \sum_{n=0}^{\infty} \frac{c_n^B}{n!}\hat{\mu}_B^n \tag{5.11}$$

where the coefficients c_n^B have the same structure as derived for chiral observables in Sec. 2.2. In a system with vanishing μ_Q and μ_S, these coefficients simplify to

$$c_n^B = \xi_{n00}^{BQS} \ . \tag{5.12}$$

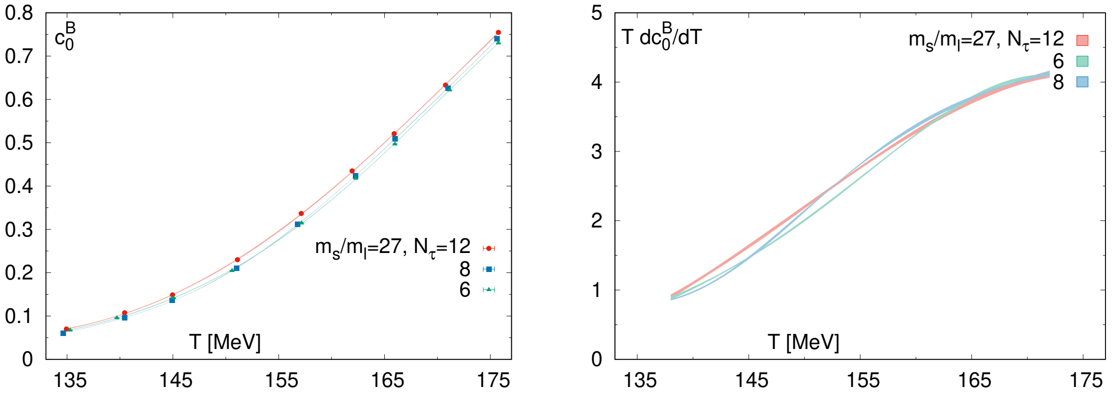

Figure 5.4: The net baryon-density fluctuations normalized with f_K^3 (left) and the corresponding first T derivative (right). The colored bands stem from the AIC weighted Padé sums and their derivatives. The data is shown for three finite lattice spacings with $N_\tau = 6, 8$ and 12.

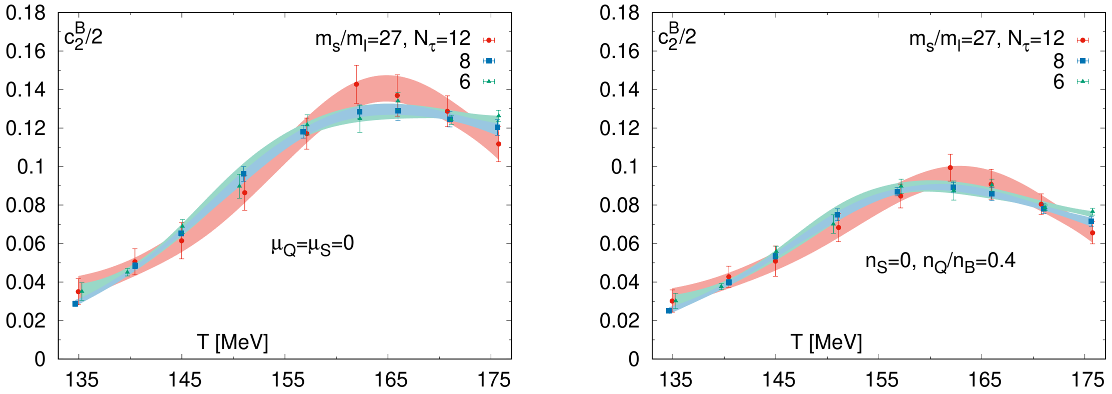

Figure 5.5: The 2nd order Taylor expansion coefficient of $\sigma_B^2/(V f_K^3)$ for systems with strangeness neutrality (right) and $\mu_Q = \mu_S = 0$ (left). The colored bands stem from the AIC weighted Padé sums and their corresponding derivatives. The data is shown for three finite lattice spacings with $N_\tau = 6, 8$ and 12.

In Fig. 5.4, we show the leading order c_0^B of net baryon-density fluctuations for three lattice spacings with $N_\tau = 6, 8$ and 12. The errors and cut-off effects are small and allow a good determination of the first T derivative of c_0^B as required for λ_2. The 2nd order c_2^B also has small cut-off effects but slightly larger statistical errors which can be seen in Fig. 5.5 In general, the behavior in a system with strangeness neutrality is similar to a system with $\mu_Q = \mu_S = 0$. However, the expansion coefficients are about 30% larger for vanishing μ_Q and μ_S which directly translates into larger fluctuations of σ_B^2 along the crossover line. The values for the expansion coefficients λ_n are summarized

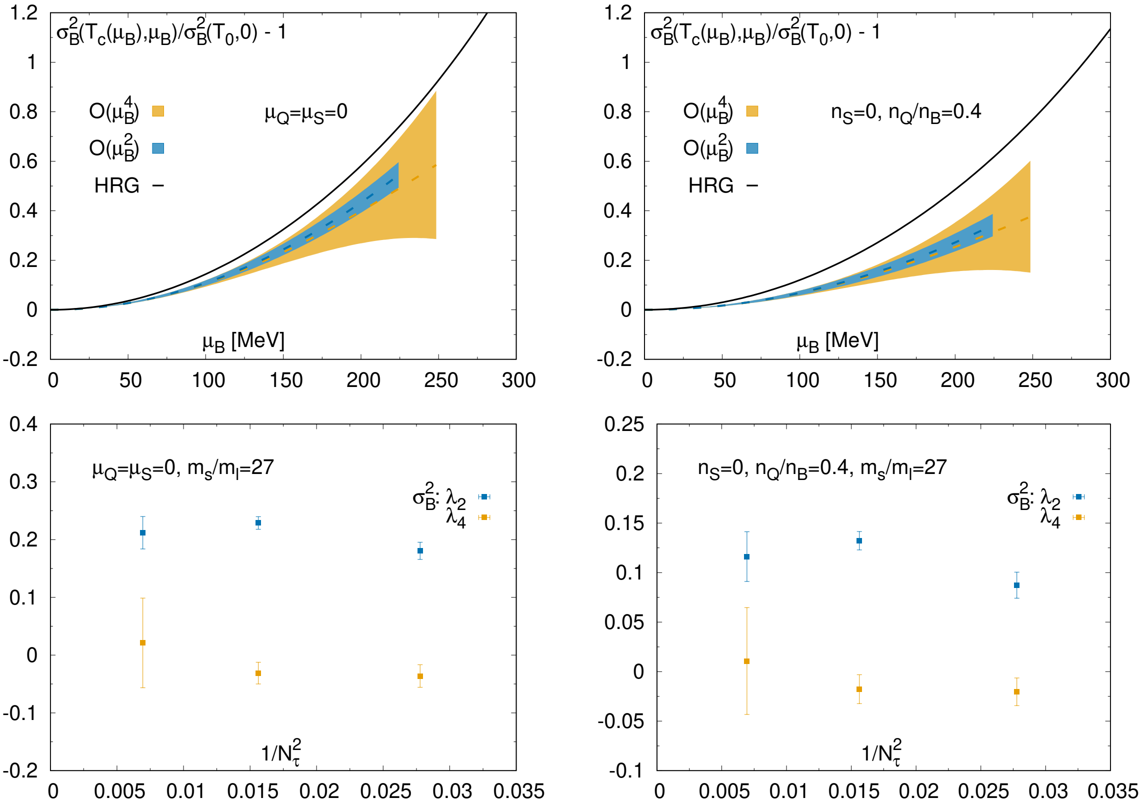

Figure 5.6: The relative change of σ_B^2 (top) along the crossover line $T_c(\mu_B)$ extracted from Σ_{sub} for systems with $\mu_Q = \mu_S = 0$ and strangeness neutrality. The blue band includes continuum extrapolated corrections up to 2nd order in μ_B and the yellow band up to 4th order in μ_B. The values for λ_2 and λ_4 at finite N_τ are shown in the bottom. The dashed lines represent the mean of the shown observable. The HRG results are shown using a solid black line.

N_τ		$\lambda_2(\sigma_B^2)$	$\text{err}(\lambda_2)$	$\lambda_4(\sigma_B^2)$	$\text{err}(\lambda_4)$
6		0.0873	0.0131	−0.0204	0.0139
8		0.132	0.00929	−0.0177	0.0146
12		0.116	0.025	0.0107	0.0539
∞	$n_S = 0, n_Q/n_B = 0.4$	0.165	0.0219	−0.00680	0.0340
6		0.181	0.0148	−0.0361	0.0195
8		0.229	0.0109	−0.0311	0.0188
12		0.212	0.0281	0.0211	0.0776
∞	$\mu_Q = \mu_S = 0$	0.263	0.0250	−0.0130	0.0454

Table 5.4: The coefficients λ_2 and λ_4 extracted from the relative change of σ_B^2 for systems with $\mu_Q = \mu_S = 0$ and strangeness neutrality at three lattice spacings with $N_\tau = 6, 8$ and 12. The continuum extrapolated values stem from a bootstrap using an ansatz with $\mathcal{O}(N_\tau^{-2})$ corrections. Here, err$(\cdot)$ denotes the standard error.

in Tab. 5.4 for finite N_τ and in the continuum. We found that the mean of the 4th order λ_4 is about factor 20 smaller than λ_2. The relative change of σ_B^2 is shown in Fig. 5.6 for both cases using $\mathcal{O}(\mu_B^2)$ and $\mathcal{O}(\mu_B^4)$ corrections. We observe a moderate increase of about 60% for net baryon-number fluctuations along the QCD crossover at $\mu_B = 250$ MeV and $\mu_Q = \mu_S = 0$ relative to σ_B^2 evaluated at $(T_0, \mu = 0)$. For a strangeness neutral system, the increase is about a factor 2 smaller. It has been shown successfully [11, 12] that net baryon-number fluctuations couple to the condensate and thus would show critical behavior when approaching a critical point. This is why we expect it to a be strong indicator to disfavor a critical point if no increased fluctuations can be observed. In particular interesting is to study deviations from the HRG model. Even for a finite volume, as given in heavy-ion collision and our simulations, these fluctuations should resemble some critical behavior in the vicinity of a critical point, i.e. show substantially larger fluctuations compared to HRG. In the HRG model, the partition function factorizes in a sum over all hadrons and their resonances [55]. It can be written as

$$\ln Z^{\mathrm{HRG}} = \sum_{i \in \mathrm{hadrons}} \ln Z_i = \sum_{i \in \mathrm{baryons}} \ln Z_i^B + \sum_{i \in \mathrm{mesons}} \ln Z_i^M . \tag{5.13}$$

The mesonic and baryonic partition functions are given for each hadron i by a fugacity expansion

$$\ln Z_i^B = \frac{VT^3}{\pi^2} d_i \left(\frac{m_i}{T}\right)^2 \sum_{k=1}^{\infty} \frac{(-1)^{k+1}}{k^2} K_2(km_i/T) \cosh\left(k(B_i\mu_B + Q_i\mu_Q + S_i\mu_S)/T\right) \tag{5.14}$$

and

$$\ln Z_i^M = \frac{VT^3}{\pi^2} d_i \left(\frac{m_i}{T}\right)^2 \sum_{k=1}^{\infty} \frac{1}{k^2} K_2(km_i/T) \cosh\left(k(Q_i\mu_Q + S_i\mu_S)/T\right) , \tag{5.15}$$

where d_i is the spin degeneracy and K_2 is a modified Bessel function of second kind. For the baryonic sector we can further simplify the partition function. In the confinement region, even the lightest baryon is much heavier than the temperature of interest. This is why we can approximate the Bessel function for large arguments as $K_2(x) \simeq \sqrt{\pi/2x}\exp(-x)$. In this case, all higher terms of the fugacity expansion are strongly suppressed and the contribution to the baryonic partition function is well described by the first term, referred to as Boltzmann approximation [56]. For the case $\mu_Q = \mu_S = 0$, only baryons contribute to the fluctuations of net baryon-number σ_B^2. As described in Eq. (5.9), we can express σ_B^2 in the HRG model as

$$\left(\frac{\sigma_B^2}{V}\right)^{\mathrm{HRG}} = \frac{T}{\pi^2} \sum_{i \in \mathrm{baryons}} d_i m_i^2 K_2(m_i/T) \cosh\left(\mu_B/T\right) . \tag{5.16}$$

Here, we have used that the baryon-number B_i is ± 1. When calculating the relative change of σ_B^2, the T dependent term in front of $\cosh(\mu_B/T)$ is not canceled by the denominator as the numerator has to be evaluated at $T_c(\mu_B)$. It is given by

$$\left(\frac{\sigma_B^2(T_c(\mu_B),\mu_B)-\sigma_B^2(T_0,0)}{\sigma_B^2(T_0,0)}\right)^{\mathrm{HRG}} = \alpha(T_c(\mu_B))\cosh\left(\mu_B/T_c(\mu_B)\right)-1 \tag{5.17}$$

with

$$\alpha(T_c(\mu_B)) = \frac{T_c(\mu_B)}{T_0}\,\frac{\sum_i d_i m_i^2 K_2(m_i/T_c(\mu_B))}{\sum_i d_i m_i^2 K_2(m_i/T_0)}\ . \tag{5.18}$$

We have checked that the sum in $\alpha(T_c(\mu_B))$ can be approximated by including only baryons up to 1.6 GeV as listed in [57]. Already baryons with masses of about 1.3 GeV have almost no visible effect on the fluctuations. For the HRG with the initial conditions of heavy-ion collisions, the equations become more complex and require an expansion similarly as shown in Sec. 2.2. This is why in this case we rely on [58] for the HRG results. In Fig. 5.6, we compare the fluctuations of σ_B^2 to the HRG model for a fixed curvature defined by the mean of the crossover parameters. The fluctuations are slightly larger in the HRG model with $\mu_Q = \mu_S = 0$ along the crossover line up to $\mu_B = 250$ MeV. For the strangeness neutral case, the fluctuations are at least a factor two smaller compared to HRG. Given that the HRG model has an infinite convergence radius and substantially larger fluctuations compared to our lattice simulations, we conclude it is unlikely that a QCD critical point can be found for $\mu_B < 250$ MeV along the crossover line. This is in agreement with our findings from the analysis of chiral susceptibility fluctuations along the crossover line (see Sec. 5.1).

6 Summary

We have studied the crossover from a hadron gas to a quark gluon plasma using lattice QCD techniques in the HISQ formulation with physical quark masses. At vanishing chemical potential, we determined the crossover temperature T_0 from chiral observables such as: subtracted condensate, subtracted susceptibility and disconnected susceptibility. By combining their values, we found that the crossover at zero chemical potential must occur in a temperature range from 155.4 MeV to 156.8 MeV.

Using a Taylor expansion up to 6th order in μ_B of these chiral observables, we were able to map out the QCD crossover line $T_c(\mu_B)$. For a system with initial conditions of a heavy-ion collision, we report a curvature κ_2 of 0.0120(20) from the subtracted condensate and 0.0123(30) from the disconnected susceptibility. The next order κ_4 is one magnitude smaller. We have compared this crossover line to the chemical freeze-out curve from heavy-ion collision experiments and lines of constant physics from lattice QCD simulations. We conclude that the crossover happens indeed close to the chemical freeze-out as well as along constant energy density and constant entropy density. We have explored the QCD phase diagram for several other cases using the above methods. In particular, $\mu_Q = \mu_S = 0$, $\mu_B = \mu_S = 0$, $\mu_B = \mu_Q = 0$ as well as a strangeness neutral system with $n_Q/n_B = r$ where we varied r between 0.1 and 0.5. The dependence on r is small. We found that the QCD phase diagram has very similar curvatures κ_2 in all directions except for $\mu_B = \mu_S = 0$. In this case, the curvature κ_2 is 0.0314(39), i.e. a factor two larger. Complementary, we measured 6th order expansion coefficients for a fixed lattice spacing and outlined that these higher order corrections are negligible for $\mu_B < 250$ MeV.

This crossover line parameterization enabled us to study net baryon-number fluctuations as a function of $T_c(\mu_B)$. Along the crossover, their increase is substantially smaller compared to a HRG. Similarly, we have analyzed chiral susceptibility fluctuations along the crossover and showed that they can be seen as constant. Given this strong evidence, we conclude that no critical point can be found for the crossover region with $\mu_B < 250$ MeV.

A Data

A.1 Chiral condensate

$N_\tau = 6$	T [MeV]	Σ_l/T^3	err(Σ_l/T^3)
	135.29	14.4041	0.0055
	139.71	12.8407	0.0057
	145.05	10.9964	0.0042
	150.59	9.1731	0.0087
	157.17	6.8713	0.0093
	162.28	5.2775	0.0077
	165.98	4.3304	0.0080
	171.15	3.1760	0.0021
	175.76	2.4719	0.0028

Table A.1: The $N_\tau = 6$ light quark chiral condensate as defined in Sec. 3.5.

$N_\tau = 6$	T [MeV]	Σ_s/T^3	err(Σ_s/T^3)
	135.29	19.8638	0.0016
	139.71	18.8669	0.0011
	145.05	17.7121	0.0010
	150.59	16.6032	0.0016
	157.17	15.3486	0.0016
	162.28	14.4418	0.0016
	165.98	13.8492	0.0017
	171.15	12.9961	0.0003
	175.76	12.3201	0.0011

Table A.2: The $N_\tau = 6$ strange quark chiral condensate as defined in Sec. 3.5.

$N_\tau = 8$	T [MeV]	Σ_l/T^3	err(Σ_l/T^3)
	134.64	16.8727	0.0023
	140.45	14.2496	0.0034
	144.95	12.2943	0.0031
	151.00	9.8550	0.0044
	156.78	7.5605	0.0030
	162.25	5.7199	0.0078
	165.98	4.6493	0.0042
	171.02	3.5823	0.0030
	175.64	2.8890	0.0042

Table A.3: The $N_\tau = 8$ light quark chiral condensate as defined in Sec. 3.5.

$N_\tau = 8$	T [MeV]	Σ_s/T^3	err(Σ_s/T^3)
	134.64	30.26437	0.00051
	140.45	28.16075	0.00080
	144.95	26.59860	0.00059
	151.00	24.84251	0.00097
	156.78	23.12819	0.00059
	162.25	21.78016	0.00174
	165.98	20.85494	0.00097
	171.02	19.76819	0.00075
	175.64	18.83039	0.00149

Table A.4: The $N_\tau = 8$ strange quark chiral condensate as defined in Sec. 3.5.

$N_\tau = 12$	T [MeV]	Σ_l/T^3	err(Σ_l/T^3)
	134.94	18.6824	0.0093
	140.44	15.9043	0.0097
	144.97	13.8023	0.0092
	151.10	11.0801	0.0096
	157.13	8.6638	0.0091
	161.94	7.0019	0.0180
	165.91	5.8801	0.0058
	170.77	4.8848	0.0089
	175.76	4.1109	0.0061

Table A.5: The $N_\tau = 12$ light quark chiral condensate as defined in Sec. 3.5.

$N_\tau = 12$	T [MeV]	Σ_s/T^3	err(Σ_s/T^3)
	134.94	53.9234	0.0022
	140.44	50.7552	0.0017
	144.97	48.4404	0.0015
	151.10	45.4176	0.0012
	157.13	42.8728	0.0010
	161.94	40.9633	0.0026
	165.91	39.3996	0.0012
	170.77	37.7773	0.0024
	175.76	36.2869	0.0020

Table A.6: The $N_\tau = 12$ strange quark chiral condensate as defined in Sec. 3.5.

$N_\tau = 16$	T [MeV]	Σ_l/T^3	err(Σ_l/T^3)
	144.9	15.9847	0.071
	151.0	13.3869	0.056
	156.9	10.7595	0.055
	162.0	8.8264	0.080
	166.0	7.6947	0.067
	170.9	6.6667	0.054

Table A.7: The $N_\tau = 16$ light quark chiral condensate as defined in Sec. 3.5.

$N_\tau = 16$	T [MeV]	Σ_s/T^3	err(Σ_s/T^3)
	144.9	76.569	0.0071
	151.0	73.536	0.0058
	156.9	69.706	0.0059
	162.0	66.552	0.0086
	166.0	64.403	0.0078
	170.9	62.168	0.0102

Table A.8: The $N_\tau = 16$ strange quark chiral condensate as defined in Sec. 3.5.

A.2 Chiral susceptibility

$N_\tau = 6$	T [MeV]	$4\chi_{f,\text{disc}}/T^2$	$\text{err}(4\chi_{f,\text{disc}}/T^2)$	$f = u, d$
	135.29	31.15	0.24	
	139.71	35.31	0.20	
	145.05	41.58	0.22	
	150.59	48.16	0.37	
	157.17	57.26	0.38	
	162.28	53.95	0.40	
	165.98	45.86	0.19	
	171.15	29.87	0.14	
	175.76	18.48	0.09	

Table A.9: The $N_\tau = 6$ light quark disconnected chiral susceptibility as defined in Sec. 3.5.

$N_\tau = 8$	T [MeV]	$4\chi_{f,\text{disc}}/T^2$	$\text{err}(4\chi_{f,\text{disc}}/T^2)$	$f = u, d$
	134.64	43.99	0.16	
	140.45	50.26	0.15	
	144.95	57.32	0.16	
	151.00	66.45	0.22	
	156.78	71.04	0.24	
	162.25	62.26	0.25	
	165.98	49.06	0.08	
	171.02	31.56	0.25	
	175.64	19.47	0.13	

Table A.10: The $N_\tau = 8$ light quark disconnected chiral susceptibility as defined in Sec. 3.5.

$N_\tau = 12$	T [MeV]	$4\chi_{f,\mathrm{disc}}/T^2$	$\mathrm{err}(4\chi_{f,\mathrm{disc}}/T^2)$	$f = u, d$
	134.94	62.98	0.49	
	140.44	71.76	0.56	
	144.97	81.36	0.73	
	151.10	94.78	0.45	
	157.13	95.69	1.24	
	161.94	84.52	0.70	
	165.91	66.03	0.60	
	170.77	47.15	0.62	
	175.76	31.18	0.28	

Table A.11: The $N_\tau = 12$ light quark disconnected chiral susceptibility as defined in Sec. 3.5.

$N_\tau = 16$	T [MeV]	$4\chi_{f,\mathrm{disc}}/T^2$	$\mathrm{err}(4\chi_{f,\mathrm{disc}}/T^2)$	$f = u, d$
	144.9	107.92	6.56	
	151.0	128.32	4.27	
	156.9	126.94	3.96	
	162.0	115.64	4.64	
	166.0	89.32	4.45	
	170.9	69.68	3.84	

Table A.12: The $N_\tau = 16$ light quark disconnected chiral susceptibility as defined in Sec. 3.5.

$N_\tau = 8$	T [MeV]	$2\chi_{f,\mathrm{conn}}/T^2$	$\mathrm{err}(2\chi_{f,\mathrm{conn}}/T^2)$	$f = u, d$
	134.64	118.43	0.30	
	140.45	123.58	0.36	
	144.95	131.12	0.44	
	151.00	140.88	0.29	
	156.78	152.77	0.29	
	162.25	156.87	0.22	
	165.98	155.01	0.33	
	171.02	145.09	0.30	
	175.64	131.53	0.51	

Table A.13: The $N_\tau = 8$ light quark connected chiral susceptibility as defined in Sec. 3.5.

$N_\tau = 12$	T [MeV]	$2\chi_{f,\mathrm{conn}}/T^2$	$\mathrm{err}(2\chi_{f,\mathrm{conn}}/T^2)$	$f = u, d$
	134.94	209.61	0.25	
	140.44	213.74	0.31	
	144.97	217.90	0.43	
	151.10	223.90	0.51	
	157.13	227.47	0.53	
	161.94	226.52	0.38	
	165.91	220.24	0.30	
	170.77	208.57	0.42	
	175.76	196.49	0.21	

Table A.14: The $N_\tau = 12$ light quark connected chiral susceptibility as defined in Sec. 3.5.

$N_\tau = 16$	T [MeV]	$2\chi_{f,\mathrm{conn}}/T^2$	$\mathrm{err}(2\chi_{f,\mathrm{conn}}/T^2)$	$f = u, d$
	144.9	304.90	0.61	
	151.0	304.35	0.53	
	156.9	307.11	0.55	
	162.0	304.95	0.84	
	166.0	299.60	0.80	
	170.9	291.57	0.97	

Table A.15: The $N_\tau = 16$ light quark connected chiral susceptibility as defined in Sec. 3.5.

Bibliography

[1] Y. Aoki, G. Endrodi, Z. Fodor, S. D. Katz, and K. K. Szabo. The Order of the quantum chromodynamics transition predicted by the standard model of particle physics. *Nature*, 443:675–678, 2006.

[2] Tanmoy Bhattacharya et al. QCD Phase Transition with Chiral Quarks and Physical Quark Masses. *Phys. Rev. Lett.*, 113(8):082001, 2014.

[3] Heng-Tong Ding, Frithjof Karsch, and Swagato Mukherjee. Thermodynamics of strong-interaction matter from Lattice QCD. *Int. J. Mod. Phys.*, E24(10), 2015.

[4] Kenji Fukushima and Tetsuo Hatsuda. The phase diagram of dense QCD. *Rept. Prog. Phys.*, 74:014001, 2011.

[5] Xiaofeng Luo and Nu Xu. Search for the QCD Critical Point with Fluctuations of Conserved Quantities in Relativistic Heavy-Ion Collisions at RHIC : An Overview. *Nucl. Sci. Tech.*, 28(8):112, 2017.

[6] T. Matsui and H. Satz. J/ψ Suppression by Quark-Gluon Plasma Formation. *Phys. Lett.*, B178:416–422, 1986.

[7] Edward V. Shuryak. Quantum Chromodynamics and the Theory of Superdense Matter. *Phys. Rept.*, 61:71–158, 1980.

[8] S. Jeon and V. Koch. Charged particle ratio fluctuation as a signal for Quark-Gluon Plasma. *Phys.Rev.Lett.*, 85:2076–2079, 2000.

[9] M. Asakawa et al. Fluctuation probes of quark deconfinement. *Phys.Rev.Lett.*, 85:2072–2075, 2000.

[10] S. Jeon and V. Koch. Event by event fluctuations. *In *Hwa, R.C. (ed.) et al.: Quark gluon plasma**, pages 430–490, 2003.

[11] Y. Hatta and M. A. Stephanov. Proton number fluctuation as a signal of the QCD critical endpoint. *Phys. Rev. Lett.*, 91:102003, 2003.

[12] M. Stephanov. QCD critical point and correlations. *J. Phys. Conf. Ser.*, 27:144–153, 2005.

[13] P. Steinbrecher. *Noise reduction for charge fluctuations: an investigation on many-core architecture.* 2015.

[14] C. Gattringer and C. Lang. *Quantum Chromodynamics on the Lattice.* 2010.

[15] H. J. Rothe. *Lattice Gauge Theories. An Introduction.* 2005.

[16] X. Du. The staggered chiral perturbation theory in the two-flavor case and SU(2) chiral analysis of the MILC data. dx.doi.org/10.7936/K7HX19T2, 2010.

[17] R. Sommer. Scale setting in lattice QCD. *DESY*, 13:262, 2014, [arXiv:1401.3270 [hep-lat]].

[18] A. Bazavov et al. Full nonperturbative QCD simulations with 2+1 flavors of improved staggered quarks. *Rev.Mod.Phys.*, 82:1349–1417, 2010.

[19] J. Kogut and L. Sussind. Hamiltonian formulation of Wilson's lattice gauge theories. *Phys.Rev.*, D11:395, 1975.

[20] Michael Creutz. Chiral anomalies and rooted staggered fermions. *Phys. Lett.*, B649:230–234, 2007.

[21] Claude Bernard, Maarten Golterman, Yigal Shamir, and Stephen R. Sharpe. 't Hooft vertices, partial quenching, and rooted staggered QCD. *Phys. Rev.*, D77:114504, 2008.

[22] H. B. Nielsen and M. Ninomiya. No go theorem for regularizing chiral fermions. *Phys.Lett.*, D11:395, 1975.

[23] E. Follana et al. Highly Improved Staggered Quarks on the Lattice, with applications to charm physics. *Phys.Rev.*, D75:054502, 2007.

[24] Y. Aoki, Z. Fodor, S. D. Katz, and K. K. Szabo. The Equation of state in lattice QCD: With physical quark masses towards the continuum limit. *JHEP*, 01:089, 2006.

[25] M. A. Clark. *The Rational Hybrid Monte Carlo Algorithm.* 2005.

[26] P. Hasenfratz and F. Karsch. Chemical potential on the Lattice. *Phys.Lett.*, B125:308, 1983.

[27] R. V. Gavai and S. Sharma. A faster method of computation of lattice quark number susceptibilities. *Phys. Rev. D*, 85:054508, 2012, [arXiv:1112.5428 [hep-lat]].

[28] R. V. Gavai and S. Sharma. Divergences in the quark number susceptibility: The origin and a cure. *Phys. Lett. B*, 749:8, 2015, [arXiv:1406.0474 [hep-lat]].

[29] P. Forcrand. Lattice QCD at finite density. [arXiv:hep-lat/1005.0539], 2010.

[30] E. Laermann and O. Philipsen. Status of Lattice QCD at finite temperature. *Ann.Rev.Nucl.Part.Sci*, 53:163–198, 2003.

[31] M. Cheng et al. The QCD Equation of State with almost physical quark masses. *Phys.Rev.*, D77:014511, 2008.

[32] A. Bazavov et al. The chiral and deconfinement aspects of the QCD transition. *Phys. Rev. D*, 85:054503, 2012, [arXiv:1111.1710 [hep-lat]].

[33] C. Schmidt. *The phase diagram and equation of state of improved lattice QCD for high temperatures and small chemical potentials.* 2003.

[34] C.R. Allton et al. Thermodynamics of two flavor QCD to sixth order in quark chemical potential. *Phys.Rev.*, D71:054508, 2005.

[35] A. Bazavov et al. QCD equation of state to $\mathcal{O}(\mu_B^6)$ from lattice QCD. *Phys.Rev.*, D95:054504, 2017, [arXiv:1701.04325 [hep-lat]].

[36] S. Dong and K. Liu. Stochastic estimation with Z_2 noise. *Phys.Lett.*, B328:130–136, 1994.

[37] notes/discussion from/with C. Schmidt. 2017.

[38] T. Kalkreuter and H. Simma. An accelerated conjugate gradient algorithm to compute low-lying eigenvalues. *Comput.Phys.Commun.*, 93, 1996.

[39] K. Wu and H. Simon. Thick-restart Lanczos method for large symmetric eigenvalue problems. *SIAM J. Matrix Anal. Appl.*, 2, 2000.

[40] discussion with Swagato Mukherjee. 2017.

[41] K. Burnham and D. Anderson. *Model Selection and Multimodel Inference.* 2002.

[42] S. Borsanyi et al. Is there still any T_c mystery in lattice QCD? Results with physical masses in the continuum limit III. *JHEP*, 1009:073, 2010, [arXiv:1005.3508 [hep-lat]].

[43] C. Bonati et al. Curvature of the chiral pseudo-critical line in QCD: Continuum extrapolated results. *Phys.Rev. D*, 92:054503, 2015, [arXiv:1507.03571 [hep-lat]].

[44] R. Bellwied et al. The QCD phase diagram from analytic continuation. *Phys.Lett. B*, 751:559–564, 2015, [arXiv:1507.07510 [hep-lat]].

[45] Floris, M. Hadron yields and the phase diagram of strongly interacting matter. *Nucl. Phys. A*, 931:103, 2014, [arXiv:1408.6403 [nucl-ex]].

[46] STAR Collaboration. Bulk Properties of the Medium Produced in Relativistic Heavy-Ion Collisions from the Beam Energy Scan Program. *Phys.Rev. C*, 96:044904, 2017, [arXiv:1701.07065 [nucl-ex]].

[47] J. Cleymans and K. Redlich. Chemical and thermal freeze-out parameters from $1A$ to $200A$ GeV. *Phys.Rev. C*, 60:054908, 1999.

[48] J. Cleymans et al. Comparison of chemical freeze-out criteria in heavy-ion collisions. *Phys.Rev. C*, 73:034905, 2006.

[49] W. Cassing et al. Chiral symmetry restoration versus deconfinement in heavy-ion collisions at high baryon density. *Phys. Rev.*, C93:014902, 2016.

[50] To be published by HotQCD.

[51] STAR Collaboration. Higher moments of net proton multiplicity distributions at RHIC. *Phys.Rev.Lett.*, 105:022302, 2010.

[52] A. Bazavov et al. Skewness and kurtosis of net baryon-number distributions at small values of the baryon chemical potential. *Phys. Rev.*, D96(7):074510, 2017.

[53] A. Bazavov et al. Freeze-out Conditions in Heavy Ion Collisions from QCD Thermodynamics. *Phys.Rev.Lett.*, 109:192302, 2012.

[54] A. Bazavov et al. Fluctuations and Correlations of net baryon number, electric charge, and strangeness: A comparison of lattice QCD results with the hadron resonance gas model. *Phys.Rev.*, D85:054503, 2012.

[55] R. Venugopalan et al. Thermal properties of interacting hadrons. *Nucl.Phys.*, A546:718–760, 1992.

[56] F. Karsch et al. Thermodynamics at non-zero baryon number density: A comparison of lattice and Hadron Resonance Gas Model calculations. *Phys.Lett.*, B571:67–74, 2003.

[57] K. Nakamura et al. Review of particle physics. *J. Phys.*, G37:075021, 2010.

[58] HRG code from Frithjof Karsch. 2017.

List of Figures

List of Tables

Disclaimer

I hereby declare that the work done in this dissertation is that of the author alone with the help of no more than the mentioned literature and auxiliary means.

Patrick Steinbrecher